2019-01-01

Processing, Structure And Mechanical Behavior Of Advanced Engineering Steels

Bing Yu
University of Texas at El Paso

PROCESSING, STRUCTURE AND MECHANICAL BEHAVIOR

OF ADVANCED ENGINEERING STEELS

BING YU

Doctoral Program in Materials Science and Engineering

APPROVED:

R. Devesh K. Misra, Ph.D., Chair

Srinivasa Rao Singamaneni, Ph.D.

Guikuan Yue, Ph.D.

Stephen L. Crites, Jr., Ph.D.
Dean of the Graduate School

PROCESSING, STRUCTURE AND MECHANICAL BEHAVIOR OF ADVANCED ENGINEERING STEELS

by

BING YU

DISSERTATION

Presented to the Faculty of the Graduate School of

The University of Texas at El Paso

in Partial Fulfillment

of the Requirements

for the Degree of

DOCTOR OF PHILOSOPHY

Department of Metallurgical, Materials and Biomedical Engineering

THE UNIVERSITY OF TEXAS AT EL PASO

December 2019

Acknowledgements

I would like to express my sincere gratitude to the esteemed Professor and my research advisor, Dr. R. Devesh K. Misra, for giving me the opportunity to work with him. His continuous support, guidance and encouragement enabled me to be enthusiastic during the entire period of doctoral research. His numerous invaluable comments, assistance, and guidance were of most importance and added significant value to the research study.

Particular thanks are given to Dr. Srinivasa Rao Singamaneni and Dr. Guikuan Yue for serving on the dissertation committee.

Words are not adequate to convey my deepest gratitude to my family for their unconditional love and support. They gave me enough freedom to pursue my future endeavor.

I would also like to thank my friends, Dr. Kun Li and Dr. Shilong Liu, for suggestion and help.

I am thankful to the colleagues and the laboratory staff for their assistance and to the Department of Metallurgical, Materials, and Biomedical Engineering at the University of Texas at El Paso for the facilities.

Lastly, financial support from National Science Foundation, USA is gratefully acknowledged.

Abstract

The concept of low lattice misfit and high-density of nanoscale precipitates obtained through solution treatment was adopted to obtain ultrahigh strength maraging steel without compromising elongation. An "ultrahigh strength-high toughness" combination was successfully obtained in 19Ni3Mo1.5Ti maraging steel with ultimate strength of ~1858 MPa and static toughness of ~110 $MJ \cdot m^{-3}$. Maraging steel had extremely high density ($2.3 \times 1024\ m^{-3}$) of nanoscale precipitates with minimum lattice misfit of less than 1% at the solutionization temperature of 820 ºC. Two kinds of nanoscale precipitates, namely, η-Ni3(Ti,Mo) and B2-Ni(Mo,Fe) contributed to ultrahigh strength. The size of nanoscale precipitates governed the movement of dislocations, cutting versus by-passing. Theoretical estimate of ordering and modulus contribution to strengthening suggested that ordering had a dominant influence on strength. The toughness was closely related to the characteristic evolution of nanoscale precipitates such that the high density of nanoscale precipitates contributed to increase of elastic deformation and low lattice misfit contributed to increase of uniform deformation. The nanoscale size and low lattice misfit of precipitates were the underlying reasons for the high-performance of maraging steel. Moreover, the combination of high-density of nanoscale precipitates and low lattice misfit is envisaged to facilitate the futuristic design and development of next generation of structural alloys. The low lattice misfit (0.6% ~ 0.9%) precipitates interacted with dislocations leaving stacking fault ribbons within precipitates and built a large long range of back stress producing a high strain-hardening response. Additionally, nanoscale twinning occurred. The above contributions to ductility are envisaged to be in addition to the significantly reduced elastic interaction between the low lattice misfit nanoscale precipitates and dislocations that reduces the ability for crack initiation at the particle-matrix interface. EBSD studies suggested that preferred orientations of {101}, fraction of high-angle grain boundary

(HAGB) and total length of grain boundary per unit area (μm/μm2) were increased with increase of aging temperature, which was beneficial to both strengthening and toughening of maraging steel. Three types of reverted austenite, granular reverted austenite at grain boundaries (γG1), lamellar reverted austenite in the matrix (γL) and globular reverted austenite (γG2) were observed depending on the aging temperature and time. At low temperatures (560 °C and 640 °C), only γG1 and γL were observed. While at high temperature (700 °C), γG1 and γL decreased with holding time increased and were completely transformed to γG2 at equilibrium condition. The observation of three different morphologies of reverted austenite were a consequence of competition between the nucleation rate and growth rate of reverted austenite at different aging temperatures. The weak texture of maraging steel with high Schmid factor at high aging temperature implied that γL and γG2 are the likely reasons for superior toughness and ductility. We underscored that it is important to consider and control the morphology and content of reverted austenite, besides other microstructural features when interpreting the mechanical behavior.

Table of Contents

List of Tables

List of Figures

Chapter 1: Introduction

With continuous demand in high performance and improvement of product quality, steel industry and researchers are currently seeking to increase the reliability in manufacturing, reduction in energy consumption, and design light-weight materials for automotive, aerospace and navigation applications. Three ultimate objectives of nowadays steel researches are: better mechanical properties, low weight and easy for manufacturing.

Ultrahigh strength steels and high strength low alloy steels are two approaches to satisfy these criteria. Ultrahigh strength steels basically have a dislocated martensitic structure with fine precipitates. The class can be subdivided into low-alloy steels, precipitation hardened stainless steels, maraging steels, and alloyed secondary hardening steels. All these steels are martensitic in microstructure and derive strength from precipitation strengthening, dislocation strengthening and structural refinement. These steels are developed for exceptional performance at high strength levels [1,2]. Among all these classifications maraging steel and medium manganese steel are the most ideal representative because they offer an unusual combination of high tensile strength and high fracture toughness.

1.1 MARAGING STEEL

It is customary to regard maraging steels as low-carbon precipitation-strengthened Fe+Ni martensitic steels [3-4]. The term ‘maraging’ is derived from the combination of the words martensite and age-hardening. Maraging steels are a class of low-carbon martensitic steels, which employ substitutional alloying elements and intermetallic compounds to achieve precipitation strengthening (formed during thermal ageing). They were first introduced by Bieber [3]. However,

during initial development, high levels nickel (20 ± 25 wt.%) contain was added without chromium Currently they have aluminum, titanium and niobium, which are added to achieve age hardening.

Maraging steel is two times harder than stainless steel and 85% harder than pure titanium. Maraging steel alloys are twice as hard as stainless steel and 35% stronger than the hardest titanium alloy. On the Rockwell scale of hardness, stainless steel is 23-26, titanium alloys are 28-41 and maraging steel is around 52-55. There is no ambiguity that maraging steels can be used for critical applications because of their ultra-high strength combined with excellent fracture toughness. Maraging steel is used in aircraft, with applications including landing gear, helicopter undercarriages, slat tracks and rocket motor casing – applications which require high strength-to-weight material. Maraging steel offers an unusual combination of high tensile strength and high fracture toughness. Most high-strength steels have low toughness, and the higher their strength the lower their toughness. The rare combination of high strength and toughness within the maraging steel makes it well suited for critical aircraft structures that require high strength and damage tolerance. [6]

1.1.1 Type of maraging steel

Bieber [3] discovered the effectiveness of cobalt and molybdenum in introducing precipitation strengthening in martensite. This led to the standardized grades of maraging steels in the early 1960s, designated 18NiCo - 200, 18NiCo – 250, 18NiCo – 300 and 18NiCo 350 in Table 1.1 [3,4,5,7]. They are classified according to their 0.2% proof stress or yield strength level, namely 200, 250, 300 and 350 ksi. in general, the higher the strength, higher is the cobalt and titanium content in the alloy.

Table 1.1 Grades of maraging steels and their alloys composition [3,4,7].

Element	Grade 200	Grade 250	Grade 300	Grade 350
Iron	Balance	Balance	Balance	Balance
Nickel	17.0 – 19.0	17.0 – 19.0	18.0 – 19.0	18.0 – 19.0
Cobalt	8.0 – 9.0	7.0 – 8.5	8.5 – 9.5	11.5 – 12.5
Molybdenum	3.0 – 3.5	4.6 – 5.2	4.6 – 5.2	4.6 – 5.2
Titanium	0.15 – 0.25	0.3 – 0.5	0.5 – 0.8	1.3 – 1.6
Aluminum	0.05 – 0.15	0.05 – 0.15	0.05 – 0.15	0.05 – 0.15

Maraging 200

Maraging 200 is a tough, relatively soft and therefore readily machined and formed. The properties are achieved through martensitic precipitation aging. When working with maraging steels even though some of them contain titanium and some contain cobalt as strengthening element, it is important to remember that their physical properties vary only slightly and are extremely similar. Usually Maraging 200 furnished in the annealed condition can be easily to machined and relatively soft. However, after heat treating via a precipitation hardening, the hardness increases greatly, which makes the steel quality for many tooling applications [8].

Maraging 250

Like all maraging steels, goes through an aging process that forces the metal to cool from its molten state to its solid state over an artificially long time. This process results in tempered steel that has both high levels of strength and hardness. It will also resist certain stresses and maintain

its structure in environments that would cause irreparable changes into many other steels. The properties that make Maraging 250 particularly appealing to many industries is its workability. This allows Maraging 250 to be more versatile than many other alloys in its class. However, it is still the alloy's strength and resistance to extreme temperatures that makes it a truly effective material in a wide range of environment. After Maraging 250 has undergone heat treatment, it demonstrates excellent mechanical properties. It will reach a yield strength of 240 ksi and a fracture toughness of 75 k_{Ic}. These properties have made Maraging 250 effective in the construction of missile and rocket motor casing, landing and takeoff gear, and high-performance shaft [9].

Maraging steel 300

This grade exhibits high levels of strength and hardness in a manner similar to all other maraging steels. However, Maraging 300 also possesses an extreme resistance to crack propagation, even in the most extreme environments. Maraging 300 is often used in applications where high fracture toughness is required or where dimensional changes have to remain at a minimal level. The unique properties of Maraging 300 have made it an integral part of the aircraft and aerospace industries. It is often used in rocket motor casings and the landing gear for certain planes. Maraging 300 is also effective in the design of power shafts and low-temperature cooling systems. Maraging steel 350 refers to crystalline tempered steel. Martensite, which is created through an aging process. When aging is used, steel is forced to cool from its molten state to its solid state over a prolonged period. The result is a metal that is harder and stronger than it would be had the steel been allowed to cool at a natural rate.

Maraging 350

Maraging steel 350 is the integral material in aerospace industry. Due to its strength and its ability to withstand extreme conditions including frequent and sudden changes in speed and

temperature, Maraging 350 is used in the production of rocket motor cases, takeoff and landing gear, and certain munitions created by defense companies. Maraging 350 also has uses in less drastic applications such as die casting and high-performance shafting.

The average density of maraging steel is equivalent to 8 g/cm^3 and the melting point is 1413 °C. It possesses excellent mechanical properties like higher yield strength and UTS. Besides, it has higher impact strength, fatigue strength, compressive strength, toughness, ductility, hardness, and wear resistance. It has excellent machinability characteristics and readily cold and hot formed. Maraging steels are highly resistant to crack propagation and possess good wettability. For heat treating, maraging steels require lower furnace temperature. Uniform and predictable shrinkage occurs during heat treatment. Minimal distortion occurs during hardening and free from the formation of carburized or decarburized layers on its surface. Maraging steels have the unique combination of ultra-high yield and tensile strength, ductility, and fracture toughness of any ferrous materials. It can retain its strength up to 350 °C. Having a very low carbon martensite, the structure is soft and readily machinable. It can be surface hardened by nitriding [5].

1.1.2 C-type maraging steel and T-type maraging steel

In addition, with the overwhelming demanding in maraging steel, the high cost of cobalt became a problem and to overcome this there has been an interest in developing maraging steels which do not contain cobalt to lower the cost of raw material. T type maraging steel was introduce in 1988 by Decker and Floreen [10]. These grades typically are obtained by reducing or eliminating the cobalt content and maintained original strength levels by increasing the titanium level. For example, the cobalt-free alloys designed to replace the 18NiCo(C-250) and 18NiCo(C-300) grades contain 1.4 and 1.85 wt% titanium (T-250 and T-300), respectively. When the nickel content is greater than about 12 wt%, Asayama [11] showed that an addition of 3 wt% chromium improves

toughness. Presence of nanoscale precipitates of high density in the microstructure of 250 grade cobalt free maraging steel gives rise to appreciable enhancement of strength and toughness.

1.1.3 Production characteristic

Melting

The maraging steels may be melted in air by arc or induction methods as well as by vacuum induction and consumable-electrode methods. Regarding 25 Ni steel, vacuum-melted material has been developed with somewhat higher strength than the air-melted material. Ductility was not improved by vacuum melting. With respect to the 20 Ni steel and the 18 Ni Co Mo steels, vacuum-melted stock indicated better ductility and notch toughness than have been obtained by air melting.

Forging

The maraging steels should be soaked and forged at 1000 to 1200 °C. Forging should be finished at about 800 °C for grain-size control and optimum mechanical properties after heat treatment. The forging behavior of the maraging steels is about the same as that of a medium alloy steel. In some instances, titanium segregation has not been eliminated in a single upset forging operation; substantial reduction in forging and intermediate soaking was required.

Rolling

The maraging steels are readily hot rolled in the temperature range of 800 to 1000 °C in between heat treatment. Again, finishing at about 800 °C is necessary for grain size control. The maraging steels are readily cold rolled. All four types have been cold reduced as much as 90 percent between anneals. Even those steels that are martensitic at room temperature are readily cold rolled. This is attributed to the fact that low-carbon martensite is relevant soft and work hardens slowly.

Heat treatment

Maraging steel is produced by heating the steel in the austenite region usually above 850 °C (Austenization), followed by air cooling to form a martensitic microstructure. The slow cooling of hypoeutectic austenite steel usually results in the formation of ferrite and pearlite and rapid cooling by quenching in water or oil is often necessary to form martensite. However, martensite forms in maraging steel upon slow cooling due to the high nickel content which suppresses the formation of ferrite and pearlite. Obtained martensitic microstructure in as-cooled maraging steel is soft compared with other martensite formed in plain carbon steels by quenching and the softness is an advantage because it will result in high ductility and toughness without the need for tempering. The softness also allows maraging steel to be machined into structural components, unlike hard martensitic steels that must be tempered before machining to avoid cracking.

The martensite in maraging steels is soft and the steel can achieve its strength only after ageing; age hardening of maraging steels is due to the precipitation of ultrafine second phase particles dispersed uniformly throughout the martensitic matrix. Precipitation strengthening of maraging steels can be accomplished in several different ways. Improvement in mechanical properties of 250 grade maraging steel can be achieved by cyclic ageing treatment where repeated thermal cycling is done within the preselected ageing temperatures. During ageing segregation of austenite stabilizing elements can occur which, creates regions of high concentration of austenite former and thus increases the amount of reverted austenite; this takes care of toughness whereas fine scale precipitation of Laves phase Fe_2Mo takes place at the high ageing temperature and as a result strength increment by more than 20% is possible [12]. Modification of tempering / ageing treatment envisages further improvement in strength and impact properties of maraging steel [13]; one approach proposed recently is the short time ageing treatment for which a higher aging

temperature is required. Normally, higher temperature aging is discouraged in maraging steel owing to the threat for the formation of undue amount of reverted austenite due primarily to the presence of high amount of austenite stabilizers in the composition. However, a shorter time ageing at the high ageing temperature can alleviate with the problem of formation of increased amount to reverted austenite. In general, maraging steel is reheated around 480–500 °C for several hours to form a fine dispersion of hard precipitates within martensite matrix as shown in figure 1.1 [14].

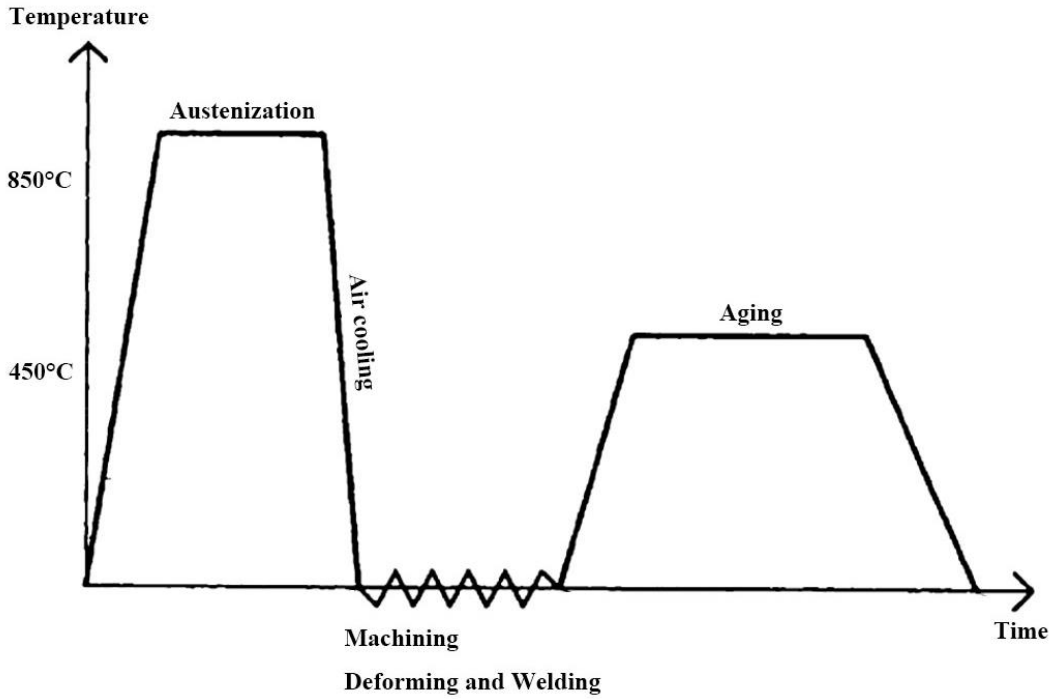

Figure 1. 1 Schematic diagram of the heat treatment process of maraging steels [14].

Fabrication

Welding is considered in detail in a later chapter regarding welding properties of maraging steel. Based on limited tests, the 20 Ni and 25 Ni steels have a machinability rating about 50 percent that of free-machining stainless steels. In the annealed condition, the steels are soft and susceptible to tearing. Better finishes, higher machining rates, and improved tool life are obtained on fully hardened material. The 18 Ni-Co-Mo steels in the annealed condition appear to machine somewhat

more readily than the 20 Ni and 25 Ni steels in the as-annealed or as-hardened condition. Even though the steel work hardens very slowly, the ductility in the annealed condition, as measured by elongation in 2 inches, is only 15 to 25 per cent. Consequently, extensive stretching and deep drawing will require intermediate annealing [15].

1.1.4 Alloying elements in maraging steel

Nickel

Nickel was added to maraging steel when its initial development by C. G. Bieber [3]. On adding 25% of nickel in steel, the Ms temperature is decreased to near room temperature and upon cooling room temperature a semi-austenitic composition was achieved. Current commercial maraging steel contains 17-19% Nickel to ensure maintaining fully martensitic composition at room temperature. Moreover, nickel reduces the tendency for cleavage and lowers the ductility-brittle transformation temperature (DBTT) of steel.

Cobalt

Cobalt is an important alloying element in maraging steel and serves several functions. Cobalt is used to reduce the solubility limit of molybdenum and thereby increase the volume fraction of Mo-rich precipitates (e.g. Ni_3Mo, Fe_2Mo). Cobalt also assists in the uniform dispersion of precipitates through the martensite matrix. Cobalt accelerates the precipitation process and thereby shortens the ageing time to reach maximum hardness [6,16].

Molybdenum

Molybdenum provides good precipitation hardening by forming different precipitates. But Decker, Eash, and Goldman and other researchers [17-19] found that hardening when cobalt and molybdenum were present together was much greater than the sum of the strength increments produced when they were added separately. Due to low diffusivity, molybdenum effectively

reduces the size, suppresses coarsening of precipitates, enhances stability and increases the number density of low lattice precipitates. Molybdenum is the primary hardener in maraging steel. Ni_3Mo precipitate gives better toughness [5,20].

Titanium

Titanium along with small portion of aluminum around 0.25% to 0.3%, is present in T-type maraging steel to substitute cobalt. The strengthening precipitates in T type maraging steels is intermetallic compounds of NiTi or Ni_3Ti types with ordering structure [21, 22]. Titanium has negative influence on the plasticity and ductility, which is due to the distribution of titanium-containing intermetallic compounds primarily at prior austenite grain boundaries [23]. This negative influence is particularly characteristic of steels without molybdenum [24]. In this case the balance between titanium and trace elements such as carbon, nitrogen and sulfur in the matrix should also be considered to achieve a better fracture toughness [25, 26]. Titanium also refines grain structure and raises the creep strength of the material.

1.1.5 Microstructure of maraging steel

As mentioned above, maraging steel is forged involving martensitic transformation, followed by age hardening. General microstructure consists of many micro precipitates embedded within the martensite lath. Figure 1.2 and 1.3 shows the microstructure difference between maraging steel and general martensite steel.

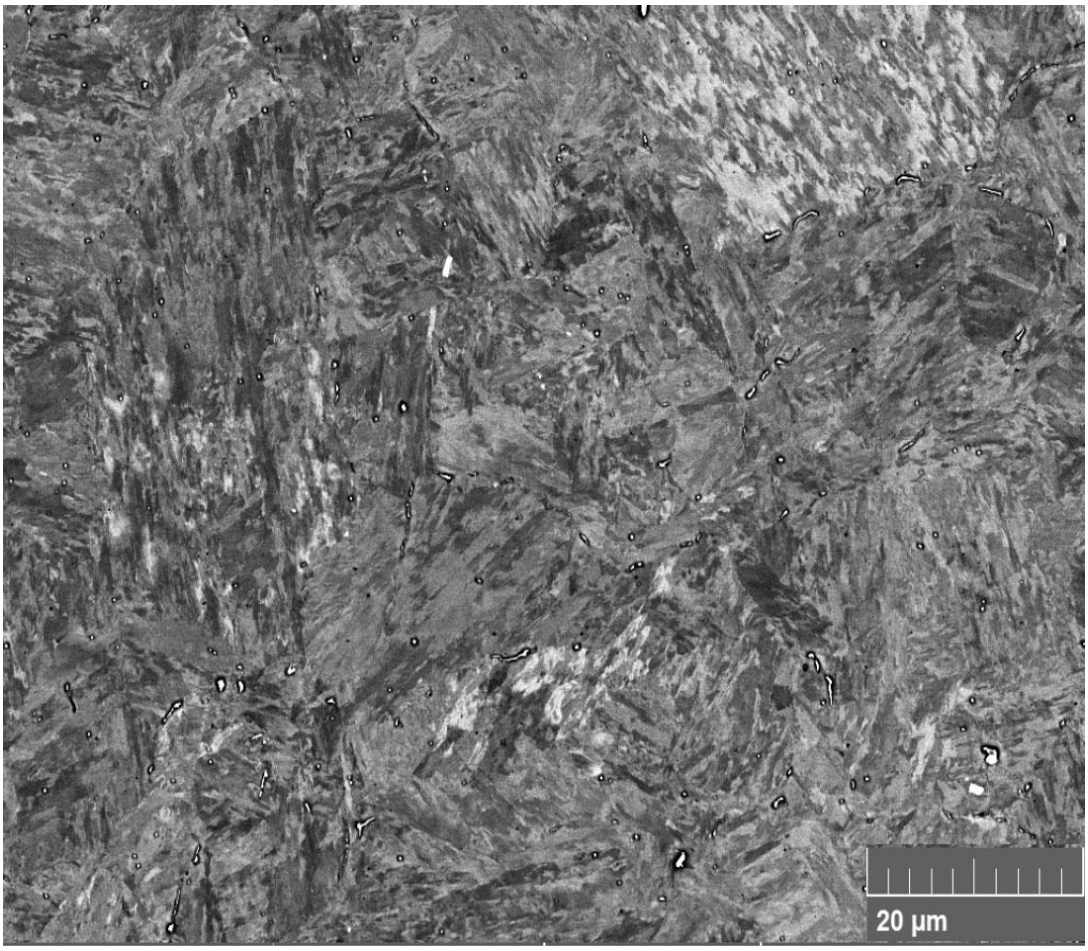

Figure 1. 2 Typical microstructure of maraging steel.

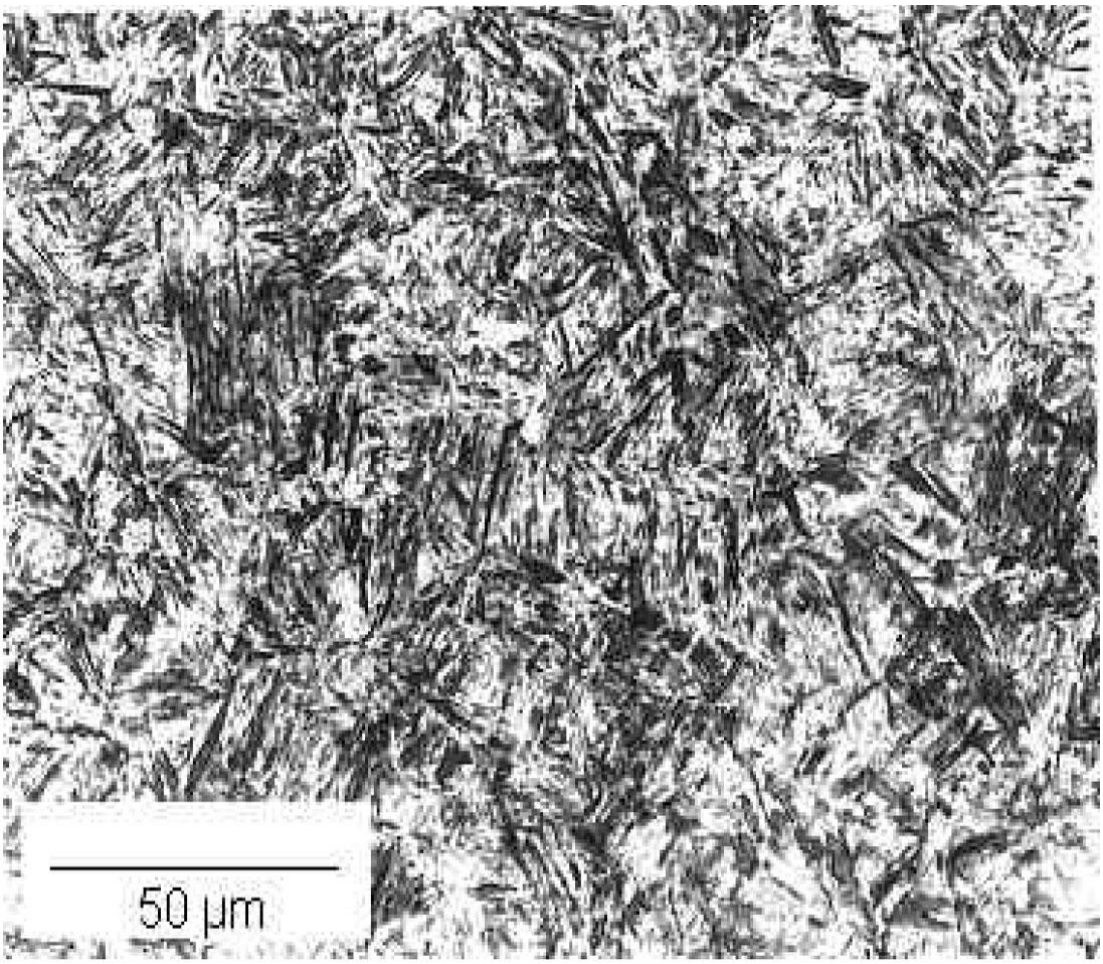

Figure 1. 3 Typical microstructure of general martensite steel.

Microstructure-martensite matrix

In many respects, the metallurgy of the maraging steels resembles that of the precipitation-hardening stainless steels Figure 1.4. The maraging steels have enough alloy content to lower the M_S temperature to near or below the room temperature. Austenite decomposition does not occur above the M_S temperature, which means neither pearlite nor bainite is formed. So, as mentioned in the production characteristics, the rate of cooling from high temperature is not important in hardening. The steels are hardened mainly by aging the martensite to promote precipitation hardening. The martensitic structure does not revert to austenite on heating until a temperature of

about 530 °C is exceeded. The steel was designed to be austenitic and, thus, soft and readily fabricated in the as-annealed condition. To harden this steel, the austenitic structure must transform into martensite. To develop maximum strength, the steel must be entirely martensitic before precipitating hardening. Cold working is known to raise the M_S temperature of austenitic iron alloys. Consequently, cold working may serve as a substitute after austenitization.

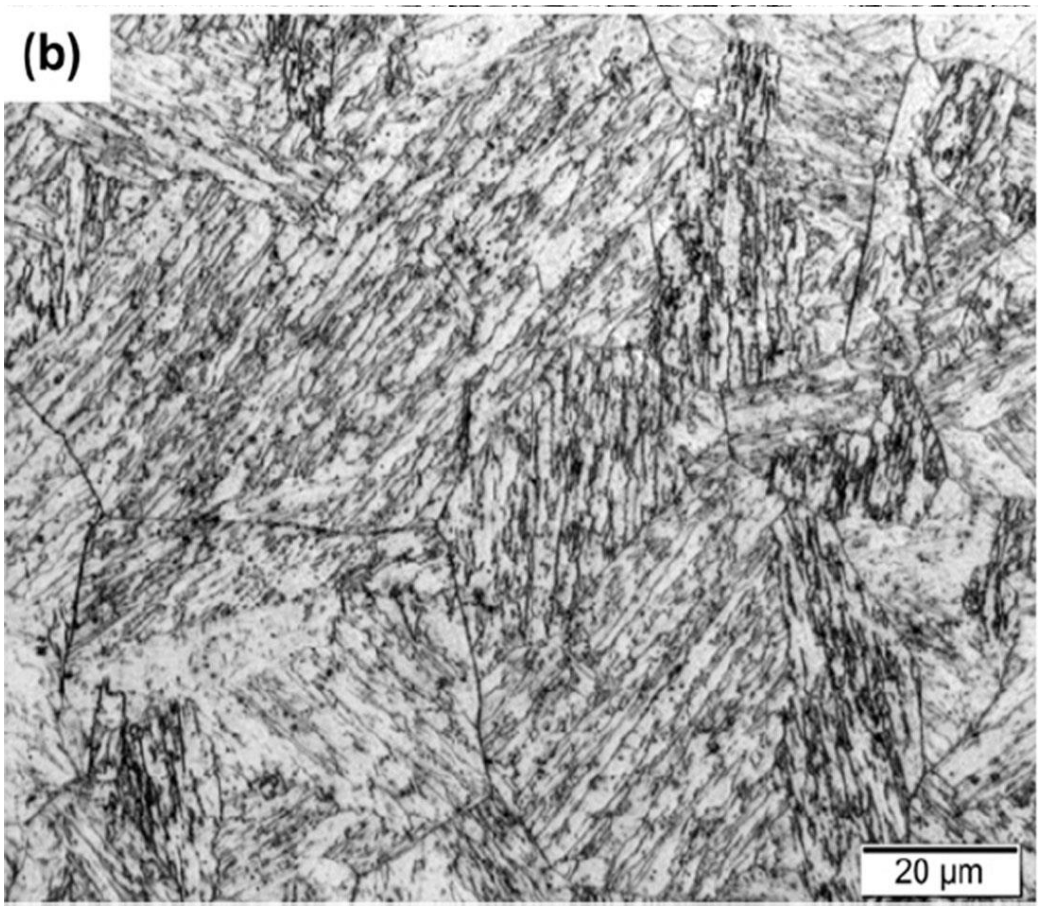

Figure 1. 4 Typical microstructure of precipitation-hardening stainless steels.

Microstructure-reverted austenite

In general, austenite in steels is derived from two different ways: (a) the austenite phase retained after cooling from the two-phase region is known as retained austenite, which has been investigated extensively in TRIP steels and (b) austenite phase which is formed by partial reversion from martensite on aging in the two-phase region at a lower temperature is defined as reverted

austenite [27-33]. In some maraging steels, reverted austenite was observed in the martensitic matrix on aging at high temperature. The reversion of martensite (α') to austenite (γ) is an important constituent that is believed to control the final structure and influence the mechanical properties. The reverted austenite in maraging steel exhibits different morphologies [32,33]. The morphologies of reverted austenite are closely correlated with alloy compositions and process parameters [33]. Reverted austenite in maraging steels generally appears either as elongated or granular shape. More specifically, reverted austenite is classified into three types, i.e. matrix austenite, lath-like austenite and recrystallized austenite [32]. Matrix austenite is defined as an austenite phase that either develops from retained austenite and thus has the same orientation or grows at the prior austenite grain boundaries and forms a single austenite grain (Figure 1.5(a)). Lath-like austenite can be generated along and within the martensite laths, thereby generating a lamellar structure of alternate austenite lath and residual martensite lath (Figure 1.5(b)). Recrystallized austenite normally nucleates at high aging temperatures or after long aging times and it is characterized by a polygonal shape with low dislocation density, as shown in Figure 1.5(c). In addition, in high Ni alloyed and Ti-containing maraging steels, a type of Widmanstätten austenite was reported to become dominant on aging at high temperatures for a long time [36,45]. Austenite can act as a sink for impurities by reducing N and P embrittlement during heat treatment. Transformation of austenite to martensite may occur during deformation, which also improves toughness.

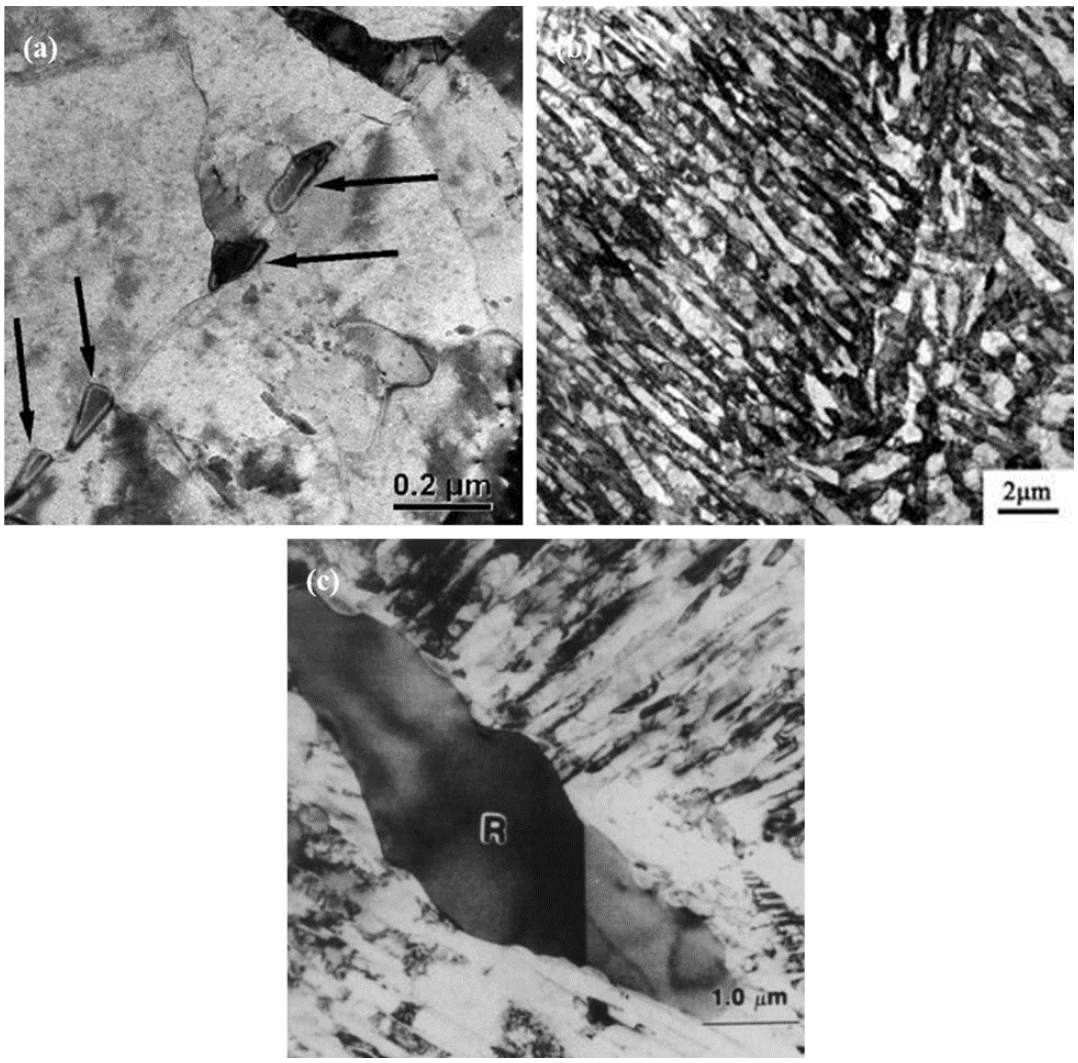

Figure 1. 5(a) Matrix austenite at prior austenite grain boundaries [34], (b) the lamellar structure of alternate lath-like austenite and residual martensite [46] and (c) a recrystallized austenite grain free of defects [33].

Microstructure-precipitates

Besides martensite matrix, characteristic of precipitates in maraging steel play another significant role in determining the mechanical properties. The precipitates in maraging steel are effective in restricting the movement of dislocations, and thereby promote strengthening by the precipitation hardening process. During initial development of maraging steel, researchers have shown great interest in precipitates present in maraging steel. With the development in the material

characteristic techniques like high resolution transmission electron microscope (HR-TEM) and 3D atom probe tomography (3DAPT), the extremely small precipitates can be characterized. The nature of intermetallic precipitates within maraging steel have been generally investigated, as shown in Table 1.2

Table 2.21 Phases in maraging steel [34].

Phase	Stoichiometry	Crystal structure	Lattice parameters
γ		f.c.c	a = 3.5852 Å
α		b.c.c	a = 2.8812 Å
μ	A_7B_6	rhombohedral	a = 4.751 Å
			α = 30.38°
ω	A_2B	hexagonal	a = 3.9-4.05 Å
			c = 2.39-2.48 Å
S	A_8B	hexagonal	a = 7.04 Å
			c = 2.48 Å
X	A_3B	hexagonal	a = 2.55 Å
			c = 8.30 Å
Fe_2Mo	A_2B	hexagonal	a = 4.745 Å
			c = 7.754 Å
Ni_3(Ti, Mo)	A_3B	hexagonal	a = 5.101 Å
			c = 8.307 Å
Ni_3Mo	A_3B	orthorhombic	a = 5.064 Å
			b = 4.224 Å
			c = 4.448 Å

For T type maraging steel most of studies show that Ni_3Ti(Mo,V,W)-type phases occurs during the very early aging stage following a more stable FeMo(W)-type phase is formed after long-term aging [34]. The formation of Ni_3Ti(Mo) type phases at the initial aging stage in conventional maraging steels have been proposed since the invention of the [4]. The modern techniques with atomic-scale resolution allow direct observation of nano-precipitates possible and finally confirm the existence of Ni_3Ti(Mo) phase (η-phase) in those steels. The morphology of Ni_3Ti precipitates was found to be needle-like [35,36], plate-like [37] or rod-like [35]. Ni3Ti precipitates exhibits hexagonal lattice with a = 2.55 Å nm and c = 4.2 Å [38]. Selected area electron diffraction (SAED) analyses indicate that the orientation relationship between ηNi_3Ti and α'-martensite matrix is $(011)\alpha' \| (0001)\eta$, $[1\bar{1}1]\alpha$, $\|[11\bar{2}0]\eta$ [39]. The formation mechanism of Ni3Ti is general considered as heterogeneous nucleation on dislocations followed by growth via pipe diffusion [39,40]. Researchers have varied opinions on the dominant strengthening effect of each type of precipitates in these steels. Some studies revealed that in maraging steels where both Ti and Mo were present, Ti was much more active in the beginning due to its higher diffusivity in martensite. Apart from the kinetic advantage, the smaller lattice misfit between Ni_3Ti and martensite and consequently a lower barrier for nucleation is another reason for the formation of Ni3Ti in the early stage of aging. Therefore, a sharp rise in hardness shortly after the onset of aging was usually observed in Ti containing maraging steels [34]. During the early aging stage, Mo is more likely to be incorporated into the Ni_3Ti phase and partially substitutes Ti atoms. As aging time increase the substitution reach limited and still sufficient Mo atoms left for the following formation of FeMo-type phases. Conversely, the growth of FeMo phase would consume the Mo atoms in Ni_3Ti(Mo) phase and therefore the stoichiometry of Ni_3Ti(Mo) becomes more closer to that of Ni3Ti. The activity of Mo has been shown to be strongly affected by other elements. The

presence of Co is generally found to promote the formation of Mo-rich precipitates. When Co is absent, the driving force for the precipitation of Mo-rich precipitate is significantly reduced. In this case, the precipitation of Mo-rich phases would take 3 to 8 hours to occur [41]. Thus, the major precipitates in Co-free maraging steels are entirely Ni_3Ti phase and thus higher Ti content is required to achieve the same level of precipitation strengthening. In addition, the stoichiometry of FeMo-type phase is still debated. Previous TEM and SAED studies suggested it as Fe2Mo Laves phase [39,41], whereas the compositional result by a more recent ATP analysis corresponded to Fe_7Mo_6 μ phase. Moreover, the possibilities of FeMo and Fe_3Mo_2 cannot be excluded as well. Apart from the primary Ni_3Ti(Mo)-type and FeMo-type phase, several other intermetallic phases may also form as well due to the composition variation in maraging steels.

In Ti-free maraging steels, the role of Ti is taken over by Mo. A precipitation sequence of Ni_3Mo followed by equilibrium FeMo-type phase was reported by Sha et al [41]. Besides, a type of metastable ω phase (ordered isothermal phase enriched in Ni, Co and Mo) was always generated before the formation of the more stable Ni3Mo phase. Researches revealed that this ω phase had a higher level of coherency with the matrix and hence was easier to form [42,43]. In addition, the precipitation of $Ti_6Si_7Ni_{16}$ (G-phase) was found to be responsible for the precipitation hardening of Cr-containing high-Si steels [44].

1.1.6 Low lattice misfit precipitates

A recent investigation with the maraging steel of composition Fe-19Ni-3Mo-1.5Ti has revealed the presence of nanoscale precipitates of hcp Ni_3 (Ti, Mo) and bcc B2 Ni (Mo, Fe) in the microstructure. Precipitates of the type Ni_3(Ti, Mo) possess a low misfit of 1% with the matrix [47]. The ultimate strength of this cobalt free maraging steel was 1850 MPa at static toughness of 110 MJ/m^3. This counterintuitive strategy for utilizing low lattice misfit precipitates with the

matrix strengthen alloys without sacrificing ductility draw attention worldwide. It is stated that ordering and modulus strengthening provides influence in improving the strength to the steel and major strengthening mechanism is the precipitation hardening. These low misfit high density precipitates contribute significantly to the toughness of the steel.

Lattice misfit also known as lattice mismatch describe the difference of two material lattice parameters. Low lattice misfit precipitates' lattice constant of the precipitate is similar or almost same as the matrix. It is preferred in the field of semiconductor industry in epitaxy process. This new research of low lattice misfit precipitates in T type maraging steel provided an alternative method in improving material strength as well as ductility.

The impact of low lattice misfit precipitates on material precipitation hardening mechanism is generally summarized as decreasing the nucleation barrier for precipitation and enabling nanoprecipitates with an extremely high density and small size Meanwhile, when deforming instead of conventional precipitate-dislocation interaction happens, the minimized elastic misfit strain around the precipitates provides chemical ordering effect that creates opposing forces when precipitates are cut by dislocations [47,48].

1.1.7 Evolution of precipitates and effect on strengthening

Generally, the precipitation process is described as successive nucleation and growth. So, the evolution of precipitates is required for in depth understanding to explain the effect of precipitates on strengthening mechanism.

Size of precipitates

During aging stage, the formation and coarsening of precipitates involves complex process including interaction mechanism of precipitates with dislocations, which is closely related to the size of precipitates. Several critical sizes are introduced to characterize precipitate during different

stages of precipitation. The critical precipitate radius (r_c) below which the precipitates will dissolve is usually determined by [49]:

$$r_c = 2c_a\Gamma/(c_0 - c_a) \tag{1.1}$$

where c_α is the solute concentration in the matrix phase during aging, c_0 is the solute concentration in the matrix before aging. The capillarity constant Γ is described as [49]:

$$\Gamma = \frac{\sigma_{\alpha/\beta} N_A \Omega\beta(1 - c_a)}{RT(c\beta - c\alpha)} \tag{1.2}$$

where $\sigma_{\alpha/\beta}$ is the interfacial energy per unit area between the precipitate and matrix, NA is Avogadro's number, Ω_β is the atomic volume of precipitates, c_β is the solute concentration in the precipitate, R is the idea gas constant and T is the absolute temperature.

The first critical precipitate radius r_{c1} is defined to distinguish the growth mechanism. When precipitate size is above $r_{c1,}$ the interfacial-limited growth is taken over by the diffusion-limited growth. After that, further precipitation results in another critical precipitate radius r_{c5} above which the diffusion-limited coarsening occurs.

As the interfacial free energy $\sigma_{\alpha/\beta}$ (Equation (1.2)) varies depending on the nature of coherency, two more critical sizes, $r_{c0\text{ and }}r_{c3}$, are introduced. r_{c0} is the critical radius below which precipitates will dissolve when the interface is coherent and r_{c3} is the critical radius below which precipitates will dissolve when the interface is incoherent. Another two critical sizes relating to the precipitation strengthening are also taken into consideration. r_{c2} stands for the critical radius above which the coherency strengthening starts to decrease, whereas r_{c4} indicates the critical radius

above which the interaction between dislocation and the precipitate transforms from shear-cutting mechanism to looping mechanism which we will discuss in following sections.

It's important to figure out the relationship between these critical sizes for us to fully understand the evolution of precipitates and its effect on strengthening mechanism. It is not difficult to understand that $rc1<rc5$ and $rc0<rc2<rc3$. As $rc0$ and $rc1$are very small, they are usually considered as zero [49]. In most cases, the Orowan looping occurs when precipitates are incoherent with the matrix, thus we can obtain $r_{c3} < r_{c4}$ (dislocation looping may also occur when the coherent precipitate is too large or strong to be cut through).

Evolution of precipitates

During the early stage of precipitation, the nucleus is surrounded by a supersaturated matrix with a higher solute concentration gradient which provides as the driving force for solute diffusion into nucleus and therefore promotes the precipitate growth. The growth rate of precipitates is governed by two parameters: the interface reaction and the lattice diffusion [50]. When the average size of precipitates is below r_{c1}, as the distance of diffusion field is rather short, the interface reaction is the rate-controlling step. The precipitate size is proportional to the aging time: $\bar{r} = r_{c0} + G_{0t}$ (Figure 1-7), where $G0$ is the growth rate during the interface-limited growth. In the case of larger precipitates ($r > r_{c1}$), the driving force for lattice diffusion gradually decreases owing to the continuous depletion of solute atoms in the matrix, the diffusion becomes the rate-controlling step [50,51]. The relationship between the precipitate size and growth time follows the equation [49,52]:

$$\bar{r} = (r_{c1}^2 + 2D\frac{c_0 - c_a^e}{c_\beta - c_a^e}(t - t_1))^{1/2} \tag{1.3}$$

where D is the diffusion coefficient in the matrix, c_0 is the initial solute concentration, c_a^e is the equilibrium solute concentration in the matrix, c_β is the solute concentration in the precipitate and $t1$ is the time the diffusion-limited growth starts.

At the end of the diffusion-limited growth period, Equation (1.3) cannot describe the dynamic evolution of precipitate size anymore which indicates that the diffusion-limited coarsening initiates. It is difficult to draw a line to distinguish the diffusion-limited growth and diffusion-limited coarsening. The diffusion-limited growth process is defined as the stage when the solute obtained by precipitates is from the matrix; while for diffusion-limited coarsening, the solute is from the dissolving of smaller precipitates. According to the Gibbs-Thomson equation [60], the solubility of smaller precipitates which possess a larger ratio of surface area to volume is higher than that of larger precipitates. This size-dependent solubility results in a further size-dependent driving force for coarsening. Based on the Gibbs-Thomson equation, the growth rate is positive for large precipitates with $\bar{r} < c_R$ and negative for small precipitates with $\bar{r} > c_R$, namely, larger precipitates grow at the expense of smaller precipitates which dissolve back into the matrix. Therefore, the coarsening process is described by the decrease of number density and the broadening of size distribution. But coarsening may take place simultaneously with the growth process or even in the nucleation stage if the initial solid solution supersaturates [51]. In addition, due to the increase in the distances of diffusion field, the size increment rate in the coarsening stage is slower than that in the growth stage (Figure 2-5). The precipitate size in most coarsening process obeys the LSW (Lifshitz and Slyozov [53] and Wagner [54]) theory which suggests the time exponent is 1/3 (Figure 1.7).

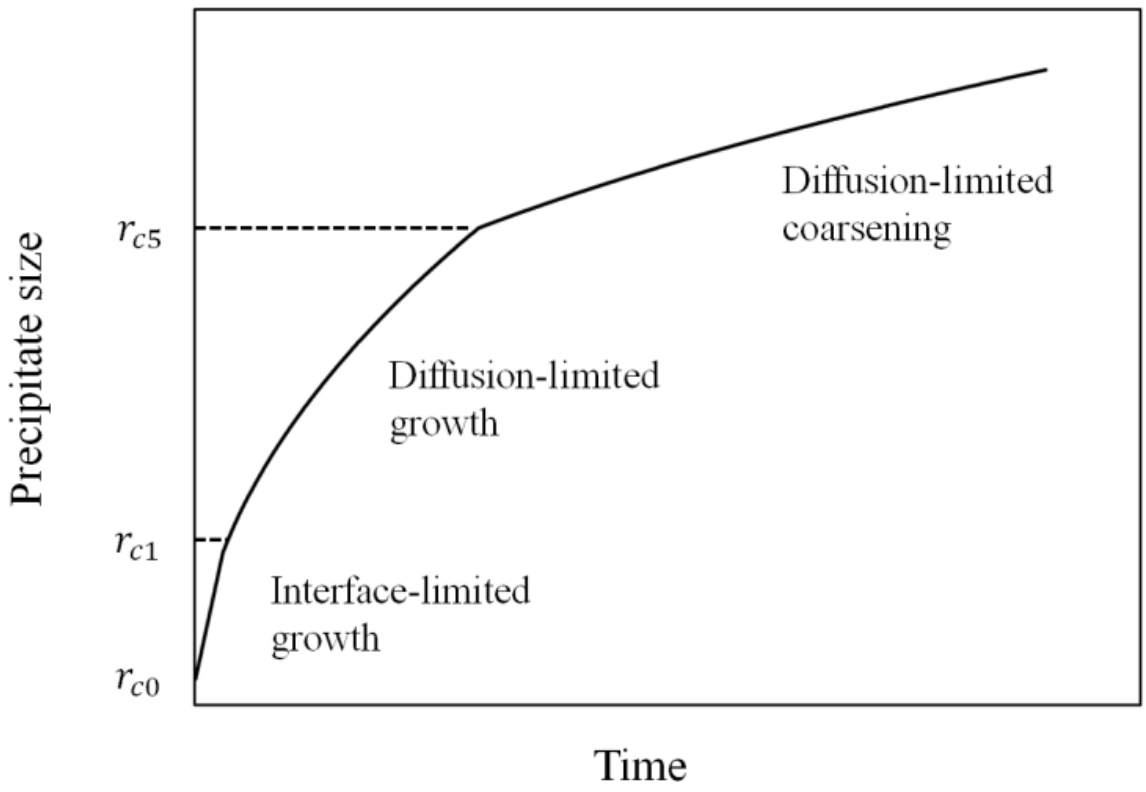

Figure 1. 6 The evolution of precipitate size during aging in terms of precipitation kinetics [49].

Precipitate coarsening theory

Precipitate coarsening is the most unfavorable thing in precipitation strengthening of materials became coarsening not only drastically increases the size of precipitates but also reduces the density and has negative impact on precipitate distribution within the matrix. Lifshitz and Slyozov, Wagner [53,54] developed a theory attempting to interpret the diffusion-limited coarsening named as LSW theory which has been proved experimentally [51,55].

LSW theory is developed based on following per-assumptions:

1. Dilute solution theory applies and the linearized version of the Gibbs-Thomson equation is valid.

2. Diffusion field of precipitates do not overlap and the particles only interact with the matrix, thereby limiting the precipitate volume fraction to zero.

3. Coarsening takes place in a stress-free matrix.

4. Precipitates possess a spherical morphology.

5. The composition of precipitates is same as given by the equilibrium phase diagram.

Based on the above assumptions, the LSW theory provides three equations to describe the diffusion-limited coarsening. The first equation predicts the increase of average precipitate radius, $\bar{r}$, with respect to the coarsening time according to:

$$\bar{r} = (r_{c1}^2 + 2D\frac{c_0 - c_a^e}{c_\beta - c_a^e}(t - t1))^{1/2} \tag{1.4}$$

where D is the diffusion coefficient in the matrix, c_0 is the initial solute concentration, $c\alpha e$ is the equilibrium solute concentration in the matrix, c_β is the solute concentration in the precipitate and t_1 is the time the diffusion-limited growth starts.

The second equation reveals that the decrease in the precipitate number density, N_V, follows:

$$NV \cong \frac{3f_p}{4\pi}\frac{1}{K_R F_3}t^{-1} \tag{1.5}$$

where fp is the volume fraction of precipitate, KR is the coarsening rate constant in Equation (1.4) and f_3 is the third moment of the time-independent precipitate size distribution function $f(r/\bar{r})$ when $V_p \rightarrow 0$

The relationship between the solute concentration within the matrix, c_i^a, and coarsening time is derived:

$$\Delta c = \frac{9(c_\beta^e - c_a^e)}{4D} K_R^{2/3} t^{-1/3} \tag{1.6}$$

Most of these experimental studies revealed that the experimental roughly fitted LSW theory. However, experimental results also indicated that the size distribution function was much broader than that of the theoretical $f(r/\overline{r})$. This deviation has later been demonstrated to be associated with the non-zero volume fraction of precipitate in reality. Therefore, many studies have been carried out to modify the LSW theory for better application in cases where the volume fraction of precipitate has to be taken into consideration. The major challenge is to determine the effect of interparticle diffusional interactions on the coarsening behavior of a precipitate with a specific size. According to the modified theories [56-59], with the increase of precipitated volume fraction, the average distance of diffusion field become shorter and thus the concentration gradients will be larger, thereby resulting in the increase of the coarsening rate. Besides, the local diffusional interactions give rise to spatial correlations between adjacent precipitates which further leads to the broadening and symmetry of size distribution function.

Effect of precipitate size on precipitation strengthening

Precipitation strengthening is usually utilized to describe the strength increase during the ageing stage and precipitation occurs. During The early stage of aging (under-aged), with the growth of coherent precipitates, the strength with shear-cutting mechanism increase. While in the overaged stage, the coarsening of precipitates results in incoherency and thus activates the looping softening mechanism. Even though at over aging stage we used softening to describe the decrease of strength but the strength at both stages is higher than that before aging, therefore both the mechanisms are defined as strengthening mechanisms.

Although the softening during the overaged period is generally considered to result from loss of coherency, a number of studies have shown that the extremely large coherent precipitate

and the modulus difference between the precipitate and matrix can also lead to the decrease of strength. In the case of large precipitates, considerable flexing of dislocation occurs owing to the increase of the interparticle spacing (assuming the volume fraction of precipitate is constant), thereby resulting in the coherency softening. Namely, the coherency softening may occur before the loss of coherency. Another possibility is the modulus difference, which is suggested to result in softening as well, but so far there is no experimental evidence to support this viewpoint yet [49].

The strengthening mechanism is only associated with the precipitate size regardless of how the precipitate approaches the critical size, by growth or coarsening. It means that $rc2$ and $rc4$ are irrelevant to $rc5$. But according to Sha and Guo's conclusion [49], the value of $rc2$ should be somewhere between $rc1$and $rc5$.

Based on the discussion, a more comprehensive precipitation-strengthening process is comprised of three stages: when the precipitate is small, coherency strengthening takes effective by cutting mechanism, the strengthening effect increases with the precipitate size; with the growth of precipitate size, the stress required to cut through precipitate is so high that Orowan looping mechanism takes place. Orowan strengthening is inversely related to the interparticle spacing, so initially the precipitate growth which reduces the interparticle spacing leads to the Orowan strengthening. The coarsening of precipitates decreases. The number density and thus the increase of interparticle spacing results in the Orowan Softening mechanism. On the other hand, the structure of the interface is also very important. For example, if the precipitates are small but have incoherent interface, the looping mechanism takes place. Conversely, if the precipitates have a large size but coherent interface and a small misfit strain, the shearing will be the dominant mechanism.

It is worth emphasizing that apart from the coherency mechanism and modulus mechanism, there are more strengthening mechanisms, such as chemical (softening), stacking fault (strengthening), order (strengthening), etc. which we will discuss specifically in chapter 3.

1.2 MEDIUM MANGANESE STEEL

Recently, there have been concerns about lightweight high-strength steels becoming the most concerned issue in the automotive industry in terms of improving fuel efficiency, reducing vehicle exhaust emissions, and improving vehicle safety. In order to meet these requirements, many steels have been proposed such as: DP steel (dual phase) steel, TRIP steel (variable) Plastic deformation, plasticity, and TWIP steel (twining induced plasticity) Figure 1.7 [60]. However, due to the large amount of expensive alloying elements and the cumbersome processing that needs to be carried out, it is difficult to apply this effect to the production of steels for motor vehicles at reasonable prices [60]. In the past decade, medium Mn steels have been actively investigated due to their excellent balance between material cost and mechanical properties.

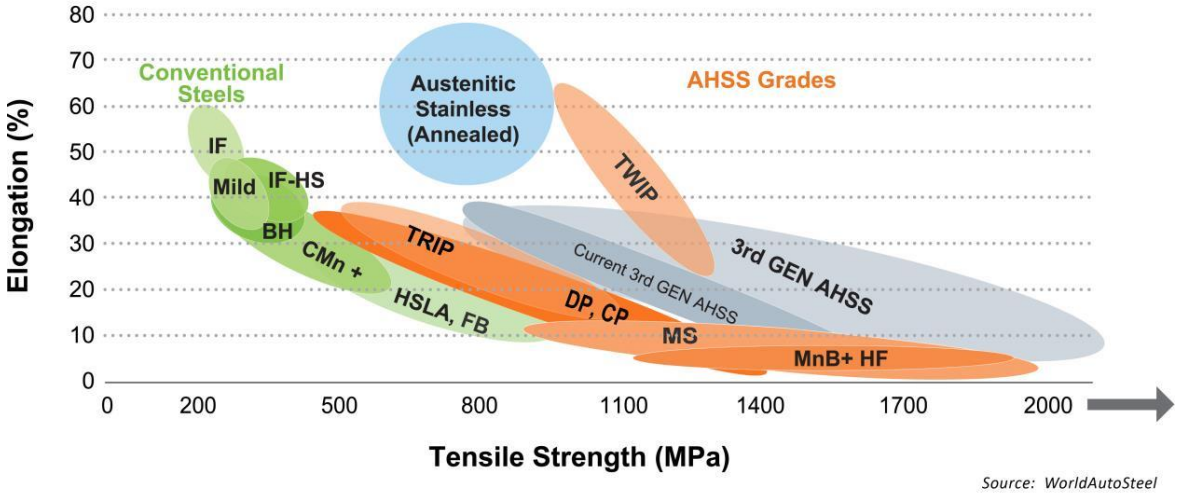

Figure 1. 77 Global tensile strength-elongation profile for various kinds of steels [60].

1.2.1 Type of medium manganese steel

The manganese content of the steel is about 5%, between low and high manganese steels (3% < Mn < 9%). As one of the austenite forming elements, manganese can effectively expand the austenite phase region and increase the austenite content and its stability [61].

The current medium manganese steel can be divided into three categories:

The first type of medium manganese steel is obtained by inverse transformation on the basis of martensite to obtain ultrafine crystal ferrite and austenite structure. In this and alloy systems, the strengthening of manganese is achieved by obtaining martensite structure, and martensite transforms into ultrafine grained ferrite and austenite structure during subsequent reverse transformation.

The second type of medium manganese steel is obtained on the basis of the reverse transformation of martensite to obtain two kinds of grain size distribution structure, which is ultrafine grained ferrite and austenite structure and coarse δ ferrite. In this alloy system, Al is mainly to prevent delta ferrite transformation. The high-temperature austenite portion is transformed into martensite and reverse-transformed into austenite after annealing in the subsequent two-phase region to obtain ultrafine-grained ferrite and austenite structure.

The third type of medium manganese steel is characterized by re-dissolution of carbides and bi-grain size distribution, namely ultra-fine-grained ferrite and austenite and coarse delta ferrite. Since this alloy system contains a large amount of Al, the density of the steel sheet is low. A relatively high C content will result in carbides during processing.

1.2.2 Designing advanced high-strength steel

At present, designing of advanced high-strength steel structure is mainly divided into 2 directions: phase regulation, by controlling the shape, proportion, size, distribution of different phases in material, especially though grain refinement to improve the mechanical properties. The second focus is on the mechanical properties of each individual phase in material, such as increasing the strength of the BCC phase and improving the FCC phase stability, improve the TRIP(transformation induced plasticity) effect of retained austenite during the deformation process and TWIP (twinning-induced plasticity) effect. Here we summarize a few representative advanced high-strength steels: TRIP steel, super-strong bainite steel, Q&P steel and medium carbon manganese steel, etc. to better facilitate the understanding of advanced high-strength steels.

TRIP steel

TRIP (transformation induced plasticity) steel was discovered by Zackay [62] in 1967 during the study of high nickel and high chromium stainless steel. Due to the original TRIP steel contains a large amount of expensive alloying elements such as nickel and chromium, its application is greatly limited. At the end of the 1880s, the emergence of low-cost C-Si-Mn TRIP steels [63] promoted the development of low-cost TRIP steels [64, 65]. The emergence of this type of steel provides a new way to improve the strength and plasticity of steel. Today's TRIP steels are mainly concentrated in the field of low-alloy high-strength steels with a composition range of 0.1~0.4wt.% C, 1.0~2.0wt.% Si, 1.0~2.0wt.%Mn. In addition, in order to increase the strength, the addition of Nb, V, Ti and other elements, using solid solution strengthening and precipitation strengthening, regulates balance between strength and plasticity. However, with high content of Si, the surface quality of the steel plate is rough [66] so Al was added by some researchers into the

TRIP steel to replace Si to inhibit the precipitation of cementite during the low temperature isothermal process [67, 68].

The typical production methods of TRIP steel mainly include hot rolling and cold rolling [69, 70], and the production process is shown in Figure 1.8. The hot-rolled TRIP steel is produced as follows: The steel is heated to high temperature austenitization zone, and after rolling in the austenitization zone, it is slowly cooled to the dual-phase zone for isothermal treatment. During this time, some of the austenite transform to ferrite and the alloying elements are initially enriched in remaining austenite, then the material is rapidly cooled to below 500 ^{o}C (bainite region). Note that the reason for applying quick cooling is to avoid the formation of pearlite, because the cementite in pearlite will use a large amount of C and reduce the stability of retained austenite. In this process, the transformation of bainite will occur, producing a certain proportion of bainite and the alloying elements are further enriched in retained austenite obtain austenite to stabilize austenite. Finally air-cooled to room temperature to obtain a multi-phase structure composed of ferrite, bainite and retained austenite. In industrial production, “two-stage slow cooling” is used instead of “two-stage isothermal”. The key to hot-rolled TRIP steel production is the control of the two slow cooling stages after hot rolling. As for cold roll process, cold rolling is applied after initial hot rolling and reheated to dual-phase zone and following sequences same as hot rolling process. During the cold rolling, strain in the microstructure provides nucleation energy for reverted austenite formation.

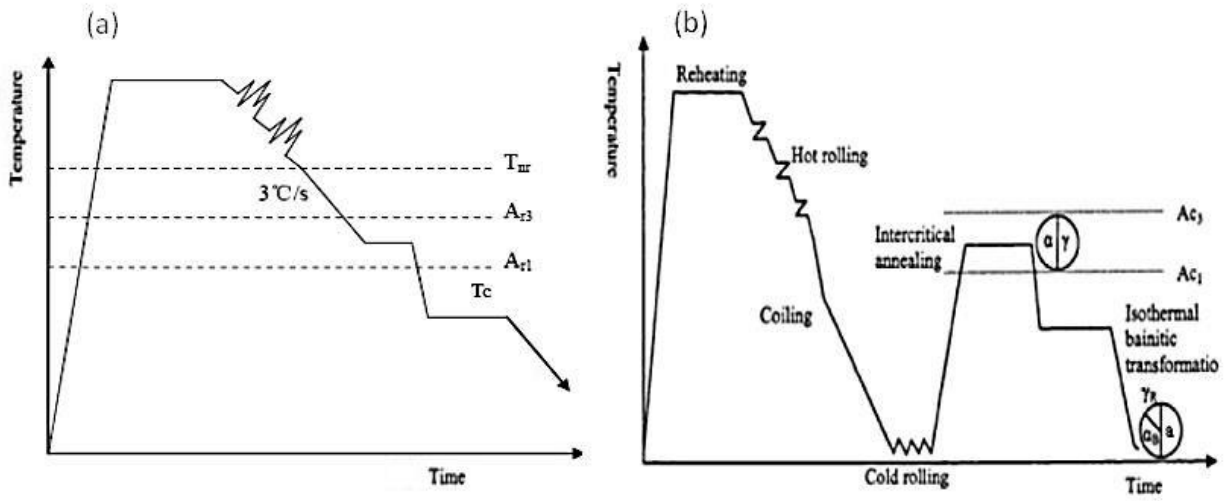

Figure 1. 88 Schematic diagram of the heat treatment process of hot rolled TRIP steel (a) and cold rolled TRIP steel (b).

The idea of both cold rolling and hot rolling TRIP steel is to enrich C in austenite to improve the stability of austenite at room temperature and eventually form multi-phase structure (consisting of ferrite, bainite and retained austenite), as shown in Figure 1.9. Due to the TRIP effect of retained austenite, this type of steel achieves high strength, high elongation, good formability and ideal strain hardening index.

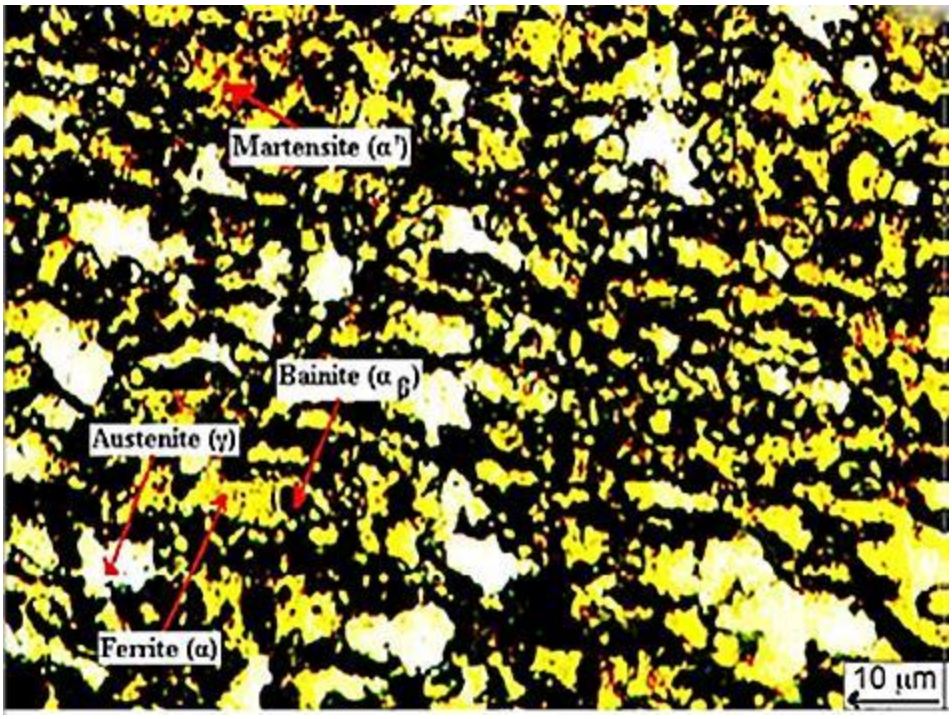

Figure 1. 99Typical microstructure of TRIP steel

Nanostructured bainite steel

Bhadeshia et al. [71,72] successfully developed a new type of ultra-high-strength nano-bainitic steel with a tensile strength of 2.5 GPa through a combination of composition design and heat treatment. Chemical composition (wt%) of the steel was: 0.8~1.0C, 1.5Si, 2.0Mn, 1.0Cr, 0.25Mo, 0.1V [71]. The heat treatment of nano-bainitic steel is as follows (Figure 1.10): steel is homogenized to fully austenitize, then it is cooled to the bainite transformation temperature region (125-250^{o}C) for long time (2-60 days) isothermally and finally cooled to room temperature.

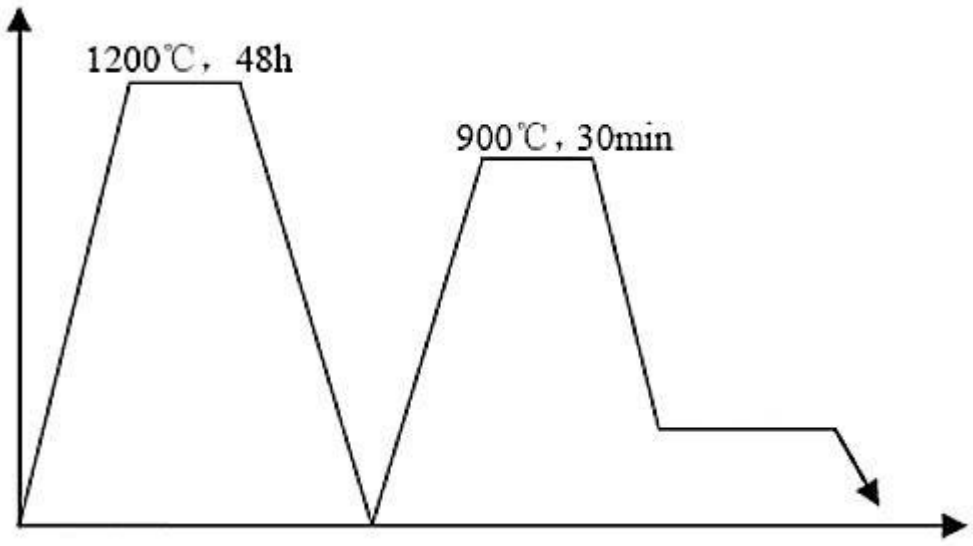

Figure 1. 10[10] Schematic diagram of the heat treatment process of nano-bainitic steel.

The microstructure of nano-bainitic steel is nanoscale (20-40 nm) ultra-fine slab-like bainitic ferrite and a large number of film-like residual austenite (Fig. 1.11). Although the strength of the nano-bainitic steel is very high, its heat treatment makes the production efficiency low, which restricts the development of the steel. Bhadeshia et al. added Co and Al [70] to the original alloy composition to shorten the bainite isothermal heat treatment time to less than 10 days. Nevertheless, longer heat treatment time is still the main problem that restricts its engineering application. Meanwhile, the higher carbon content also limits its thermal stability and weldability. Caballero et al. [72] modified the chemical composition (wt.%) of nano-bainitic steel to 0.2~0.3C, 1.5 Si, 1.5-2.0Mn, 1.5Cr, 0.25Mo, and replaced the original heat treatment with air cooling which makes the entire heat treatment process easier to achieve in industrial production. With this process, the tensile strength can reach up to 1.8 GPa with at least 18% elongation.

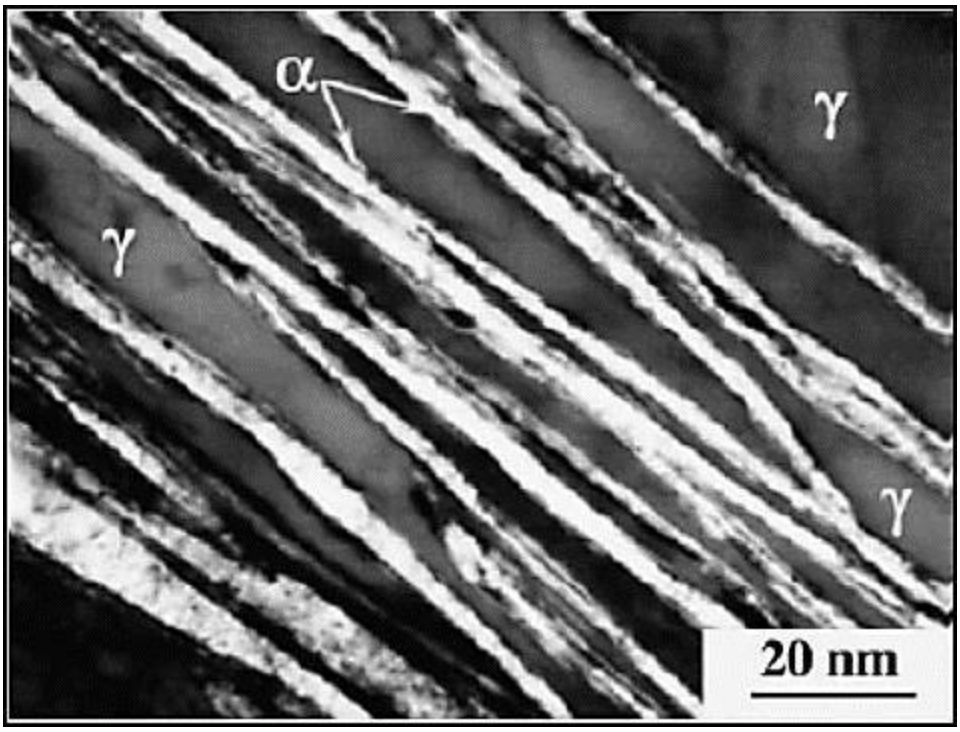

Figure 1.11[11]Typical microstructure of nano-bainitic steel.

The idea of nanostructured bainite steel is to obtain ultra-fine lath microstructure though low temperature bainitic transformation and the high dislocation density within the lath, provides ultrahigh strength.

Q&P steel

Speer et al. [73-76] developed a new process for heat treatment of martensitic steels called quenching and partitioning process (Figure 1.12) [77-79], using medium and high carbon silicon-containing steel. As shown in figure 0.35C-1.3Mn-0.74Si is heated to austenite zone for complete austenitization and it is rapidly cooled to a temperature T_Q between Ms-Mf. Then heated to a certain temperature above Ms T_P for isothermal treatment, finally cooled to room temperature, a multiphase structure composed of martensite and retained austenite is obtained, which has comprehensive mechanical properties (high strength, high plasticity). The characteristic structure

is shown in Figure 1.12. C_i, C_γ and C_m represent the carbon content in the original alloy, austenite and martensite, QT and PT represent the initial quenching temperature and the isothermal carbon partitioning temperature respectively.

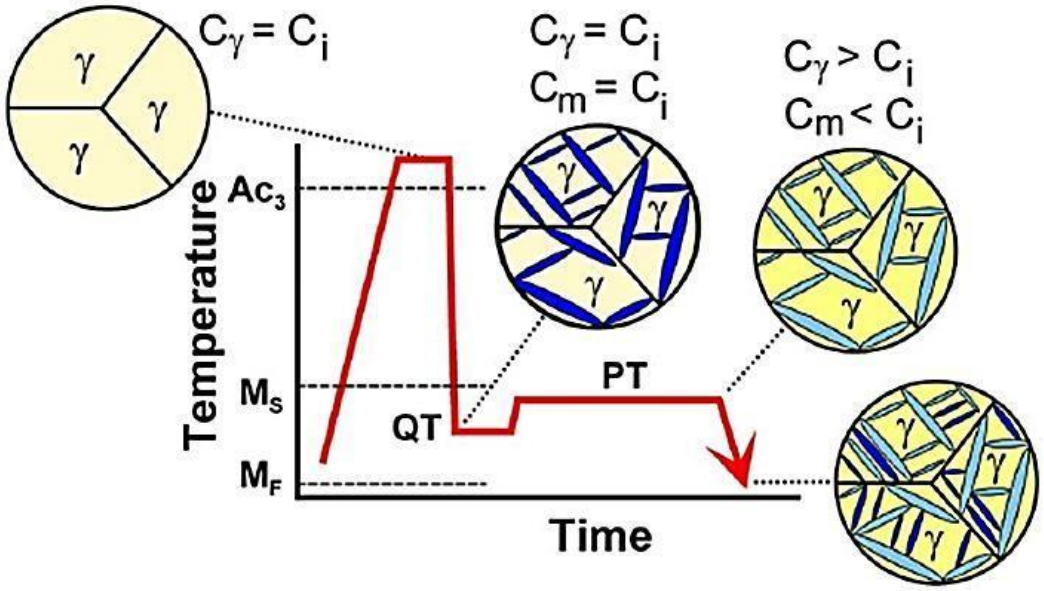

Figure 1. 12 Schematic diagram of Q&P process [76-78]. **12**

The Q&P process is identical to the traditional process of quenching-tempering (cooling speed and holding temperature) with some minor differences: in the Q&P process, quenching is incomplete and at the end of quenching, a certain amount of retained austenite remains in the microstructure. In the isothermal partitioning process, C atoms are enriched from martensite to retained austenite without phase transformation, thereby improving the stability of retained austenite. New martensite is produced during the subsequent cooling process, and part of austenite is preserved at room temperature. Si element is added in order to transfer enough carbon from the supersaturated martensite into the austenite through inhibits the precipitation of cementite.

Q&P steel is comparable to that of conventional quenched and tempered martensitic (M) steel in strength but has better plasticity. Q&P tempering proposed by Xu et al. [80, 81] has made full use of the precipitation strengthening effect of alloy carbides, and the strength is above 2 GPa,

and the plasticity is higher than 10%. However, the precipitation of carbides consumes a part of the carbon atoms, which reduces the carbon content in the retained austenite, which affects the austenite stability and the elongation of the material to some extent. Therefore, the high carbon content Q&P and Q&P-T steel has become one of the development trends [82, 83].

ART medium manganese steel

Morris et al. [84, 85]. found that in low-carbon steel with Mn content of 5% (wt), high content austenite with ultra-fine ferrite can be obtained through Austenite Reverted Transformation (ART). Figure 1.13. ART treatment is to heat the martensite structure obtained by quenching between Ac1-Ac3 for annealing at different times. Austenite nucleation occurs (reverse transformation) during annealing. A stable austenite, ultrafine ferrite and a multiphase structure of precipitated phase are obtained. One of the most important features of the ART process is that the martensite structure formed in quenching is reheated to a large amount of stable austenite and ferrite (degenerate martensite) multiphase structure. It is necessary to suppress the excessive coarseness of the martensite lath during the austenite reverse transformation annealing, austenite stabilize elements are required (Mn, Ni, etc.) considering relatively slow diffusion rate. At the same time, carbon can greatly improve the stability and matrix strength of metastable austenite and is also an essential element for alloying of ART process.

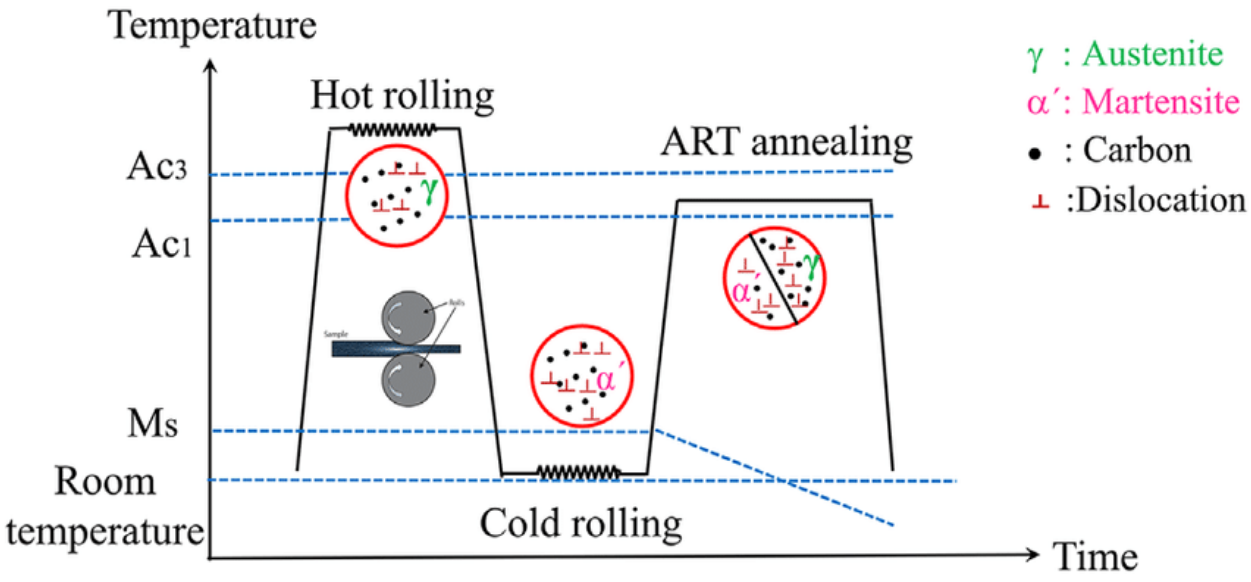

Figure 1. 13 Schematic diagram of ART process

All these advanced high-strength steels have one thing in common is that the focus is on the retained austenite and increasing austenite ratio and stability is significantly influences the mechanical properties. Also, we can find that in the effect of "double enrichment" to improve the stability of retained austenite is higher than that of "single enrichment". For high-performance structural steels, to control the stability of retained austenite in a low-carbon low-alloy component system, it is necessary to obtain enough stability of the retained austenite by multi-step enrichment of the alloying elements. However, high temperature distribution and multi-step distribution, which inevitably reduces the strength of the BCC phase, are problems that must be considered.

1.3 SUMMARY

In this chapter, we introduced maraging steel and medium manganese steel and their recent development. Based on the above discussion, we proposed a strategy in my research of obtaining high strength and high ductility in maraging steel and medium manganese steel (a) by utilizing different heat treatment parameters to obtain nano-scale low lattice misfit precipitates to achieve good combination of mechanical properties and (b) establish the relationship between heat

treatment parameters, mechanical properties and microstructures and understand the strengthening mechanisms and deformation behavior of cobalt-free maraging steel. Furthermore, elemental partitioning in retained austenite and microstructure refinement in medium manganese steel was studied.

Chapter 2: Material and experimental methods

2.1 ALLOYS AND PROCESSING DETAILS

In maraging steel research, commercial T-250 maraging steel was used. 19Ni3Mo1.5Ti maraging steel (referred as T-250) ingot with a nominal composition of Fe-19Ni3Mo1.5Ti0.3Cr0.1Al0.007C was prepared by combining vacuum induction melting and vacuum arc melting, using high purity (99.9 at%) alloying elements. Aluminum and chromium were added to enhance oxidation and corrosion resistance. The content of P and S was controlled to 0.005 wt%, and the conditions of O, H and N were limited to below 5 ppm. The ingot was forged as thick plates at 1200 ºC, and annealed in an Ar atmosphere for 60 min, followed by air cooling (AC) to room temperature. Fig 2.1 illustrates the relationship between ultimate tensile strength and total elongation and the raw material cost for the experimental maraging steel and compared with other high-strength steels that are being developed or are currently available [86-92].

In medium manganese steel research, the nominal chemical composition of experimental steel was Fe-0.22C-4.88Mn-1.59Al. Mn is the primary alloying element in the experimental steel. The reason for higher carbon content as compared to our recent study on MSP [93] is to study the effect of carbon on tempering in MSP steel. Al was added to inhibit the formation of cementite. Steel was melted in vacuum and cast into ingots of ~80 mm thickness. The ingots were homogenized at 1200 ºC for 2 h, and hot rolled to 12 mm thick strip using several passes with minimum reduction of 20% per pass. Detail heat treatment parameters of medium manganese steel are given in chapter 7.

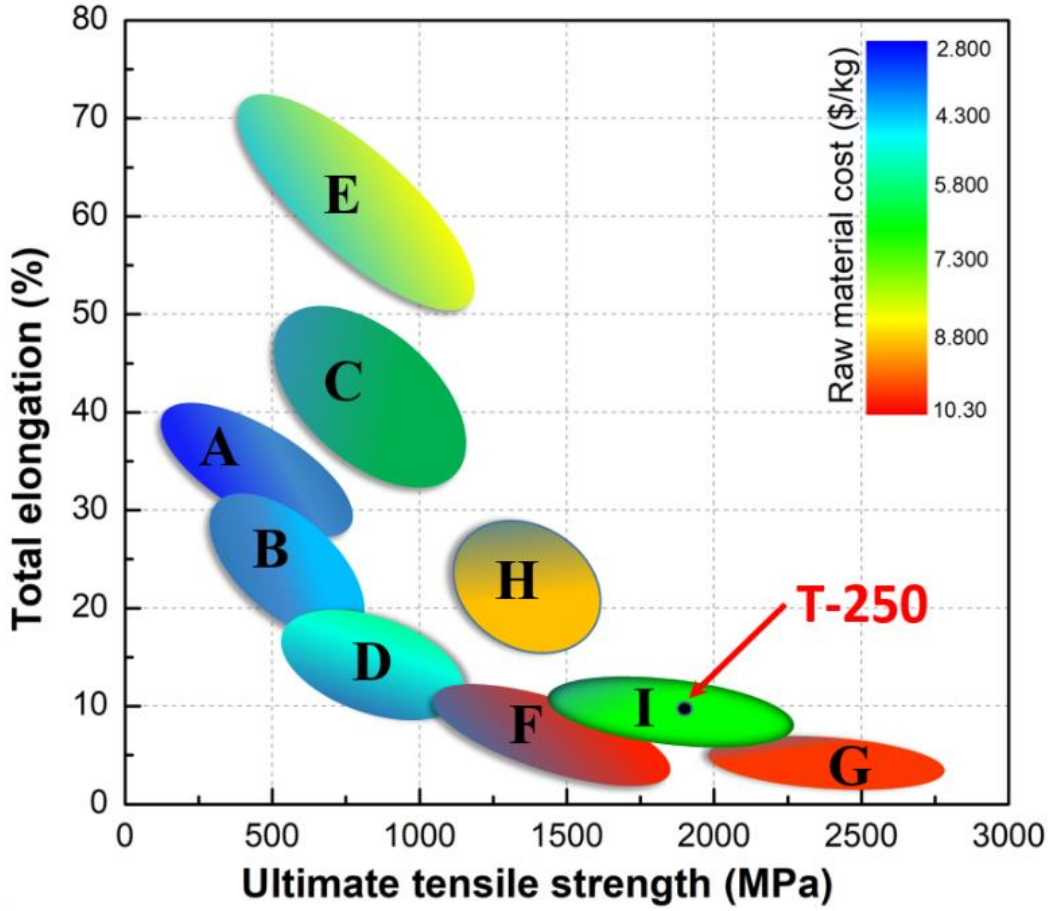

Figure 2. 1 Typical high-strength steels evolution and comparison of raw material cost (A-single phase ferritic steel, B-dual phase steel [88], C-austenitic stainless steel [89], D-TRIP and complex phase steel [90], E-advanced TWIP and TRIP steel [91], F-maraging stainless steel [92], G-Co-containing maraging steel [87], H-maraging TRIP steel [86] and I-Ti-strengthened maraging steel [87]).

2.2 SAMPLE PREPARATION

2.2.1 Cutting, grinding and polishing

All hot-rolling and heat-treatment pieces for characterization were cut from bulk samples after each processing procedure. To avoid deformation-induced phase transformation, all the aged materials were cut by Buehler ISOMET 2000 Precision Cutting with feeding speeds of 5- 10 mm/s.

Small pieces of samples were then hot mounted for optical and scanning electron microscopy (SEM) observation. Samples without mounted were prepared for X-ray diffraction (XRD) and transmission electron microscopy (TEM) analyses. Mechanical grinding and polishing process with extremely care to make sure produce good image. The grinding operation was carried out successively on 240, 400, 800 and 1200 grade silicon carbide papers with running water. The polishing operation was performed by AutoMet™ 250 Grinder-Polisher from 9 μm to 3 μm polishing cloth with corresponding diamond suspensions. All the samples were rinsed and dried with isopropanol after each step and final cleaning was done using ultrasonic agitation.

The 2% nital is the most widely used etchant for general steels. In this study, 2% nital worked effectively on medium manganese steel but not on maraging steel samples. Eventually maraging steel were etched with modified Fry's regent (50ml HCl + 25ml HNO3 + 1g CuCl2 + 150ml H2O) to better reveal the microstructure.

2.2.2 TEM thin foil preparation

TEM thin foil samples were prepared in electropolishing. The bulk samples were manually ground to foils below 150 μm thick. Disks with a diameter of 3 mm were then punched and further thinned to 50-80 μm. Electropolishing was conducted with solution of 5% perchloric acid and 95% ethanol at -20 ^{o}C. within the twin-jet electro polisher operated at 25-35 V (being adjusted to ensure the current of ~40 mA). The whole process lasted approximately 2-3 minutes depending on the operation parameters (such as temperature, jet speed and sensitivity, etc.) and stopped once the foil was perforated.

2.2.3 EBSD sample preparation

EBSD samples were prepared from as-polished bulk material. After mechanical polishing, electro-polishing within a solution of 10% perchloric acid and 90% ethanol at a voltage of 25 V was applied to remove the surface roughness and stress.

2.3 CHARACTERIZATION TECHNIQUE

2.3.1 Tensile testing

The tensile tests were carried out on ASTM E8 standard specimens using an MTS testing machine. The machine has a fixed lower jaw and a movable upper jaw to hold the dog-bone samples for testing. Once the sample is fixed, the load is set to zero to neglect force set manually because the load set by fixing the sample hand tight is not the original load. An extensometer set helps in finding the instantaneous change in the cross-section during the test on the specimen while the strain is extracted. The standard geometry followed for the tensile specimen are shown in figure 2.2.

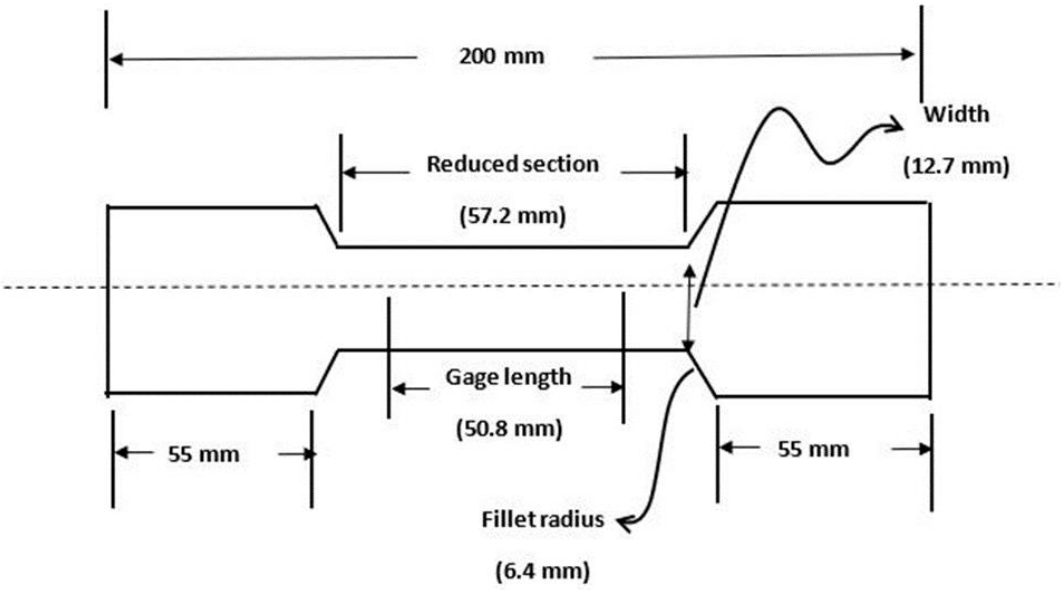

Figure 2. 2 ASTM E8 standard dimensions and geometry of a flat tensile specimen [94].

2.3.2 Microstructure characterization

Optical and scanning electron microscopy studies were applied and micrographs were taken at selected locations in all the tests using a Nikon optical microscopy (OM), TM-1000 back scattered electron microscope, and field-emission scanning electron microscopy (SEM).

Transmission electron microscopy (TEM) was completed to distinguish the constituent phases and precipitates in maraging steel and differentiate nano phases in medium manganese and look at the dislocation structure inside the grains, its size and distribution. Hitachi H9500 TEM and FEI Tecnai G2 F20 transmission electron microscope were used in 200 kV.

2.4 PHASE VOLUME CALCULATION BY XRD

X-ray diffraction work was performed on Bruker D8 Discover using Cu Kα radiation (λ = 1.54178Å) at the condition of 40 kV and 40 mA. Samples were step scanned (0.02° per step) by a beam size of 0.2 mm covering a range of 2θ angles. For quantitative phase analysis, more than two

sites of each sample were scanned. XRD data were collected by DIFFRAC plus XRD commander (D5000). The diffraction plots undertaken using ICDD PDF-4+.

X-ray diffraction (XRD) measurement was applied to identify the austenite (fcc) in martensite matrix (bct). It is worth noting that, to simplify the discussion, ε-martensite was treated as ferrite (bcc). The XRD patterns were compared to standard diffraction patterns by software to identify phases. Each phase has characteristic X-ray peaks and corresponding to d spacing. Accurate d-spacings were calculated using Bragg's law, $\lambda = 2d\sin\theta$ (λ is the wavelength of target radiation and θ is half of the angle where the peak presents). XRD technique is considered as one of the most accurate and convenient methods to evaluate the volume fraction of austenite in steels. In this study, the volume fraction of austenite was calculated via comparison method described by Yang et al. [95] and the ASTM standard E975-03 [96]. For a randomly oriented sample, the integrated intensities of the austenite (γ) and ferrite (α) diffraction peaks are determined by:

$$I_a^{hkl} = \frac{KR_a^{hkl}V_a}{2\mu} \tag{2.1}$$

$$I_\gamma^{hkl} = \frac{KR_\gamma^{hkl}V_a}{2\mu} \tag{2.2}$$

where K is the constant related to the instrumentation geometry and radiation. R is proportional to the theoretical integrated intensity which depends on the interplanar spacing (hkl), Bragg angle θ, crystal structure and composition of the phase. V is the volume fraction of each phase and μ is the linear absorption coefficient of steels. In this study, the integrated intensities of ferrite peaks (200) and (211) and austenite peaks (200), (220) and (311) were used and measured by ICDD PDF-4+.

2.5 IDENTIFICATION OF PRECIPITATES

The crystal structure of precipitates is of vital importance for the study of precipitation-strengthened materials as the structure of precipitates, to a large extent, determines their properties and thus their roles in precipitation-strengthened materials. SAED is one of the most frequently used experimental tools to identify the crystal structure of ultrafine phases which cannot be detected by XRD or SEM. Electron diffraction pattern is unique to the crystal structure and the patterns can provide information about the size and shape of the unit cells and atomic positions in the unit cell as well. As Figure 2.3 shows, the d_{hkl} can be obtained as:

$$d_{hkl} = \frac{L\lambda}{r} \tag{2.3}$$

$L\lambda$ is known as camera constant and after measuring the nearest r_1, r_2 and r_3 we can calculate the lattice spacing and therefore get the crystal structure.

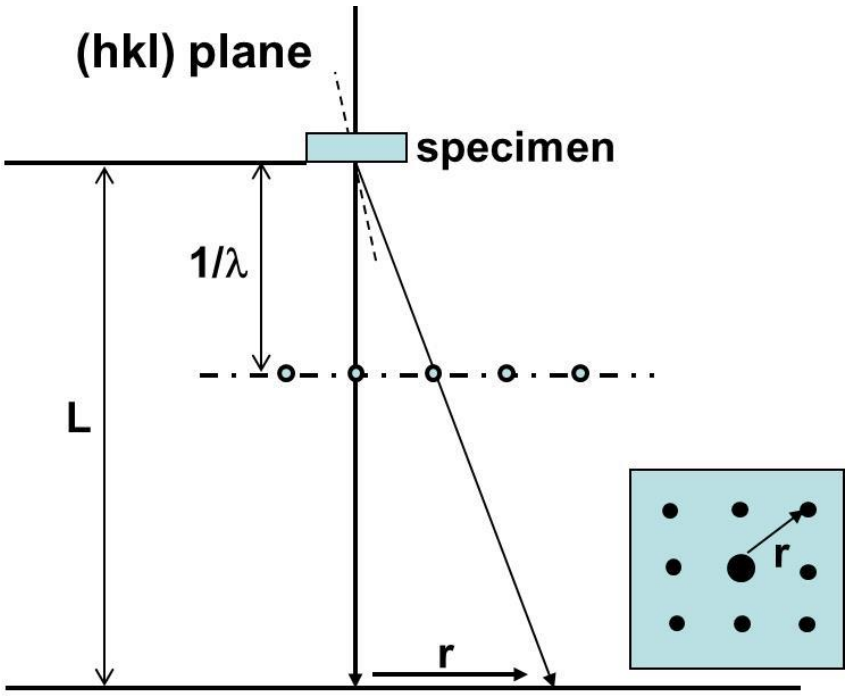

Figure 2. 3 The geometric relationship between reciprocal lattice and electron diffraction. Pattern [97].

Chapter 3: Strengthening through high-density and low lattice misfit nanoscale precipitates

3.1. INTRODUCTION

In this chapter, we have conducted an in-depth understanding of the effect of solutionization temperature on the precipitation behavior and mechanical properties of 250 grade cobalt-free maraging steel. The potential of optimizing the solutionization temperature in obtaining extremely high-density and low lattice misfit nanoscale precipitates is elucidated in the study presented here. The crystal structure of nanoscale precipitates was also analyzed to understand their contribution toward strengthening.

3.2 EXPERIMENTAL DETAIL

The specimens were first cut in the form of 2 mm×50 mm plate and solutionized at different temperatures of 780 ºC, 820 ºC, 860 ºC and 900 ºC for 1 h, and air cooled (referred as S780, S820, S860 and S900). Next, aging was carried out at 480 ºC for 3 h. Sheet tensile samples of gage length 20 mm and cross-section of 2 mm×5 mm were cut and mechanically polished using standard metallographic procedure. Tensile tests were conducted using the MTS system at a strain rate of 5×10^{-3} s^{-1}. Given that the static toughness has a direct relationship with the impact toughness and fracture toughness at room temperature [98-100], the acquired tensile stress-strain plots were used to obtain ultimate tensile strength (σb) and static toughness (UOT), which represents strength and toughness of steels, respectively [98]. The static toughness was obtained from the integrated area according to the following equation [99]:

$$U_{OT} = \int_0^{\varepsilon_t} \sigma d\varepsilon \tag{3.1}$$

where UOT is static toughness, εt is total strain after fracture, σ is real-time stress, ε is real-time strain.

To observe the microstructure, the samples were metallographically polished and etched with modified Fry's regent (50ml HCl + 25ml HNO3 + 1g CuCl2 + 150ml H2O). The microstructure of samples subjected to four different annealing temperatures was observed by optical microscopy (OM), scanning electron microscopy (SEM) combined with energy dispersive spectrometer (EDS) and high-resolution transmission electron microscopy (HRTEM). SEM studies were carried out using a Hitachi S-4800 field emission scanning electron microscope operated at 15 kV. TEM studies were carried out via FEI Tecnai G2 F20 transmission electron microscope operated at 200 kV using thin foils electropolished in a solution of 5% perchloric acid and 95% ethanol at -20 ºC. The fracture surface was observed by scanning electron microscope.

3.3 RESULTS AND DISCUSSION

3.3.1 Mechanical properties

Tensile properties of the four samples (S780, S820, S860 and S900) extracted from the engineering strain-stress plots (Fig.3.1) are listed in Table 3.1.

Table 3. 1 Tensile properties of experimental steels

Sample	σ_b, MPa	σ_s, MPa	ε_t, %	U_{Oz} MJ·m^{-3}
S780	1650	1352	9.8	83.2
S820	1858	1645	10.0	110.4
S860	1767	1420	9.4	76.3
S900	1603	1295	10.2	87.5

Note: σ_b - ultimate tensile strength, ε_t - total elongation, U_{OT} – static toughness.

On solutionizing at 780 ºC, ultimate tensile strength of 1650 MPa, yield strength of 1352 MPa and total elongation of 9.8% were obtained. The corresponding static toughness was ~83 MJ·m^{-3}. At 820 ºC, the ultimate tensile strength was increased to 1858 MPa (208 MPa higher than S780 steel) and the yield strength was increased to 1645 MPa, which was 293 MPa greater than S780 steel (increase of ~22%). Meanwhile, the total elongation was maintained at 10% and the

static toughness increased to ~110 $MJ \cdot m^{-3}$. While for S860 steel, the ultimate tensile strength and yield strength were decreased to 1767 MPa and 1420 MPa, respectively. The total elongation decreased to 9.4%, and the static toughness decreased to ~76 $MJ \cdot m^{-3}$. When the solutionizing temperature was high at 900 ^{o}C, both ultimate tensile strength and yield strength were decreased with small increase in total elongation of ~10.2%. The static toughness was 87.5 $MJ \cdot m^{-3}$. Based on the above observations, solutionization temperature had a significant effect on the mechanical properties of T-250 maraging steel. In summary, S820 steel had highest ultimate strength, yield strength and static toughness, and was characterized by best combination of strength and toughness. It can be concluded from the data of mechanical properties (Table 3.1) that the solutionization temperature of 820 ^{o}C was optimal for T-250 maraging steel.

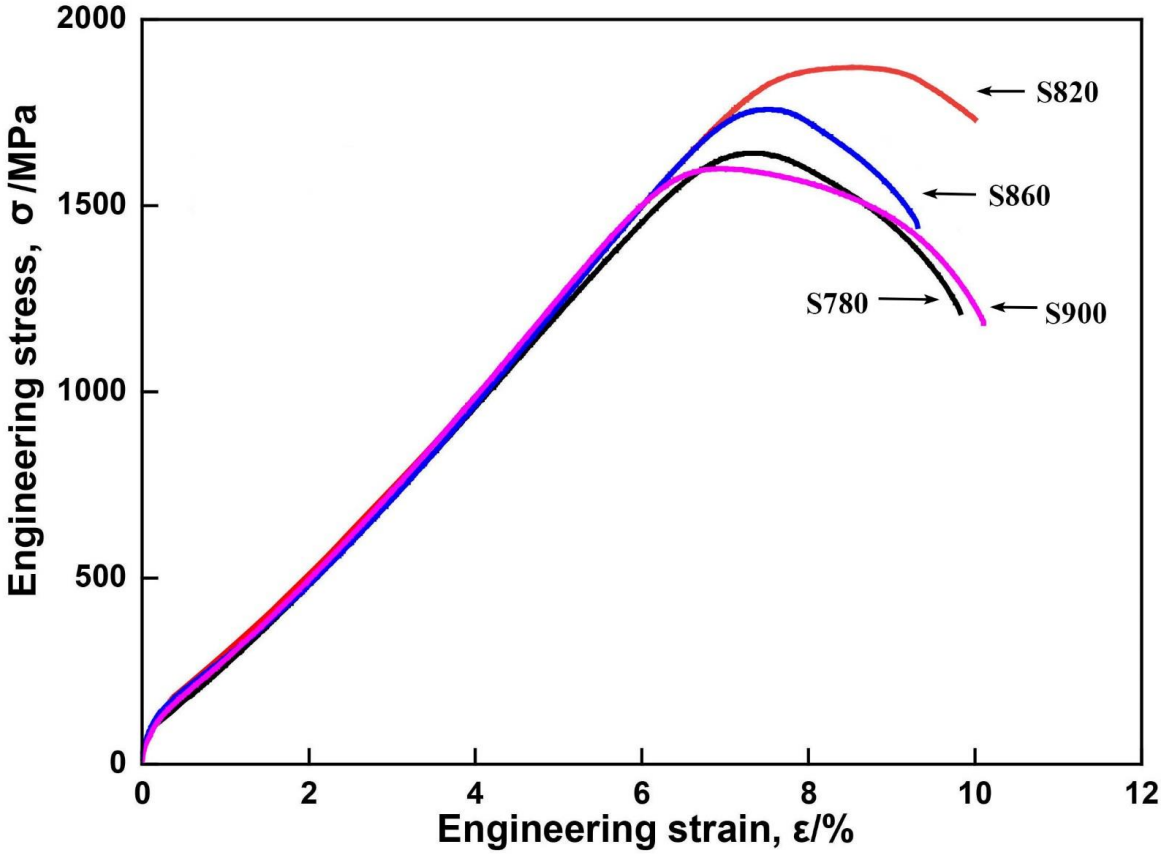

Figure 3. 1 Engineering stress-strain plots of maraging steels subjected to different solutionization temperatures.

3.2.2 Microstructure evolution

Fig.3.2 shows differences in the microstructure of four steels. All four maraging steels were characterized by lath-like martensite matrix (Fig. 3.2a1-d1). Retained and reverted austenite was absent (Fig. 3.2a2-d2) and was confirmed by X-ray diffraction and TEM studies (see below). However, the dimensions or width of martensite lath increased with increase in solutionization temperature. At 780 °C, the martensite lath within the block was needle or acicular-like (Fig. 3.2a1)

with a width of ~2 μm, as shown by arrow 1 in Fig. 3a2. At 820 ºC, the martensite lath within the block was also needle or acicular, similar to 780 ºC, but appeared to have a preferred orientation (Fig. 3.2b2). At 860 ºC, the martensite blocks had a width ~5 μm (Fig. 3.2c1), and prior austenitic grain boundaries could be delineated, as indicated by arrow 3 (Fig. 3.2c2). When solutionization was carried out at 900 ºC, the prior austenite grain size was large (~50 μm) (arrow 3 in Fig. 3.2d2), and martensite blocks were ~10 μm in size. In the etched microstructure, some etched pits presumably associated with the precipitates (arrow 2) were observed in the martensite matrix and at interface/grain boundaries (Fig. 3.2a2-d2 and inset of Fig. 3.2d2). It is known that when the interfacial energy ($\gamma_{interface}$) between the precipitate and matrix is high, it leads to corrosion at the interface surrounding the precipitates, compared to the martensite matrix [101]. The etched pits are believed to be associated with precipitates that strengthen maraging steel during the aging treatment [100,102].

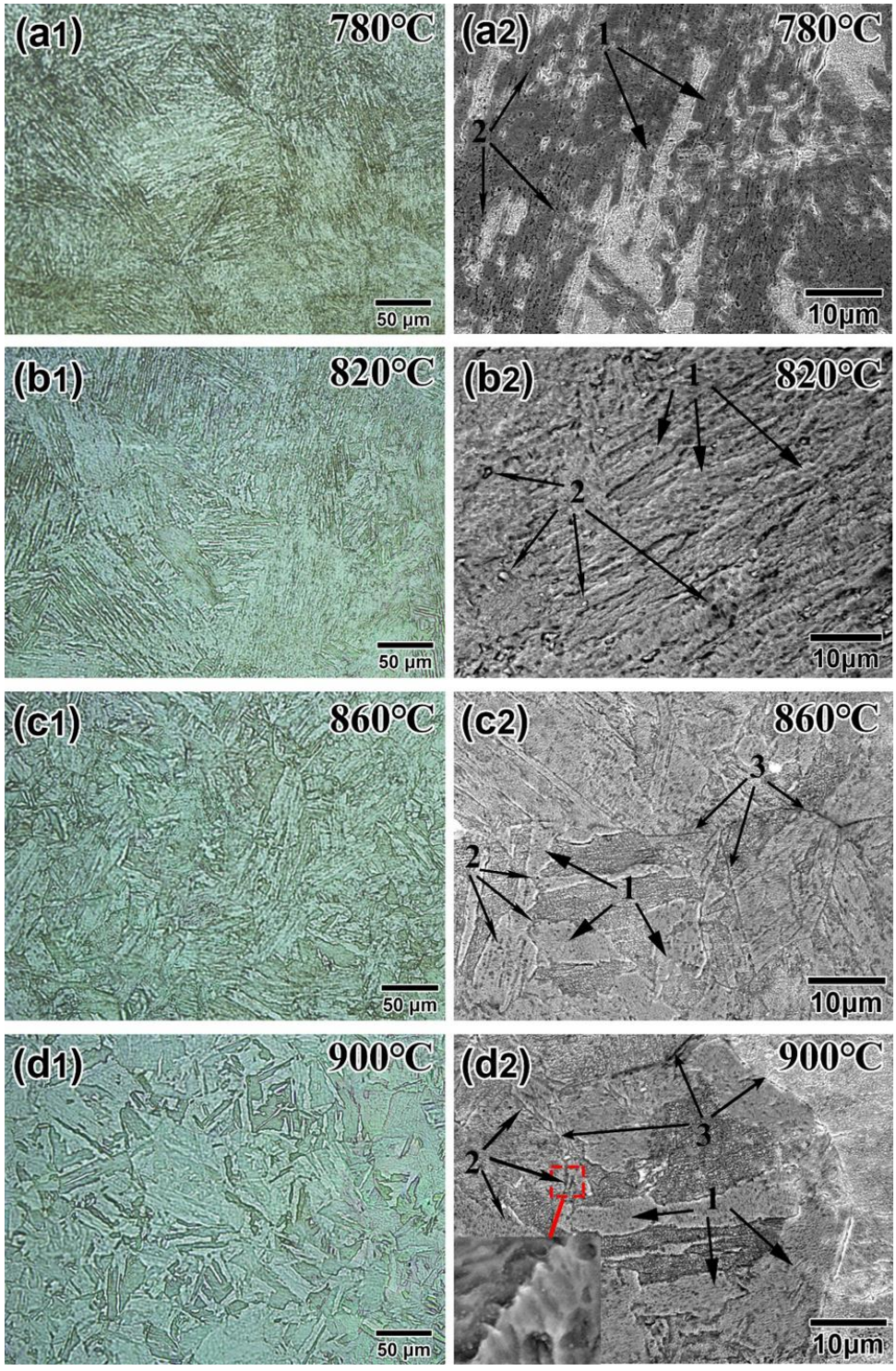

Figure 3. 2 Optical and SEM micrographs of T-250 maraging steels at different solutionization temperatures (arrow 1-martensite block, arrow 2-etched pits presumably associated with the precipitates, arrow 3-original austenitic grain boundaries).

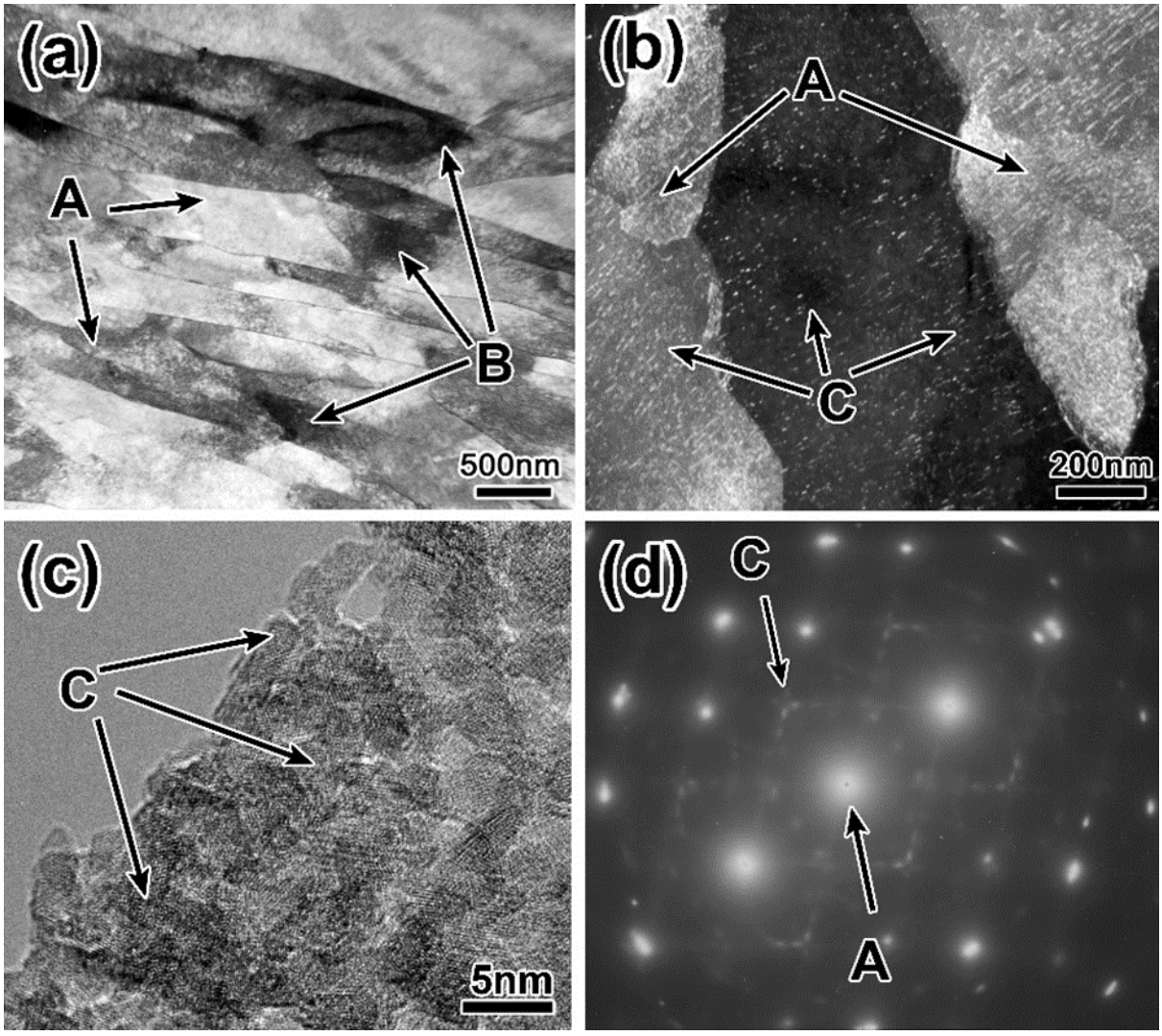

Figure 3. 3 Representative TEM micrographs of T-250 maraging steels (the solutionization temperature was 780℃) (a) martensite lath, (b) low magnification of precipitates, (c) high magnification of precipitates and (d) selected area electron diffraction pattern. (A-martensite lath, B-dislocations, C-precipitates).

To further observe the microstructure, we now describe in some detail the TEM studies of martensite lath and precipitates in Fig. 3.3. The matrix consisted of martensite lath (A) and dislocations (B). A number of nanoscale precipitates (C) of size ~2-3 nm were observed and confirmed by selected area diffraction pattern to consist of Ni_3(Ti, Mo) precipitate [103,104]. There were also nanoscale precipitates that were less spherical (Fig. 4c), and are likely to consist of Ni, Mo and Fe [105,106].

3.2.3 Effect of solutionization temperature on nanoscale precipitation

Characteristic evolution of nanoscale precipitates

The main strengthening factor for maraging steel is precipitates [104,107,108]. Thus, the characteristics of nanoscale precipitates at different solutionization temperatures are important in governing mechanical properties, whose evolution is illustrated in Fig. 3.4. At 780 ^{o}C, the size of precipitates was small and their density was low (Fig. 3.4a). The density of nanoscale precipitates at 820 ^{o}C was higher and their distribution was also uniform (Fig. 3.4b). With further increase in the solutionization temperature, the precipitates coarsened and their density was decreased. When the temperature was 900 ^{o}C, the size of precipitates was increased to ~20 nm, and the density was the lowest (Fig. 3.4d).

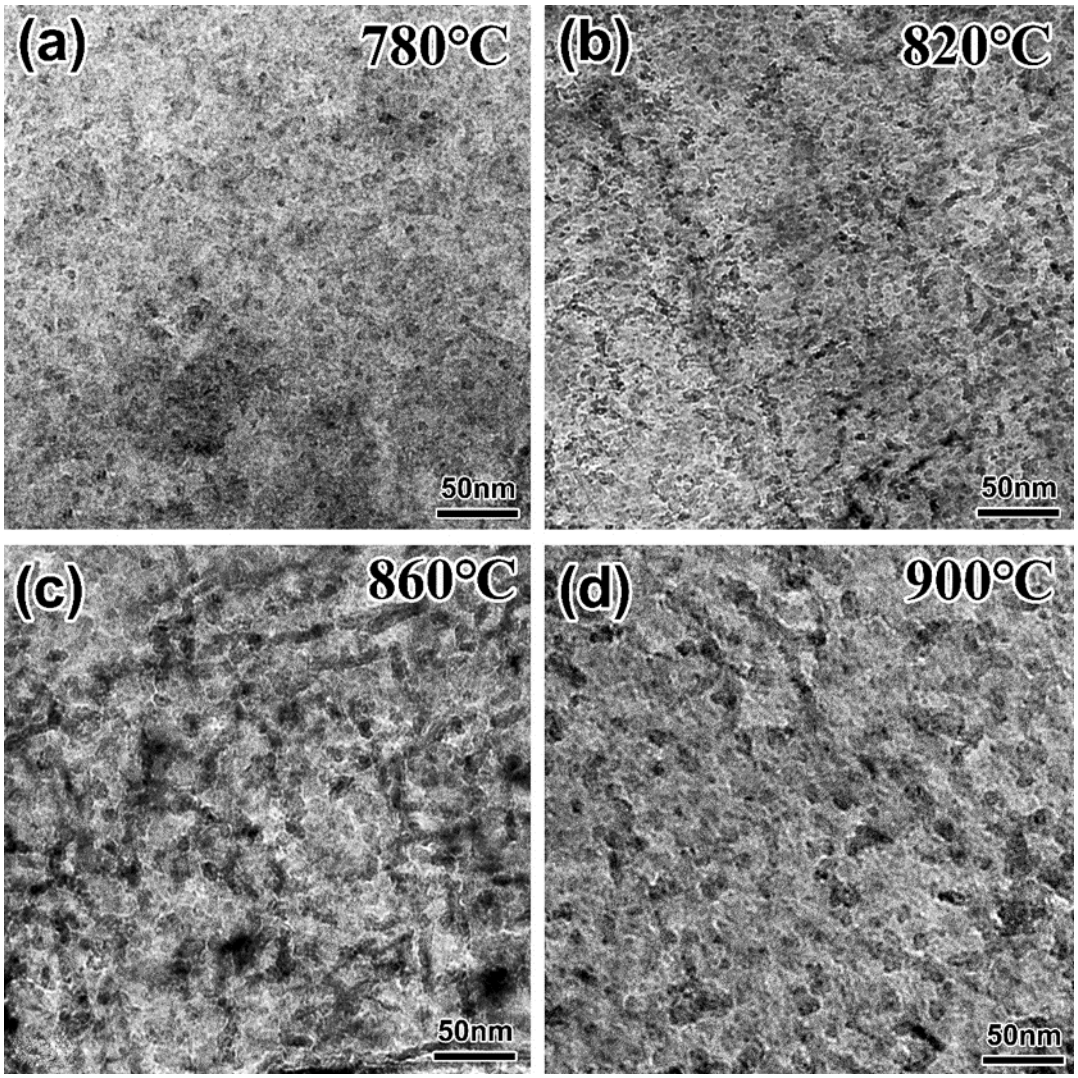

Figure 3. 4 Representative TEM micrographs illustrating the characteristics of nanoprecipitates at different solutionization temperatures.

Using a number of TEM micrographs of the type presented in Fig. 3.4, the characteristics of nanoscale precipitate were statistically analyzed using MATLAB software and Nano-measurer software. At least 30 micrographs of each steel and more than 2000 nanoscale precipitates were assessed for measurements. Assuming nanoscale precipitates to be spherical, the total volume fraction of nanoscale precipitates (fv) was estimated by:

$$f_v = \sum \frac{V_i}{V_{total}} \tag{3.1}$$

and the average nanoscale precipitate size ($\bar{d}_{ppt}$), nanoscale precipitate spacing (λ_{ppt}) and nanoscale precipitate density (ρ_{ppt}, unit: m^{-3}) were evaluated by equations 3.2-3.4 respectively:

$$\bar{d}_{ppt} = 2R = \sum (\frac{V_i}{V_{total}} \cdot d_i) \tag{3.2}$$

$$\lambda_{ppt} = \sqrt{\frac{2\pi}{3 f_v}} \frac{\bar{d}_{ppt}}{2} \tag{3.3}$$

$$\rho_{ppt} = \frac{6 f_v}{\pi \bar{d}_{ppt}^3} \tag{3.4}$$

where $\frac{V_i}{V_{total}}$ is the volume fraction of nanoscale precipitates having diameter, d_i (unit: nm). Furthermore, the average width of martensite lath (W_m) was also measured by MATLAB software from more than 20 TEM micrographs. Based on equations (3.2) -(3.4), the characteristic evolution of nanoscale precipitates (size, volume fraction, density and spacing between nanoscale precipitates) and the width of martensite lath as a function of solutionization temperature are presented in Fig. 3.5. It was observed that the solutionization temperature had an effect on the characteristics of nanoscale precipitates and martensite lath. The width of martensite lath (W_m) was increased from ~0.2 μm to ~1 μm with increased solutionization temperature. Meanwhile, the diameter ($\bar{d}_{ppt}$) of nanoscale precipitates increased from ~2-3 nm to ~22 nm with solutionization temperature. The total volume fraction of nanoscale precipitates (f_v) first increased with increase of solutionization temperature, and then decreased when the solutionization temperature was

greater than 860 ºC. While the spacing between the nanoscale precipitates (λ_{ppt}) indicated a trend opposite to that of size, such that the lowest value of λ_{ppt} was observed at 820 ºC. At this temperature the nanoscale precipitate density was highest (2.3×10^{24} m^{-3}), when the steel exhibited the best combination of strength and toughness (Table 3.1).

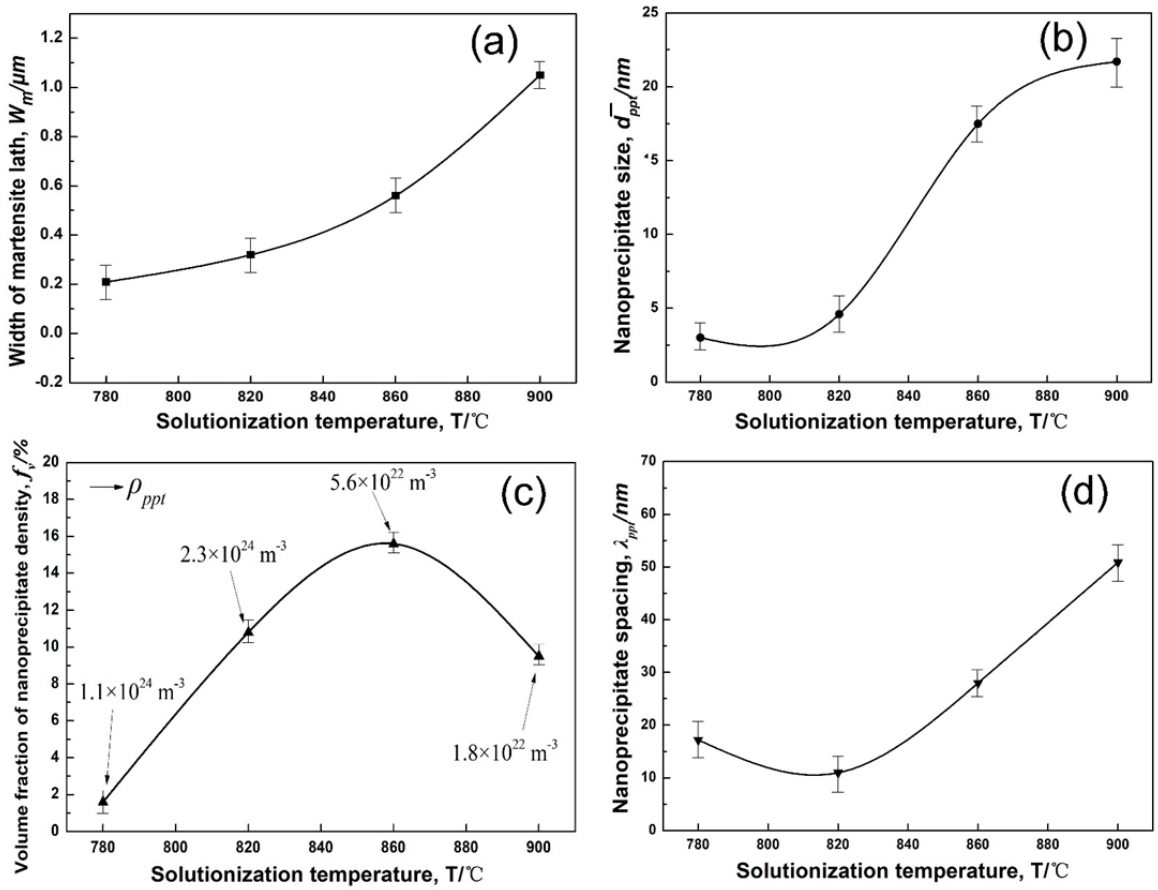

Figure 3.5 Characteristic evolution of martensite lath and nanoprecipitates in T-250 maraging steel as a function of solutionization temperature.

Nanoscale precipitates and relationship with matrix

Figs. 3.6 and 3.7 are the representative high resolution TEM micrographs of nanoscale precipitates in two different regions of maraging steel. The nature of nanoscale precipitates was identical in all the four steels. There were two kinds of nanoscale precipitates in T-250 maraging

steel, both of which had superlattice diffraction pattern. The differences in the high resolution image of nanoscale precipitates and matrix were clearly distinguished by the IFFT image (Fig. 3.6c). The points in the broken box of the two-dimensional lattice image of nanoscale precipitate indicated an alternating bright and dark superlattice pattern (Fig. 3.6a), while the points in the solid box of the two-dimensional lattice image of the matrix (Fig. 3.6a) were of similar brightness, identified by M. It is the difference in the real space between the nanoscale precipitates and the matrix, while the superlattice diffraction spots is the difference in the reciprocal space between the nanoscale precipitate and matrix. In combination with the FFT image (Fig. 3.6b) and selected area electron diffraction pattern (Fig. 3.6d) of the high resolution image, the nanoscale precipitate was identified as η-Ni3(Ti,Mo) by indexing the diffraction pattern in Fig. 7e. This was further confirmed from the atomic ratio of Ni and Ti, Mo by energy dispersive X-ray spectroscopy (Fig. 7f), consistent with the results of Fig. 4. According to the diffraction pattern, the η-Ni3(Ti,Mo) had an hcp structure [14,15]. The atomic arrangement of Ni3(Ti,Mo) is delineated by the box with broken lines in Fig. 3.6a. The crystal orientation relationship between Ni3(Ti,Mo) nanoscale precipitate and the matrix was $(01\bar{1}2)_\eta \parallel (110)_\alpha$, $[\bar{2}110]_\eta \parallel [001]_\alpha$. Using identical approach, another type of nanoscale precipitate was identified as B2-Ni(Mo,Fe) (Fig. 8a-8f). Based on the diffraction pattern, B2-Ni(Mo,Fe) had bcc structure. The atomic arrangement of Ni(Mo,Fe) is shown in the box with broken lines in Fig. 3.7a. The crystal orientation relationship between Ni(Mo,Fe) nanoscale precipitate and the matrix was $(110)_{B2} // (110)_\alpha$, $[001]_{B2} // [001]_\alpha$. Based on high resolution images, the a-axial lattice constant of η-Ni3(Ti,Mo), B2-Ni(Mo,Fe) and the matrix was statistically analyzed. They were aη=0.2785 nm, aB2=0.2886 nm and am=0.2877 nm, respectively, which are similar to the lattice parameter of α-Fe matrix in maraging steel, am=0.288 nm [109,110]. Using identical approach, all four steels were characterized by high resolution TEM

and the lattice parameters are listed in Table 3.2. At low temperature of 780 ºC, the lattice constant of Ni_3(Ti,Mo) was smaller than the matrix, while the lattice constant of Ni(Mo,Fe) was slightly larger than the matrix. The small change in the lattice constant of η-Ni_3(Ti,Mo) and B2-Ni(Mo,Fe) is related to distribution of Ni atoms with change in the solutionization temperature. As the solutionization temperature was increased, it was envisaged that a number of Ni atoms were associated with Ni_3(Ti,Mo) and Ni(Mo,Fe) nanoscale precipitates, and the decrease in the fraction of Ni atoms in the martensite matrix was apparent. This phenomenon led to increase in the lattice constant of η-Ni_3(Ti,Mo) and B2-Ni(Mo,Fe) and the lattice constant of the matrix was decreased (Table 3.2). However, when the temperature was greater than 860 ºC, e.g., S900 steel, there was an increase in the lattice constant of matrix, because high solutionization temperature led to dissolution of some nanoscale precipitates back into the matrix (Fig. 3.5), with consequent increase in the fraction of Ni atoms in the matrix. Irrespective of the above, from the lattice misfit (Table 3.2), we envisage that both types of nanoscale precipitates in the four steels had low lattice misfit with the matrix ($<5\%$), and for S820 steel, the lattice misfit was less than 1% for both η-Ni_3(Ti,Mo) and B2-Ni(Mo,Fe) nanoscale precipitates, and were coherent with the matrix. Correspondingly, S820 steel had the highest strength and toughness (Table 3.1). This underscores that low misfit between nanoscale precipitates and matrix in T-250 maraging steel had a significant influence in governing the mechanical properties of maraging steel.

Table 3. 2 Lattice parameters and misfit between nanoscale precipitates and matrix (in nanometers).

Sample	a_m	a_η	δ_η	a_{B2}	δ_{B2}
S780	0.2877	0.2785	3.2%	0.2886	0.3%
S820	0.2864	0.2847	0.6%	0.2890	0.9%
S860	0.2848	0.2895	1.7%	0.2912	2.2%
S900	0.2869	0.2978	3.8%	0.2950	2.8%

Note: a_m, a_η and a_{B2} are lattice constant of matrix, η-Ni_3(Ti,Mo) and B2-Ni(Mo,Fe), respectively, δ_η-the lattice misfit between η-Ni_3(Ti,Mo) and the matrix, δ_{B2}- the lattice misfit between B2-Ni(Mo,Fe) and the matrix.

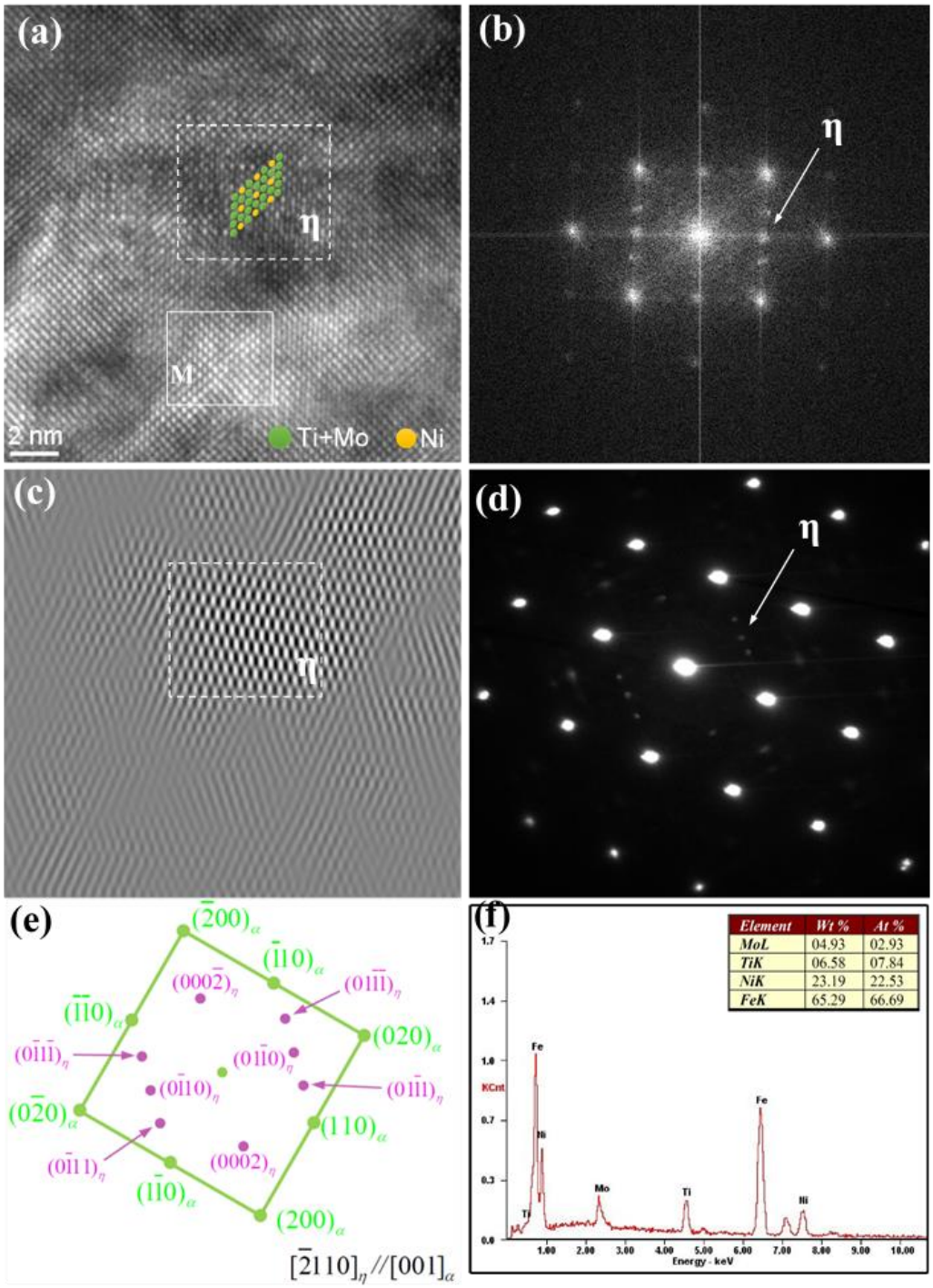

Figure 3.6 (a) Representative high resolution image of one area in maraging steel along $[001]_\alpha$ direction (the solutionization temperature was 780℃), (b) FFT image of (a), (c) IFFT image of (a), (d) selected area electron diffraction pattern of (a), (e) indexing of diffraction pattern of (b) and (d), (f) EDS of η-Ni_3(Ti,Mo) nanoprecipitate in (a).

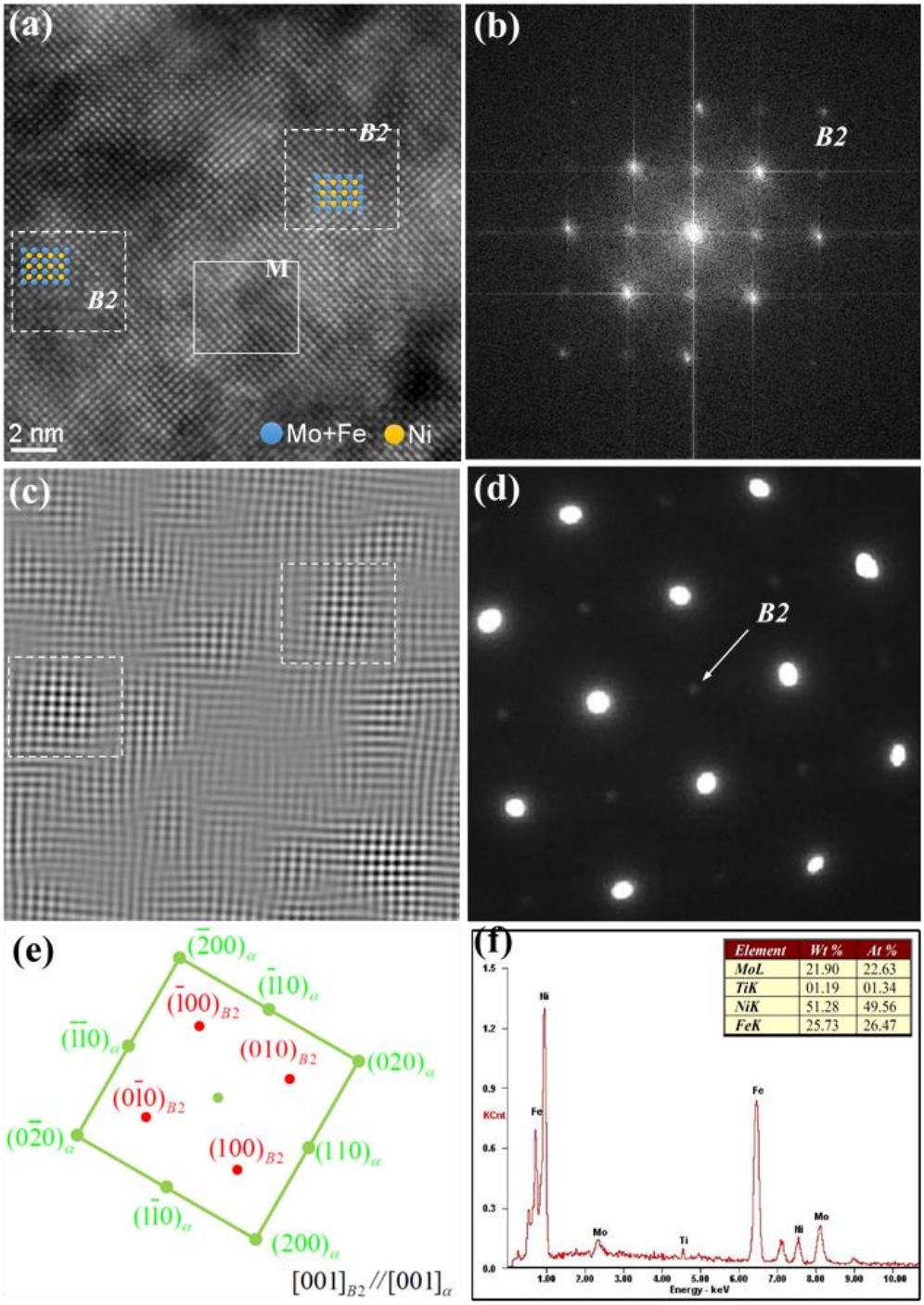

Figure 3.7 (a) Representative high resolution image of another area in maraging steel along [001]α direction (the solutionization temperature is 780°C), (b) FFT image of (a), (c) IFFT image of (a), (d) selected area electron diffraction pattern of (a), (e) indexing of diffraction pattern of (b) and (d), (f) EDS of B2-Ni(Mo,Fe) nanoprecipitate in (a).

3.2.4 Strengthening response of nanoscale precipitates and mechanical properties

The increase in yield strength by precipitation strengthening is given by Orowan-Ashby equation [111-113]:

$$\Delta R_p = (0.538Gb\sqrt{f_v} / 2R)\cdot \ln(R/b)_{\text{-ModeI}} = cGb/\lambda_{\text{-ModeII}} \quad (3.5)$$

where ΔR_p is the yield strength increase associated with precipitates, G is the shear modulus, b is the Burgers vector, f_v is the volume of the precipitate, R is the radius of the precipitate, c is the correction coefficient and λ is the precipitate spacing. In T-250 Co-free maraging steel, the nanoscale precipitates are the primary contributors to strength. The two mechanisms through which the dislocations can move across the precipitates are cutting and by-passing based on interparticle spacing. This is schematically illustrated in Fig. 3.8. If $R/b < 15$, the dislocation moves by cutting (shearing) the precipitate (Mode I), where f_v and R are the dominant factors influencing the strength. If $R/b \geq 15$, the dislocation moves via by-passing the precipitate forming a dislocation loop around the precipitate (Mode II), where λ is the dominant factor influencing the strength. In our study, the Burgers vector b for the martensite matrix, i.e., the unit slip distance in easy atomic slip direction, is 0.248 nm [38] and the shear modulus G=72 GPa [41,42]. Based on the size of nanoscale precipitates ($\bar{d}_{ppt}=2R$) presented in Fig. 3.5, the value of R/b of four steels is listed in Table 3.3. For S780 and S820 steels, the R/b is below 15, which activates Mode I. When the solutionization temperature is greater than 860 °C, the R/b of S860 and S900 steels is greater than 15, which activates Mode II. According to equation (3.5) and Fig. 3.5， the yield strength increment by precipitate (ΔR_p) was calculated, and the second yield strength increment (ΔR_m) involved the martensite matrix. Their contributions are listed in Table 3.3. It shows that the contribution of nanoscale precipitates to yield strength is greater than the martensite matrix, which

suggested that the nanoscale precipitates played a dominant role in strengthening T-250 maraging steel. At solutionization temperature of 780 ºC and 820 ºC, a greater number of Ni atoms are involved in precipitates, which increased the precipitation strengthening effect and decreased solid solution strengthening effect. Thus, the yield strength increment by nanoscale precipitates was increased, while that of the martensite matrix was decreased. However, at relatively higher solutionization temperature of 860 ºC and 900 ºC, Ni atoms from the precipitates dissolved back into the martensite matrix such that the precipitation strengthening effect was reduced. In summary, S820 steel had the highest density of nanoscale precipitates and lowest lattice misfit between the two types of nanoscale precipitates and matrix, which led to maximum strength in S820 steel, with insignificant loss in ductility.

Table 3.3 Tensile properties of experimental steels.

Sample	*R/b*	ΔR_p, MPa	ΔR_m, MPa	$\Delta R_{modulus}$, MPa	$\Delta R_{ordering}$, MPa
S780	7.40	664	668	205	427
S820	11.3	1259	386	402	906
S860	43.0	1077	343	—	—
S900	53.3	893	402	—	—

Note: ΔR_p-the yield strength increment by precipitate, ΔR_m-the yield strength increment by martensite matrix, $\Delta R_{modulus}$-the yield strength increment by ordering hardening, $\Delta R_{ordering}$-the yield strength increment by modulus hardening.

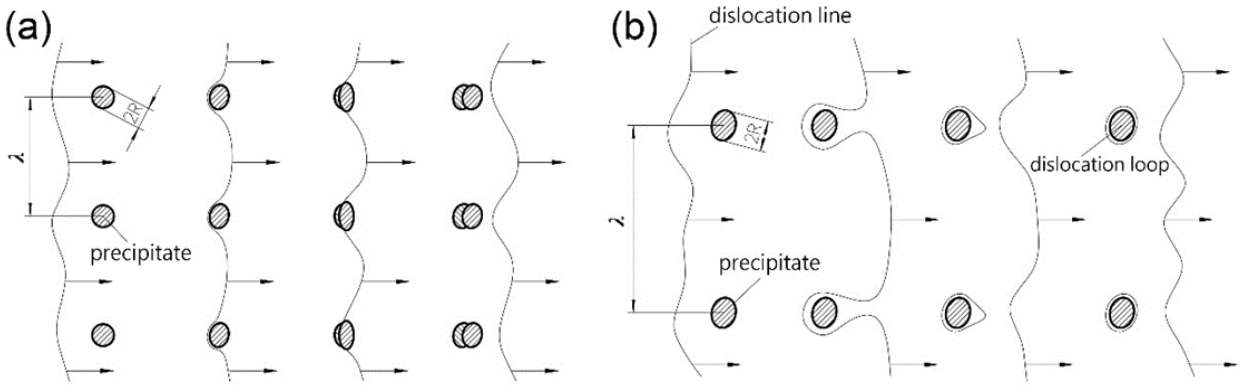

Figure 3.8 Schematic illustration of movement of dislocations (a) Mode I-dislocation moves by cutting precipitate and (b) mode II-dislocation moves via by-passing precipitates.

The characteristics of nanoscale precipitates and their lattice misfit with the matrix significantly influence the inherent strengthening mechanism. In the case of S780 and S820 steels, the coherent η-Ni_3(Ti,Mo) and B2-Ni(Mo,Fe) nanoscale precipitates strengthened the matrix via Mode I because of their nanoscale dimensions (~2-3 nm) and very high density (greater than 10^{24} m^{-3}). In this system, with low coherency strain (low lattice misfit), the elastic interaction between the nanoscale precipitates and dislocations is less and strengthening from elastic coherency strain is negligible. Modulus and ordering hardening contributed to the precipitation strengthening mechanism. The modulus hardening contribution to the yield strength increment can be estimated by Knowles-Kelly equation [114]:

$$\Delta R_{\mathrm{mod}ulus} = \frac{M\Delta G}{4\pi^2}\left(\frac{3\Delta G r f_v}{Gb}\right)^{1/2}\left[0.8-0.143\ln\left(\frac{r}{b}\right)\right]^{2/3} \tag{3.6}$$

where $M\approx3$ is Taylor factor, b, $r=\bar{d}_{ppt}/2$, f_v and G are identical to equation (6). ΔG is the difference in the shear modulus between the precipitates and the matrix. The modulus of B2

phase is reported to be ~88 GPa and is not strongly composition-dependent [115]. The ordering hardening contribution to the yield strength increment is estimated by [38]:

$$\Delta R_{ordering} = \frac{M\gamma_{apb}^{3/2}}{b}\left(\frac{4r_s f_v}{\pi T_1}\right)^{1/2} \tag{3.7}$$

where $r_s=(2/3)^{1/2}r$ is the average radius of the sheared precipitates in the gliding plane, γ_{apb}=0.48 J·m^{-2} is the average value of the antiphase boundary energy for η-Ni_3(Ti,Mo) and B2-Ni(Mo,Fe), which is similar to NiAl [116-119] and T_1 is the dislocation line tension, which is approximated as ~$Gb^2/2$. The calculated results are listed in Table 3.3. The contribution of modulus strengthening and ordering strengthening to the total yield strength was calculated to be 205 MPa and 427 MPa for S780 steel, and 402 MPa and 906 MPa for S820 steel, respectively. Adding these two factors, the total strengthening increment is 632 MPa for S780 steel and 1308 MPa for S820 steel, consistent with equation (3.5), i.e., 664 MPa for S780 steel and 1259 MPa for S820 steel, respectively (Table 3.3). This result indicated that ordering strengthening had greater influence on strength, which is related to the high density of nanoscale precipitates and their low lattice misfit with the matrix.

As regards the toughening mechanism, the nanoscale precipitates can make a significant difference. Fig. 3.9 shows working hardening rate curves for the four steels as a function of true strain. The data extracted from Fig. 3.9 is summarized in Table 3.4. It is clear that the four steels were characterized by three stages of working hardening rate (WHR). In the first stage (S1), WHR decreased with increased strain, and then increased gradually in the second stage (S2), and finally decreased to zero in the third stage (S3). The increase in stage S2 is attributed to the contribution of nanoscale precipitates on uniform deformation, while S1 and S3 are associated with the deformation of martensite matrix and nanoscale precipitates. The starting strain (ε_s) and final strain

(ε_f) of working hardening refers to the beginning and end of uniform deformation, respectively. The commencement of work hardening for S820 steel occurred at a later stage at ε_s=0.032, because ordering and modulus strengthening by nanoscale precipitates hindered the movement of dislocations and provided a larger elastic regime prior to the yield point compared to the other three steels. The end of work hardening of S820 steel also occurred at a later stage at ε_f=0.088, and the total true strain during the work hardening period $\Delta S2$=0.056, was the largest. This implied that the high density of nanoscale precipitates had an important role in uniform deformation because of near homogeneous distribution of nanoscale precipitates in the matrix. Additionally, the WHR of S820 steel in the second stage increased more rapidly than other three steels. This is attributed to the lowest lattice misfit between the nanoscale precipitates and matrix in S820 steel. It was difficult for the dislocation to cut or by-pass the nanoscale precipitates that are highly coherent with the matrix. Thus, the ultrahigh strength and high toughness of maraging steel (S820) was obtained via high density and extremely low lattice misfit (＜1%) nanoscale precipitates via optimized solutionization temperature.

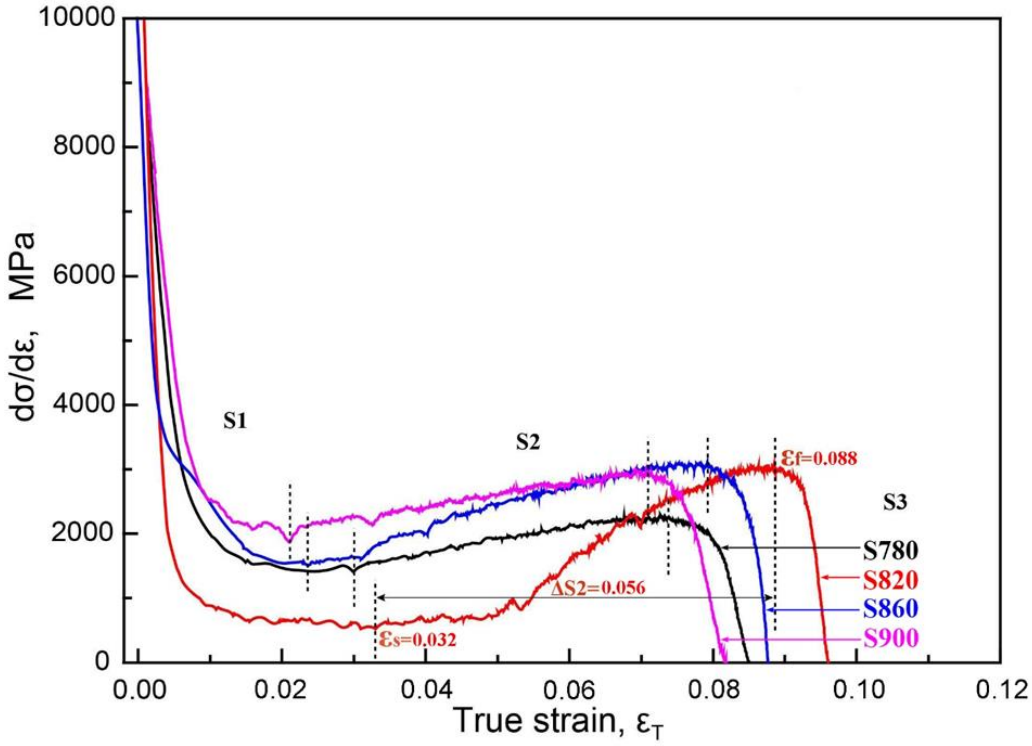

Figure 3.9 The curves of working hardening rate *vs* the true strain of four steels (S1 stage 1, S2-stage 2, S3-stage 3, ε_s – the starting strain of work hardening, ε_f- the final strain of work hardening, *ΔS2* – the total true strain during the work hardening period).

Table 3.4 Summary of work hardening rate of experimental steels.

Sample	εs	εf	ΔS2
S780	0.029	0.073	0.044
S820	0.032	0.088	0.056
S860	0.024	0.078	0.054
S900	0.021	0.070	0.049

Note: εs – the starting strain of work hardening, εf - the final strain of work hardening, ΔS2 – the total true strain during the work hardening period.

It may be briefly appropriate to describe the tensile fracture. Fracture is generally representative of the deformation processes such that it may retain the signature of the deformation processes. The fracture may also reflect the size and distribution of precipitates. The fracture surface of four steels, as imaged via SEM, are presented in Fig. 3.10. It can be seen that all the four steels exhibited ductile fracture mode, but a careful examination suggests that there was significant difference in the nature, size and distribution of dimples. When the solutionization temperature increased from was 780 ºC to 820 ºC, the size of dimples in S820 steel was small (~0.5-1.5 μm) and their distribution over the entire fracture was highly uniform compared to S780 steel (Fig.3.10a). In S860 steel (Fig. 3.10c), the size of dimples was inhomogeneous (~0.5-5 μm) and their distribution was non-uniform. In S900 steel, while the dimple was relatively uniform (~3-5 μm), but they were shallow. Furthermore, in S780 and S820 steels, very few microcracks (indicated by red arrow) were observed, while in S860 and S900 steels, a greater number of microcracks were observed. The highest density (2.3×10^{24} m^{-3}) and uniform size of nanoscale precipitates in S820 steel resulted in small-sized dimples compared to the other three steels. In

addition, the nanoscale precipitates in S820 steel had the lowest lattice misfit with the matrix. When the lattice misfit is low, it requires higher stress and more strain for the nanoscale precipitates to separate from the matrix. Furthermore, the low elastic interaction between the nanoscale precipitates and the dislocations is reduced. This decreases the possibility of crack initiation at the precipitate-matrix interface because of very low misfit and appreciably reduced accommodation of strain. It is expected that the microcracks (red arrows) present on the fracture surface initiated at the precipitate-matrix interface or because of inconsistent deformation between martensite lath with different orientations. There was increased tendency for microcracks with increase in lattice misfit (i.e. increase in solutionization temperature).

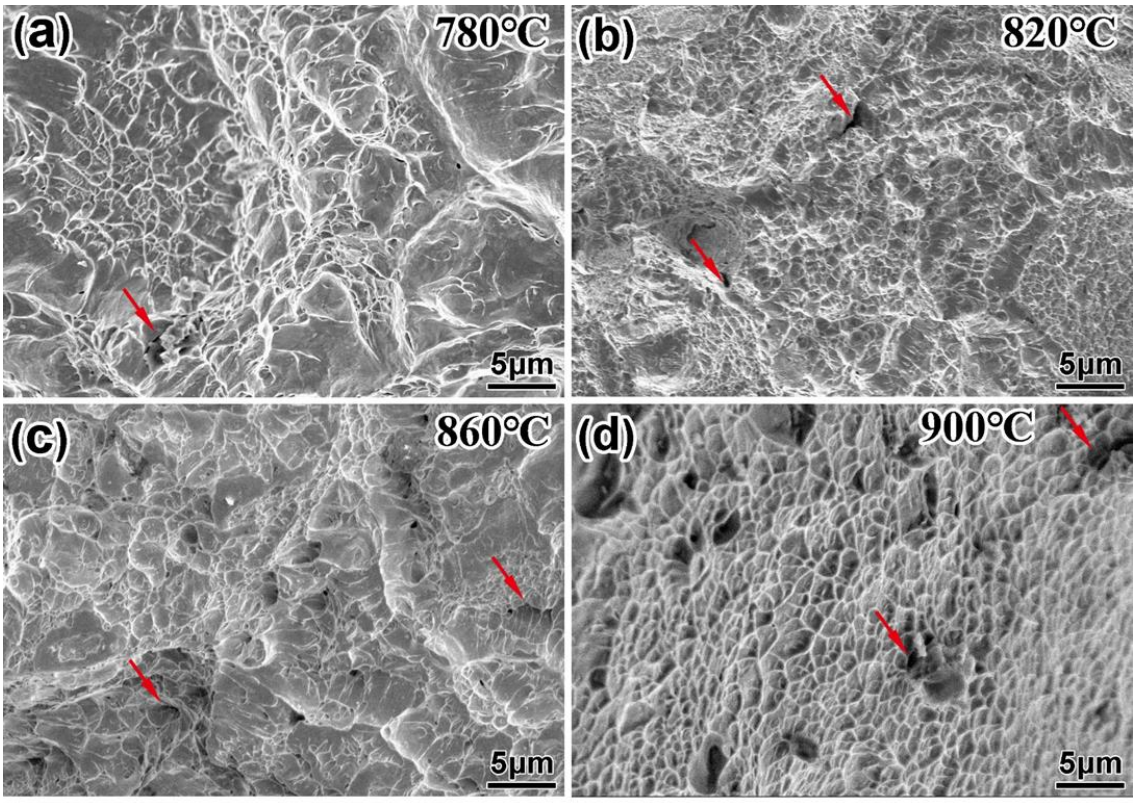

Figure 3.10 Representative SEM micrographs of fracture surface of four steels at different solutionization temperatures. (red arrow- microcrack).

3.4 CONCLUSIONS

An excellent combination of strength and toughness was obtained in the optimized 820 ºC solution heat treated steel. The ultimate strength and static toughness were 1858 MPa and ~110 MJ·m-3. Both these properties were superior than the other three steels solution heat treated at 780 ºC, 860 ºC and 900 ºC.

The solutionization temperature controlled the characteristic evolution of nanoscale precipitates. The nanoscale precipitates were identified as η-Ni3(Ti,Mo) with a hcp crystal structure and B2-Ni(Mo,Fe) with a bcc crystal structure. The η-Ni3(Ti,Mo) nanoscale precipitate had a slightly smaller lattice constant than the matrix, while the B2-Ni(Mo,Fe) nanoscale precipitate had a larger lattice constant than the matrix. The optimized solutionization temperature of 820 ºC increased the density of nanoscale precipitates (~2-3 nm) to 2.3×1024 m-3 with minimal lattice misfit of less than 1%.

The precipitation strengthening was the dominant strengthening mechanism in T-250 maraging steels. The strengthening effect by nanoscale precipitates was first increased and then decreased with the increase of solutionization temperature from 780 ºC to 900 ºC. Ordering and modulus strengthening contributed to high strength, while ordering strengthening played a more effective role than modulus strengthening, with the maximum contribution of 906 MPa in S820 steel.

The high density and low lattice misfit of nanoscale precipitates had a significant influence on the toughness and ductility of maraging steel. In S820 steel with the optimized solutionization temperature, the highest density of nanoscale precipitates and lowest lattice misfit led to work hardening at a later stage (high strain) and a longer work hardening period, which contributed to increase in the elastic deformation and uniform deformation regimes.

The ultra-fine size and low lattice misfit of nanoscale precipitates in S820 steel led to fracture with small and uniform-sized dimples.

3.5 SUMMARY

In this chapter we have fundamentally elucidated here the concept of low lattice misfit of nanoscale precipitates with the matrix and the high density of nanoscale precipitates in the context of cobalt-free maraging steel to obtain an ultra-strong T-250 maraging steel. The ultra-strong maraging steel was characterized by high-density and minimal lattice misfit nanoscale precipitates obtained by optimizing the solutionization temperature followed by aging. HRTEM was used to understand the nanoscale crystal structure and precipitation behavior of nanoscale precipitates. The tensile fracture was characterized to obtain an insight on the significant role of high-density and low lattice misfit nanoscale precipitates on mechanical properties.

The concept of low lattice misfit and high-density of nanoscale precipitates obtained through solution treatment was adopted to obtain ultrahigh strength maraging steel without compromising elongation. An "ultrahigh strength-high toughness" combination was successfully obtained in 19Ni3Mo1.5Ti maraging steel with ultimate strength of ~1858 MPa and static toughness of ~110 $MJ \cdot m^{-3}$. Maraging steel had extremely high density ($2.3 \times 1024\ m^{-3}$) of nanoscale precipitates with minimum lattice misfit of less than 1% at the solutionization temperature of 820 ^{o}C. Two kinds of nanoscale precipitates, namely, η-Ni3(Ti,Mo) and B2-Ni(Mo,Fe) contributed to ultrahigh strength. The size of nanoscale precipitates governed the movement of dislocations, cutting versus by-passing. Theoretical estimate of ordering and modulus contribution to strengthening suggested that ordering had a dominant influence on strength. The toughness was closely related to the characteristic evolution of nanoscale precipitates such that the high density of nanoscale precipitates contributed to increase of elastic deformation and low lattice misfit

contributed to increase of uniform deformation. The nanoscale size and low lattice misfit of precipitates were the underlying reasons for the high-performance of maraging steel. Moreover, the combination of high-density of nanoscale precipitates and low lattice misfit is envisaged to facilitate the futuristic design and development of next generation of structural alloys.

Chapter 4 Aging temperature on Microstructural evolution and strengthening behavior

4.1 INTRODUCTION

In the last chapter, we conducted an in-depth understanding of the effect of solution temperature on the mechanical behavior of 250 grade cobalt-free maraging steel and obtained an optimal solution temperature at which high-density and low lattice misfit nanoscale precipitates were obtained. In sequel to the previous chapter, we present here a systematic study of aging temperature on the mechanical properties of this cobalt-free maraging steel. The microstructural evolution and hardening behavior were critically analyzed using a combination of electron back-scattered diffraction (EBSD), scanning electron microscopy (SEM) and transmission electron microscopy (TEM) to study phase precipitation and phenomena in this maraging steel.

4.2 EXPERIMENTAL DETAIL

The samples were solutionized at optimal temperature of 820 ℃ based on our previous study for 1 h followed by AC. The aging treatment was carried out at different temperatures of 460 ℃, 480 ℃, 520 ℃ and 560 ℃ for 3 h followed by AC (referred as A460, A480, A520 and A560). Tensile tests were conducted using an MTS system at a strain rate of 5×10^{-3} s^{-1} to determine mechanical properties of steels. The dimensions of tensile samples and method of obtaining ultimate strength (σ_b), elongation (ε) and static toughness (U_{OT}) are described in previous chapter.

The samples for microstructural analysis were metallographically polished and etched for SEM observation via a Hitachi S-4800 field emission scanning electron microscope operated at 15 kV, and electro-polished with a solution consisting of 90% glacial acetic acid and 10% perchloric acid at a voltage of 12 V for EBSD observations. Thin foils for TEM observation via FEI Tecnai G2 F20 transmission electron microscope operated at 200 kV were made by mechanical thinning

to ~50 μm, followed by twin-jet polishing in a solution of 5% HClO4 + 95% CH3COOH at a potential of 40 V at 253 K.

4.3 RESULTS AND DISCUSSION

4.3.1 Mechanical properties

The mechanical properties of maraging steels corresponding to four different aging temperatures obtained via tensile tests are listed in Table 4.1. It is clear that the steel aged at 460 ℃ had inferior tensile properties with ultimate tensile strength of 1409 MPa, yield strength of 1239 MPa and static toughness of 75.8 $MJ \cdot m^{-3}$ (total elongation: 9.9%). When aging temperature was increased, the tensile strength and static toughness were both increased, as well as total elongation. At aging temperature of 480 ℃, the ultimate strength was 1850 MPa, an increase of 441 MPa and yield strength was 1642 MPa, an increase of 403 MPa, whist the static toughness was significantly increased to 112 $MJ \cdot m^{-3}$ with total elongation of 10.7%. As the aging temperature was increased to 520 ℃, the ultimate tensile strength of steel was highest at 1892 MPa (~500 MPa greater than A460) with highest yield strength of 1730 MPa (increase of ~40%). Meanwhile, the static toughness was increased to the peak value of 125.4 $MJ \cdot m^{-3}$ and total elongation was 11.5% (Table 1). At higher aging temperature of 560 ℃, the ultimate strength decreased to 1708 MPa, yield strength was 1615 MPa, with total elongation of 11.8% and static toughness of 110.5 $MJ \cdot m^{-3}$.

From the mechanical properties of steels aged at different temperatures (Table 4.1), it is clear that aging temperature of cobalt-free 19Ni3Mo1.5Ti maraging steel had a significant effect. The steel aged at 520 ℃ exhibited the best combination of strength and toughness, which resulted from precipitation behavior during aging. In the under-aged (temperature less than 520 ℃) or over-aged condition (temperature greater than 520 ℃), the nature of martensite, precipitates and reverted austenite that are expected to be present at higher aging temperature in the maraging steel did not

effectively impact mechanical properties (see below). The microstructural evolution and precipitation behavior are discussed in detail in following sections.

Table 4. 1 Mechanical properties of maraging steels aged at different temperatures.

Sample	σ_b, MPa	σ_s, MPa	ε_t, %	U_{OT}, MJ·m^{-3}
A460	1409	1239	9.9	75.8
A480	1850	1642	10.7	112.6
A520	1892	1730	11.5	125.4
A560	1708	1615	11.8	110.5

Note: σ_b - ultimate tensile strength, σ_s - yield strength, ε_t - total elongation, U_{OT} – static toughness.

4.3.2 Microstructural evolution

Fig. 4.1 illustrates the microstructure of maraging steels at different aging temperatures. The microstructural constituents at four different aging temperatures consisted of martensite lath with different orientations and precipitates were observed at high magnification in SEM (inset of Fig 4. 1a). The precipitates were confirmed to be low lattice misfit precipitates of η-Ni_3(Ti,Mo) with hcp crystal structure and B2-Ni(Mo,Fe) with bcc crystal structure, as previously shown by us [122]. They were dispersed in the martensite matrix and grain boundaries during aging. The etched pits in the SEM micrographs are associated with corrosion at precipitate/matrix interface that occurred during etching of steel because of their different interfacial energies ($\gamma_{\text{interface}}$) [123,124]. In the case of A460 steel, the etched pits were small and few. This implied complete precipitation did not occur and was fine in size in the under-aged condition. In the A480 steel, because of higher aging temperature, a high degree of precipitation occurred with evidence of large etched pits after

corrosion (Fig 4. 1b). In contrast, a number of big lenticular etched pits were present in the matrix with granular particles embedded in A520 steel (Fig 4. 1c). This granular phase with micron size is reverted austenite in the matrix and was confirmed in the previous study [120,121]. This kind of reverted austenite occurred at high aging temperature and was distributed in the martensite matrix, which is beneficial to toughness [17,135]. This reverted austenite transformed from granular to lamellar morphology when the aging temperature was increased to 560 ℃. As shown in Fig 4. 1d, the microstructure of A560 steel was comprised of martensite lath, precipitates and lamellar reverted austenite. In view of lamellar shape of reverted austenite, micro-cracks can easily initiate at reverted austenite/matrix interface, which is detrimental to toughness.

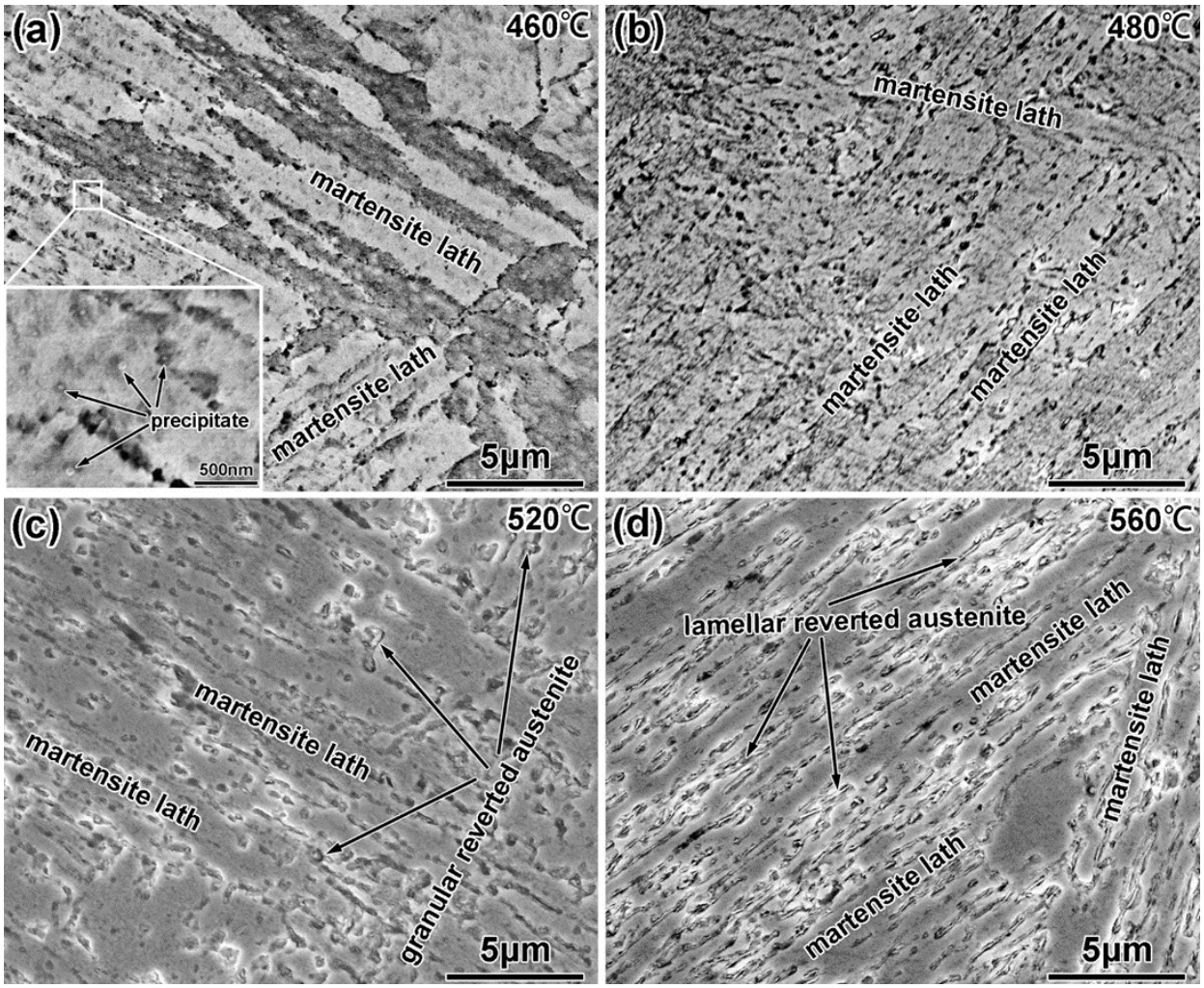

Figure 4. 1 SEM micrographs of maraging steels at different aging temperatures (the precipitates in the inset of Fig. 1a were present in all four steels)

Fig 4. 2 shows the orientation maps of maraging steels at different aging temperatures, as studied by EBSD. In the orientation map of A460 steel, it is clear that the grains had preferred orientation with strong orientations of {101} (Fig 4. 2a). This is because martensite is easy to form along {101} orientations from the habit planes {111} of austenite during air cooling. As the aging temperature was increased, the preferred orientation became weak, and the orientation became relatively more random with different orientations such as {001}, {111} and {112} present in small

sub-grains (Figs. 4.2b-2d). This indicated that at high aging temperature recovery of dislocations in martensite occurred during aging. Because of limitation of EBSD, the reverted austenite could not be identified in the maps.

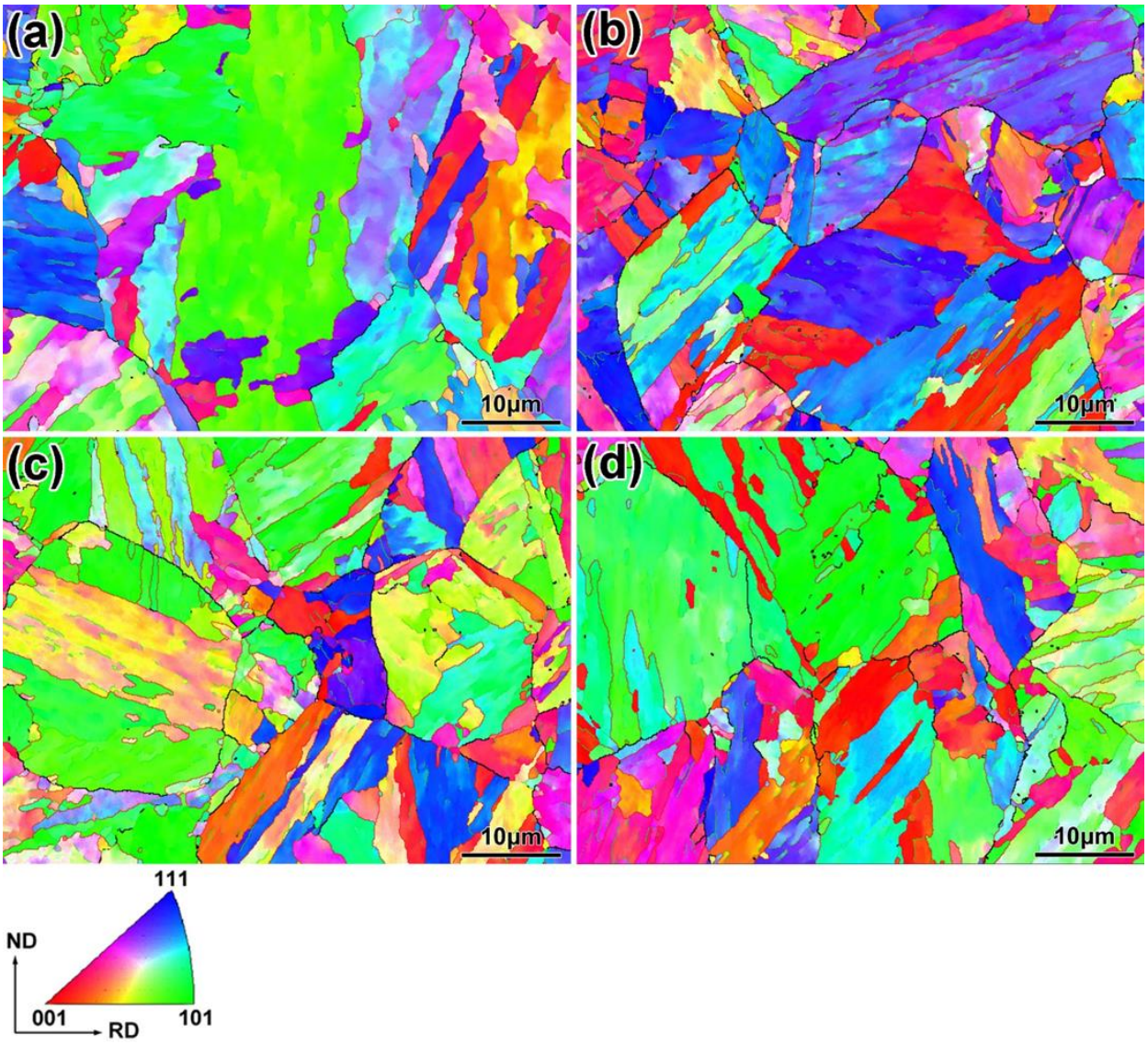

Figure 4. 2 EBSD IPF maps of maraging steels at different aging temperatures of (a) 460 ℃, (b) 480 ℃, (c) 520 ℃ and (d) 560 ℃.

The EBSD band contrast maps with grain boundary misorientation distribution of maraging steels at different aging temperatures are shown in Fig 4. 3. The green lines, black lines

and red lines represent the angle of misorientation below 15°, between 15° and 45° and above 45°, respectively. It can be seen that sub-grain boundary was increased with increase of aging temperature. Meanwhile, the high-angle grain boundaries with misorientation greater than 15° (called HAGB: black lines + red lines) were increased.

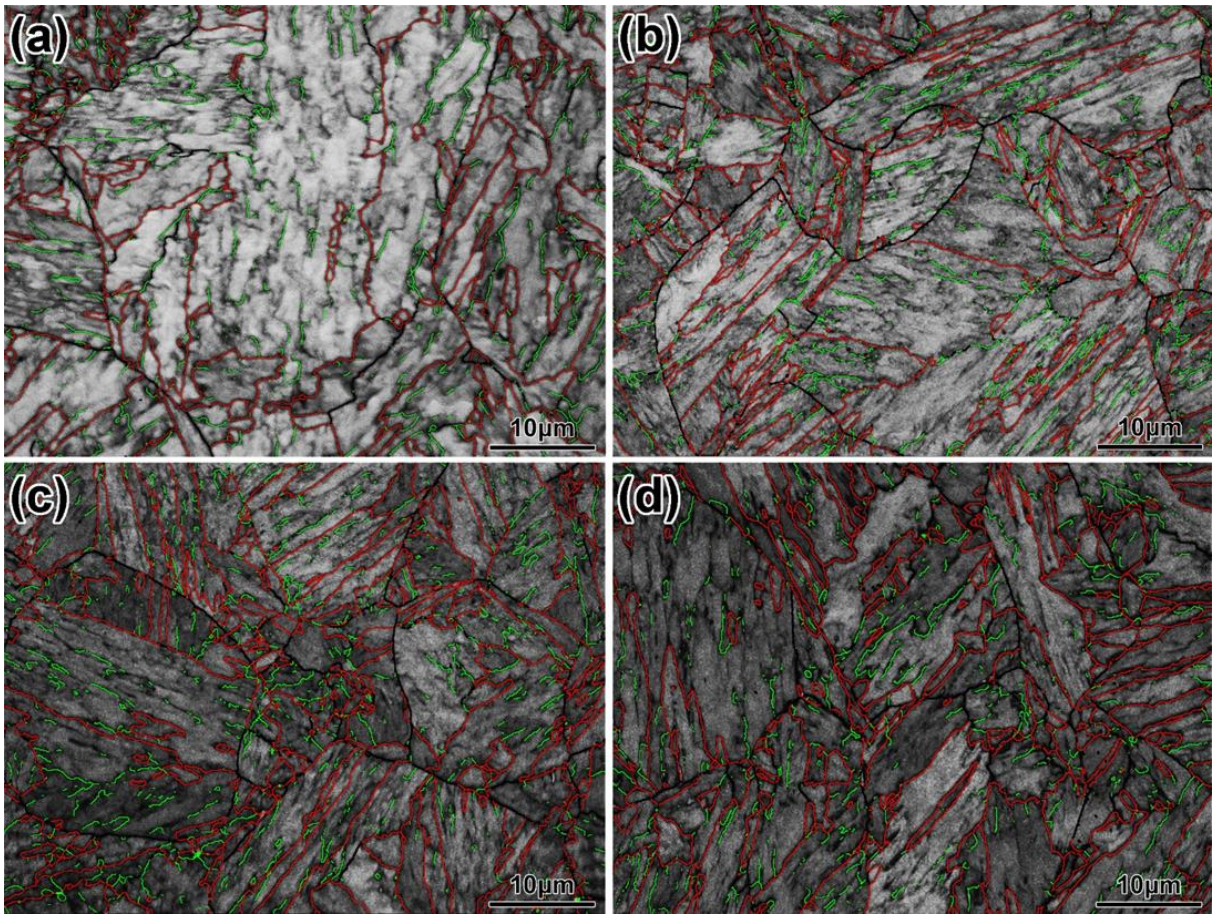

Figure 4. 3 EBSD band contrast maps with grain boundary misorientation of maraging steels at different aging temperatures of (a) 460 ℃, (b) 480 ℃, (c) 520 ℃ and (d) 560 ℃. (green line: < 15°, black line: 15°~45°, red line: > 45°).

The fraction of HAGB and total length of grain boundary per unit area (μm/μm^2) at different aging temperatures were calculated statistically using EBSD grain boundary

misorientation maps and the data is shown in Fig 4. 4. The high-angle grain boundaries (HAGB) can effectively deflect or even arrest the propagation of microcracks, whereas the low-angle grain boundary (LAGB) has less ability to deflect the cracks [126,127]. The fraction of HAGB increased from 12% to 30% as the aging temperature was increased. The high-angle grain boundaries in maraging steel at high aging temperature provide greater resistance to nucleation and growth of microcracks, which is beneficial to toughness. The total length of grain boundary per unit area was increased when aging temperature increased from 460 ℃ to 520 ℃ and had a high value at 560 ℃ (Fig 4. 4). This is because of recovery at higher aging temperature. The residual stress is eliminated, when the dislocation cells and inner dislocation lines in grains disappear by dividing the original martensite laths to several polygonal sub-grains (as shown in Fig 4. 2b-2d), leaving a number of sub-grain boundaries with numerous precipitates distributed along them [128,129].

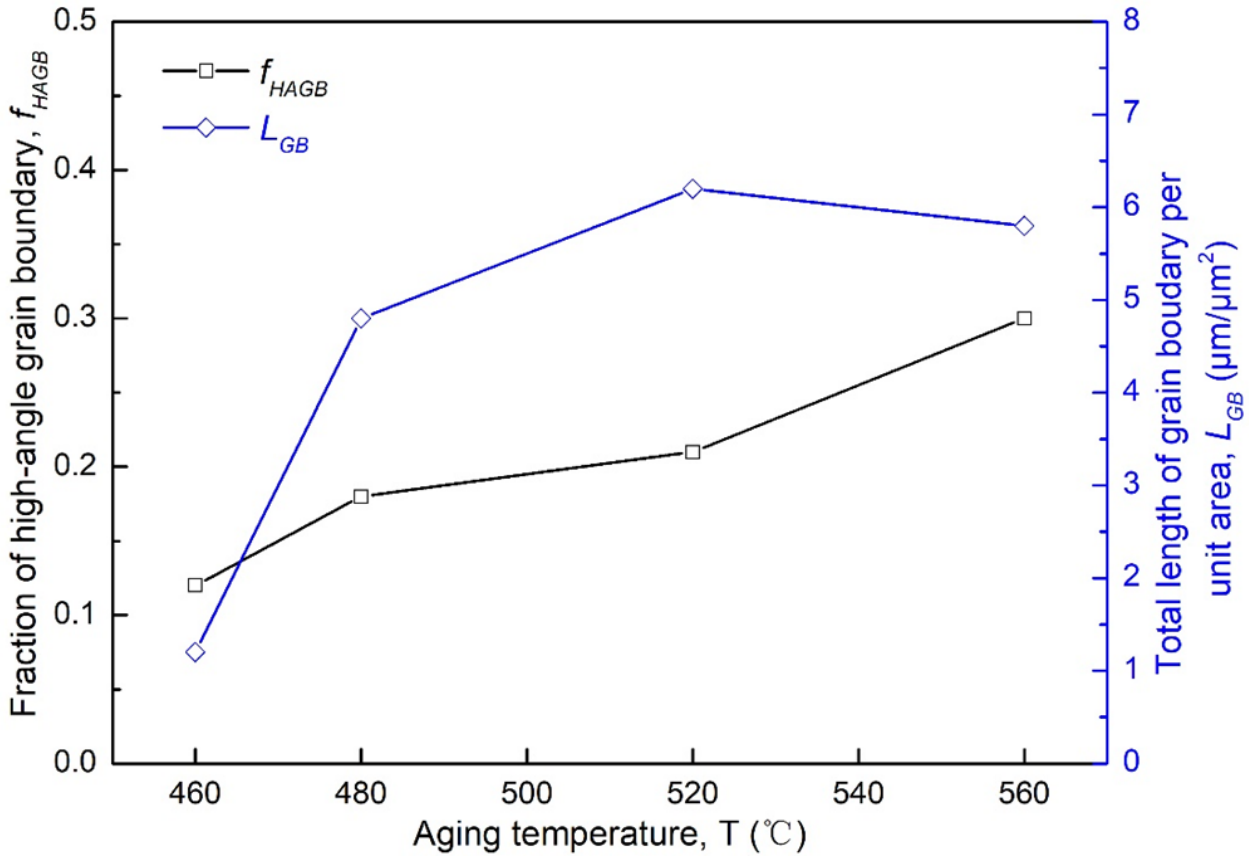

Figure 4. 4 The change in the fraction of high-angle grain boundary (HAGB) and total length of grain boundary per unit area (μm/μm2) at different aging temperatures.

The change in dislocation behavior can also be observed in the result of Kernel average misorientation analyzed by EBSD (Fig 4. 5). Kernel average misorientation (KAM) was used to represent local dislocation density distribution and the recovery fraction. In principle, non-recovered grains have greater maxima of distribution of KAM values because of their high dislocation density, whereas the recovered grains have lower maxima distribution of KAM values [130-132]. It may be seen from Fig 4. 5 that the maxima of distribution of KAM values became lower when the aging temperature was increased (Fig 4. 5e). The distribution of KAM was more uniform at higher aging temperature (Figs. 5a-5d). This indicated that the dislocation density in

martensite lath was decreased with increase of aging temperature, consistent with the aforementioned results. In addition, the KAM maxima shifted towards higher value with increase of aging temperature even though the shift was small but systematic, suggesting more recovery of martensite laths, and is another reason for the superior ductility and toughness at high aging temperature, as listed in Table 4.1.

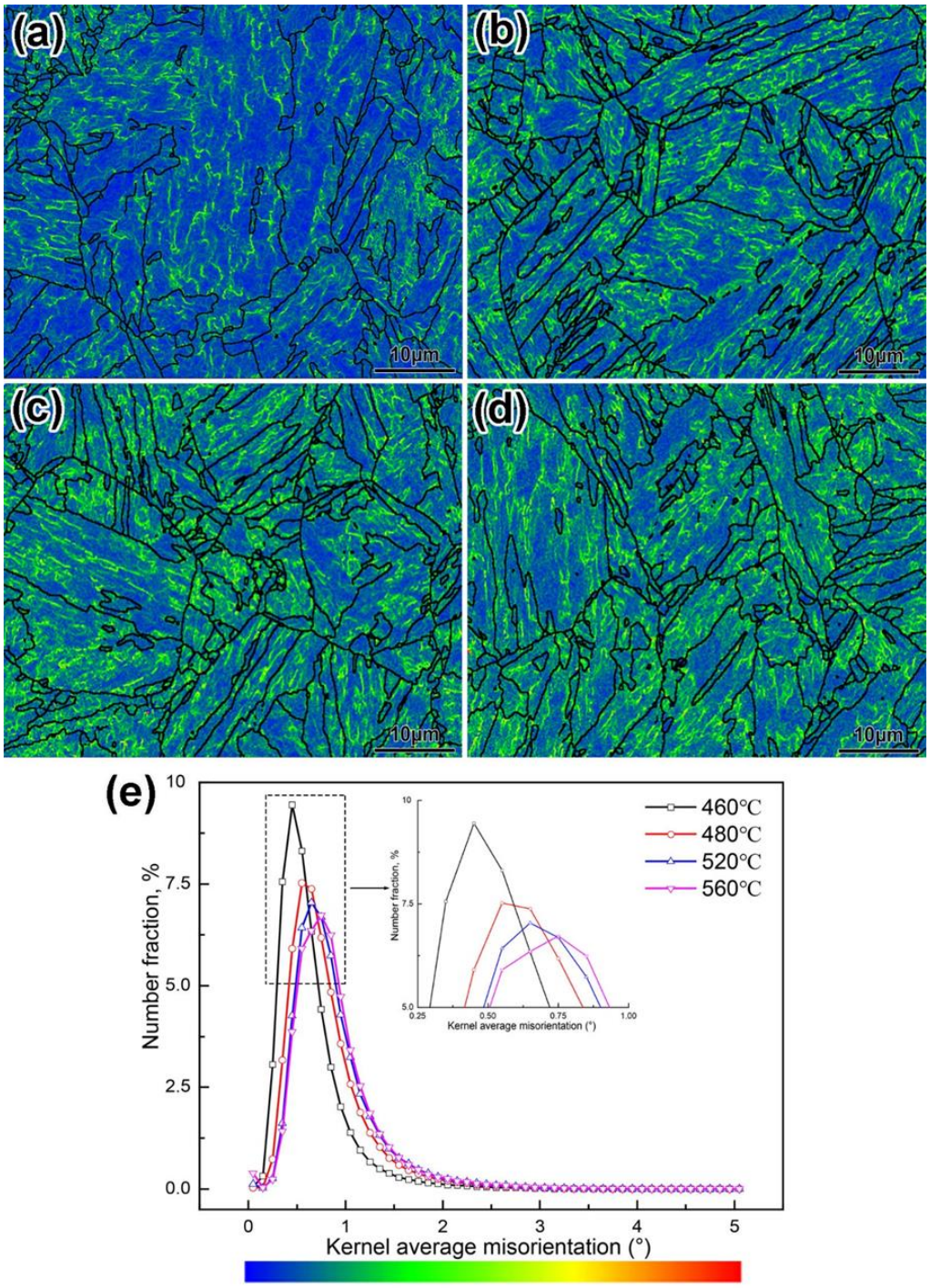

Figure 4. 5 Kernel average misorientation (KAM) maps at different aging temperatures of (a) 460 ℃, (b) 480 ℃, (c) 520 ℃ and (d) 560 ℃, and (e) the distribution of KAM values at different aging temperatures (calculated using neighboring EBSD points of KAM maps at a d distance of 200 nm and up to a maximum deviation of 5°).

The orientation of grains relative to loading direction (Schmid factor) was also examined by EBSD, as shown in Fig 4. 6. The value of different Schmid factor was identified as different colors in Figs.6a, 6c, 6e and 6g. It is noted that majority of martensite laths had Schmid factor greater than 0.4 because of the soft Fe-Ni martensite matrix. However, the Schmid factor of majority of grains shifted to higher value with increase of aging temperature. This suggests that grains in steel subjected to high-temperature aging must glide or deform easily, which contributes to high ductility and toughness.

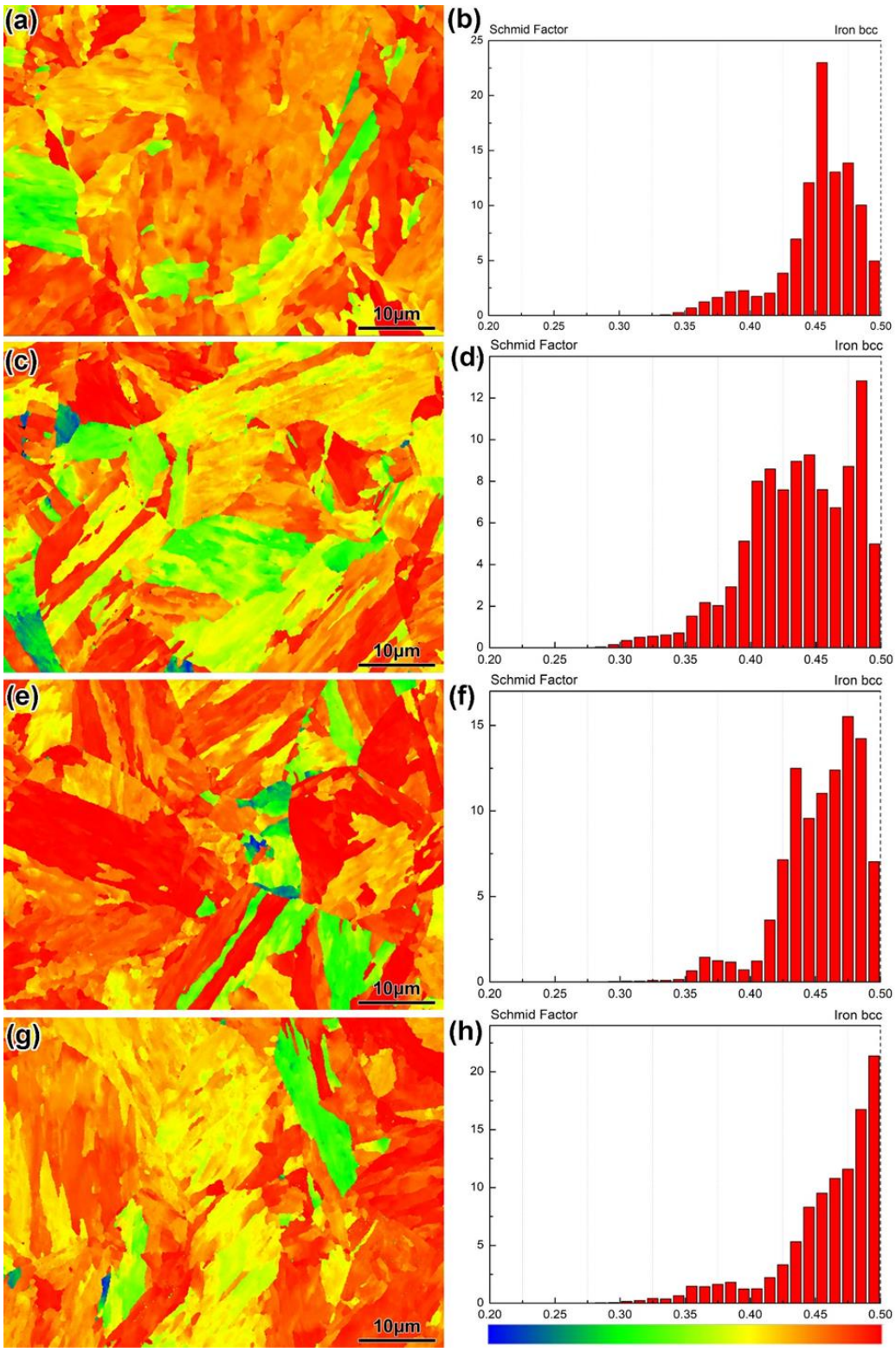

Figure 4. 6 Schmid factor of martensite laths at different aging temperatures analyzed by EBSD: (a) and (b) 460 ℃, (c) and (d) 480 ℃, (e) and (f) 520 ℃, (g) and (h) 560 ℃.

4.3.3 Precipitation behavior

Fig 4. 7 shows TEM micrographs of matrix with Ni3(Ti,Mo) and Ni(Mo,Fe) precipitates distributed homogeneously in martensite lath at different aging temperatures. At low aging temperature of 460 ℃, the martensite lath had preferred-orientation with numbers of dislocations and a few precipitates (Fig 4.7a). In the case of A480 steel, the width of martensite lath did not show an observable change, while the dislocations were decreased. A number of sub-grain boundaries were observed, which appeared to divide the original martensite lath, and the precipitates were increased. Inset shows the selected area electron diffraction pattern (SAED) from the precipitates (Fig 4. 7b). As the aging temperature was increased, reverted austenite was observed in the matrix, besides increased density of precipitates (Figs. 7c and 7d).

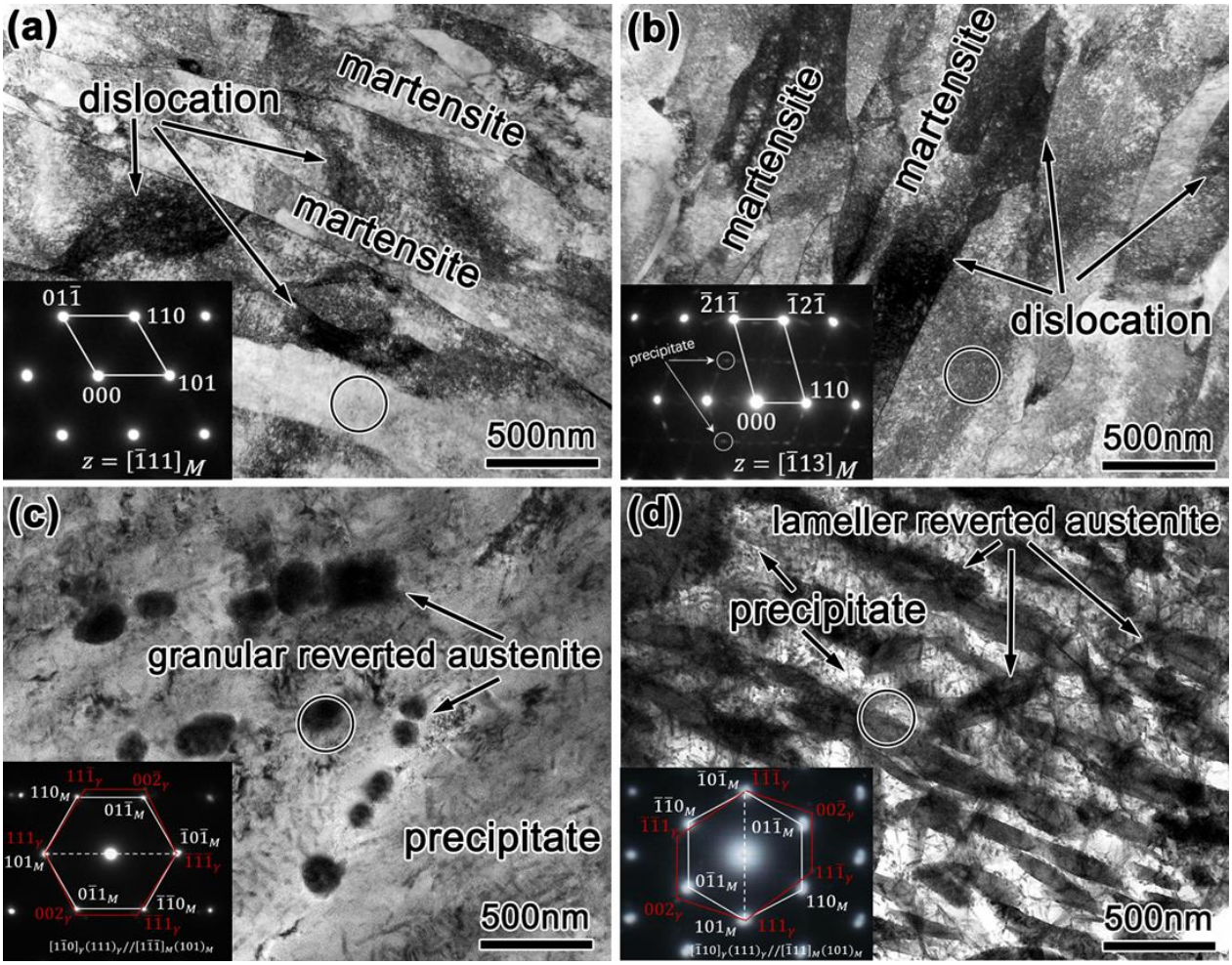

Figure 4. 7 Representative TEM micrographs of maraging steels at different aging temperatures of (a) 460 ℃, (b) 480 ℃, (c) 520 ℃ and (d) 560 ℃. (O-selected area of diffraction pattern)

The reverted austenite changed from granular in A520 steel to lamellar morphology in A560 steel, consistent with SEM observations. The characteristic evolution of Ni3(Ti,Mo) and Ni(Mo,Fe) precipitates at high magnification is illustrated in Fig 4. 8.

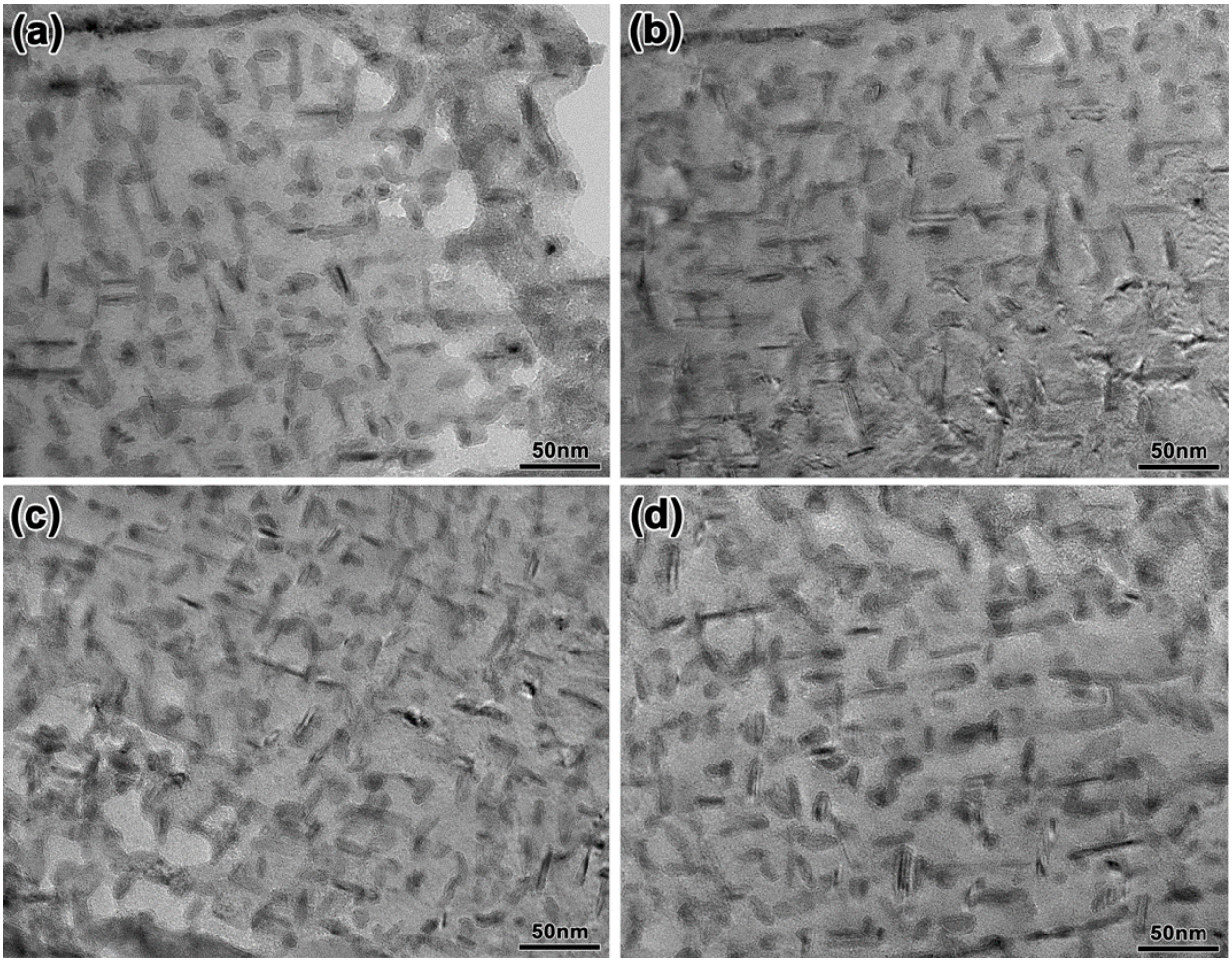

Figure 4. 8 Representative TEM micrographs of precipitates at different aging temperatures of (a) 460 ℃, (b) 480 ℃, (c) 520 ℃ and (d) 560 ℃.

The precipitation behavior was changed with increase of aging temperature, in terms of size, volume fraction, density and interparticle spacing of precipitate, which were statistically measured by Digital Micrograph software. The total volume fraction of nanoscale precipitates (fv) is given by [133]:

$$f_v = \sum \frac{V_i}{V_{total}} \tag{4.1}$$

and the average nanoscale precipitate size ($\overline{d}_{ppt}$), nanoscale precipitate spacing (λ_{ppt}) and

nanoscale precipitate density (ρppt, unit: m^{-3}) were calculated using equations (4.2)-(4.4), respectively [133,134]:

$$\bar{d}_{ppt} = 2R = \sum \left(\frac{V_i}{V_{total}} \cdot d_i\right) \qquad (4.2)$$

$$\lambda_{ppt} = \sqrt{\frac{2\pi}{3 f_v}} \frac{\bar{d}_{ppt}}{2} \qquad (4.3)$$

$$\rho_{ppt} = \frac{6 f_v}{\pi \bar{d}^3_{ppt}} \qquad (4.4)$$

where V_i is the volume of nanoscale precipitates having diameter, di (unit: nm). The corresponding data was statistically acquired from a number of TEM micrographs of precipitates, which is summarized in Fig 4. 9.

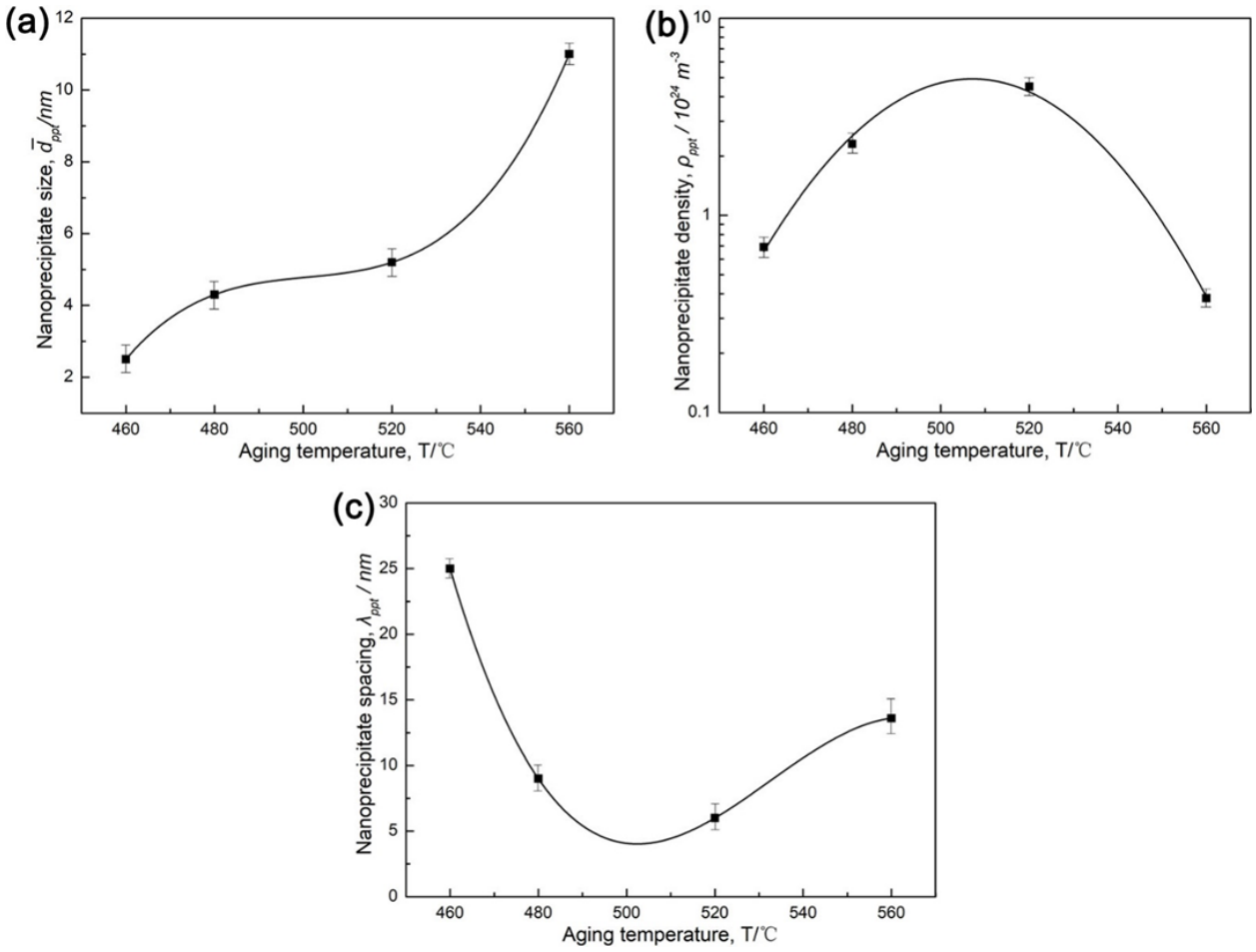

Figure 4. 9 Characteristics of nanoscale precipitates in maraging steel at different aging temperatures.

It can be seen that the average nanoscale precipitate size ($\overline{d}_{ppt}$) increased from ~3 nm to ~10 nm, as the aging temperature was increased. While the nanoscale precipitate density (ρppt) increased from 6.9×1023 m^{-3} (460 ℃) to 4.5×1024 m^{-3} (520 ℃), then decreased to 3.8×1023 m^{-3} (560 ℃). The highest density of nanoscale precipitates was obtained at 520 ℃, which is more than twice of 480 ℃ (2.3×1024 m^{-3}). Meanwhile, the nanoscale precipitate spacing (λ_{ppt}) decreased first and then increased, exhibiting a minimum spacing of ~ 6 nm at 520 ℃. This indicated that

the maraging steel aged at 520 ℃ had highest density (4.5×1024 m-3) of precipitates and lowest interparticle spacing (~ 6 nm), which governs strengthening mechanism.

4.3.4 Strengthening mechanism

It is known that strengthening and toughening of maraging steel is closely related to the phases present in the matrix, including martensite lath, precipitates and reverted austenite. As regards the strengthening mechanism, precipitates are the main strengthening phase in maraging steel, and the remaining strengthening is contributed by the Fe-Ni martensite matrix. Therefore, it is essential to estimate the contribution of precipitates to effective strengthening. There are two well-known mechanisms for precipitation strengthening, shearing mechanism and bypass mechanism [135,136]. The equations for the two contributions are as follows [133,136]:

$$\Delta\sigma_{p-shearing} = (0.538Gb\sqrt{f_v} / \bar{d}_{ppt}) \cdot \ln(\bar{d}_{ppt} / 2b) \tag{4.5}$$

$$\Delta\sigma_{p-bypassing} = cGb / \lambda_{ppt} \tag{4.6}$$

where symbols f_v, $\bar{d}_{ppt}$,λ_{ppt} in equations (4.5) and (4.6) are defined above in equations (4.1-4.4), and $\Delta\sigma_p$ is the yield strength increase associated with precipitates, G=72 GPa is the shear modulus, b=0.248 nm is Burgers vector and c is the correction coefficient [133,137,138].

From equations (45) and (4.6) we note that the strengthening increment from shearing mechanism increases with the increase of precipitate size, while the strengthening increment from bypass mechanism decreases with the increase of precipitate spacing. Combining equations (4.3), (4,5) and (4.6), the critical precipitate size d_c for transformation of strengthening mechanism can be calculated by the following equation:

$$d_c = 2b\exp\left(\frac{c}{0.538}\sqrt{\frac{6}{\pi}}\right) \tag{4.7}$$

The d_c of Ni_3(Ti,Mo) and Ni(Mo,Fe) precipitates was estimated to be 7.4 nm calculated from equation (4.7). The strengthening effect of nanoscale precipitates of size less than 7.4 nm at aging temperature range of 460 ℃~ 520 ℃ was calculated based on shearing mechanism, while for the nanoscale precipitates with size larger than 7.4 nm at 560 ℃, the bypass mechanism was applied (Fig. 4.9a). Beside the strengthening increment from precipitates, the balance is the strengthening increment from martensite. The estimated contributions to yield strength from precipitates and martensite are listed in Table 4.2. It can be seen that at low aging temperature of 460 ℃, when the precipitates were small and the density was low, the strengthening increment from precipitates was ~ 435 MPa. The dominant strengthening contribution was the martensite matrix. With increased precipitation at high temperature, the strengthening increment from precipitates was significantly increased, whilst the strengthening increment from the martensite matrix was decreased. This is related to significant precipitation of Ni containing precipitates from the matrix, which weakened the strengthening effect of Fe-Ni martensite. The precipitates exhibited maximum strengthening effect with a value of 1463 MPa at 520 ℃, when the strengthening increment from the martensite matrix was the lowest. The formation of reverted austenite at this temperature further decreases the strengthening effect of martensite, and reverted austenite is beneficial to toughness. Thus, maraging steel aged at 520 ℃ had ultrahigh strength and high toughness, without sacrificing ductility (Table 4.1). When the aging temperature was greater than 520 ℃, growth of precipitates occurred and part of them redissolved into the martensite matrix. As a result, the hardening mechanism transformed from shearing to bypass. The strengthening increment from precipitates decreased to 1064 MPa, while the strengthening effect of martensite had a contribution of 551

MPa. Martensite did not provide high strength similar to that at low aging temperature because of the formation of significant content of lamellar reverted austenite that provides high ductility and toughness.

Table 4. 2 Contribution of precipitates and martensite to yield strength of maraging steels aged at different temperatures.

Sample	$\Delta\sigma_s$, MPa	$\Delta\sigma_p$, MPa	$\Delta\sigma_m$, MPa
A460	1239	435	804
A480	1642	1250	392
A520	1730	1463	267
A560	1615	1064	551

4.4 CONCLUSIONS

The best combination of high-strength and high-toughness was obtained at aging temperature of 520 ℃, without sacrificing ductility. The ultimate strength and static toughness at this peak aged condition were 1850 MPa and 125.4 MJ·m-3, respectively.

The microstructural constituents in maraging steels were strongly influenced by the aging temperature. Low lattice misfit nanoscale precipitates and martensite matrix were the primary constituents in maraging steels aged at different temperatures. The reverted austenite was obtained at high aging temperature above 520 ℃, whose morphology changed from granular to lamellar, with expected impact on toughness of maraging steel.

In A460 steel, martensite had a preferred orientation of {101}. As the aging temperature was increased, the preferred orientation was weakened. The fraction of high-angle grain boundary (HAGB) and total length of grain boundary per unit area (μm/μm2) were increased because of

recovery of martensite laths at higher aging temperature, with consequent formation of sub-grains. This had a beneficial impact on the strengthening and toughening of maraging steel, consistent with the analyses of KAM value and Schmid factor obtained by EBSD.

With increase of aging temperature, the size of nanoscale precipitates was increased from ~3 nm to ~10 nm. The nanoscale precipitate density first increased and then decreased with maximum of 4.5×1024 m-3 at 520 ℃. The trend in interparticle spacing was opposite, with lowest spacing of ~ 6 nm at 520 ℃. The characteristics of precipitation (size, density and interparticle spacing) at different aging temperatures governed the strengthening contribution and mechanism.

4.5 SUMMARY

In this chapter, we studied the dependence of aging temperature on the microstructural evolution and accompanying change in strengthening in cobalt-free maraging steel.: We elucidate here the impact of aging temperature on microstructural evolution and strengthening behavior on low lattice misfit cobalt-free maraging steel. The best combination of high-strength (1850 MPa) and high-toughness (125.4 $MJ \cdot m^{-3}$) was obtained at the optimal aging temperature of 520 ℃, without sacrificing ductility. Electron back scattered diffraction studies suggested that preferred orientations of {101}, fraction of high-angle grain boundary (HAGB) and total length of grain boundary per unit area ($\mu m/\mu m^2$) were increased with increase of aging temperature, which was beneficial to both strengthening and toughening of maraging steel. The strengthening contribution from the precipitates was transformed from shearing mechanism to bypass mechanism when the aging temperature is greater than 520 ℃. The aging tempered steel of 520 ℃ provided maximum strengthening increment of 1463 MPa through shearing mechanism, while granular reverted austenite at this temperature contributed to high toughness.

Chapter 5 Interaction between low lattice misfit precipitates and martensitic MATRIX

5.1 INTRODUCTION

Based on the aforementioned research, optimizing the microstructure via change in solution and aging temperature-time combination have been achieved. Meanwhile the deformation mechanism that contribute to high ductility of cobalt-free maraging steels comprising of high density of low lattice misfit nanoscale precipitates has not been explored to the best of our understanding. the objective of this chapter is to elucidate the deformation behavior of cobalt-free maraging steel via post-mortem electron microscopy of tensile strained samples.

5.2 EXPERIMENTAL DETAIL

The samples for microstructural observations by optical microscopy (OM) and scanning electron microscopy (SEM) were metallographically polished using standard procedure and etched with modified Fry's regent (50ml HCl + 25ml HNO_3 + 1g $CuCl_2$ + 150ml H_2O). TEM studies were carried out using 200 kV FEI Tecnai G2 F20 transmission electron microscope on samples in aged condition and post-mortem electron microscopy of the tensile strained condition near the fracture tip (please see Fig 5.1 for location). The foils were twin-jet electropolished in a solution of 5% perchloric acid and 95% ethanol at 253 K. The characteristics of nanoscale precipitate were statistically analyzed by MATLAB software and Nano-measurer software, using a number of TEM micrographs of the type presented in Fig 5. 2c. At least 30 micrographs of each steel and more than 2000 nanoscale precipitates were assessed for measurements.

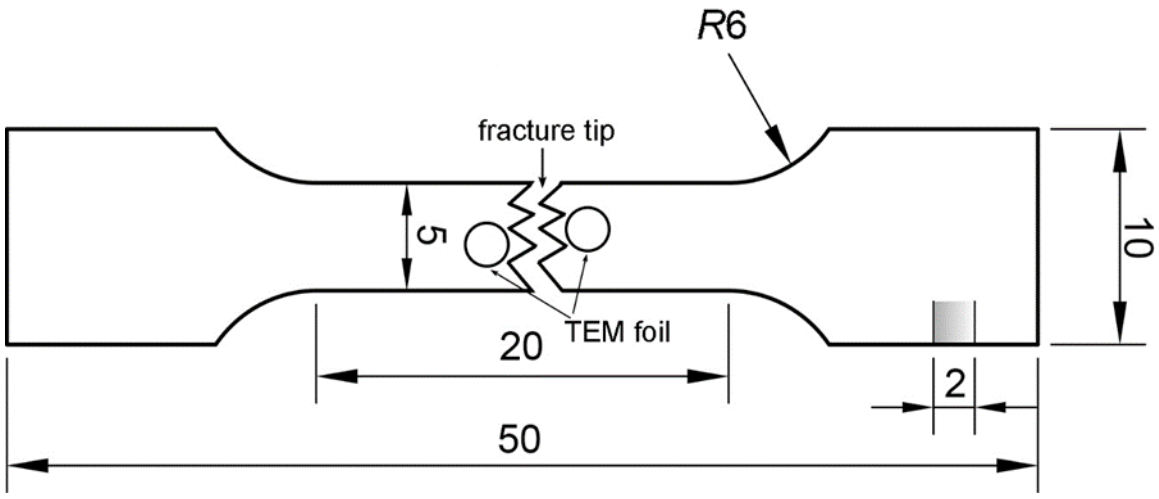

Figure 5. 1 Dimensions of the tensile specimen and the location from where the TEM foils were prepared after tensile straining. All dimensions are in mm).

5.3 RESULTS AND DISCUSSION

5.3.1 Mechanical properties and microstructure of (undeformed) maraging steel

Prior to describing the deformation mechanisms, which contributes the focus of study, it is appropriate to first briefly visit and describe the tensile properties and microstructure that contributed to ultrahigh strength and elongation. The tensile properties of solution-annealed parent metal and aged maraging steel are listed in Table 5.1. Ultimate tensile strength and total elongation of solution-annealed parent metal were 912 MPa and 13.8%, respectively, and the static toughness had a high value of 82.9 $MJ \cdot m^{-3}$. On aging, the ultimate tensile strength was increased from 912 MPa to 1860 MPa, while the static toughness continued to remain high at 112.5 $MJ \cdot m^{-3}$. Fig 5. 2 shows the corresponding microstructure of undeformed maraging steel and the engineering stress-strain plots. The solution-annealed parent metal was composed of lath martensite (Fig 5. 2a). After aging, a high density of dislocations (Fig 5. 2b) and precipitates (Fig 5. 2c) in lath martensite with straight martensite lath boundaries were observed. A number of these precipitates were analyzed to be $Ni_3(Ti,Mo)$ by selected area electron diffraction pattern presented in the inset of Fig 5. 2c.

$Ni_3(Ti,Mo)$ contributes to strength [139]. The precipitates were further studied in detail using high resolution TEM and Fig 5. 2d shows that the strength of aged steel increased to ~0.95 GPa compared to the solution-annealed parent metal.

Table 5. 1 Tensile properties of experimental steels.

Sample	Ultimate tensile strength, MPa	Total elongation, MPa	Static toughness, MJ·m-3
As-solution-annealed	912	13.8	82.9
As-solution-annealed+aged	1860	10.2	112.5

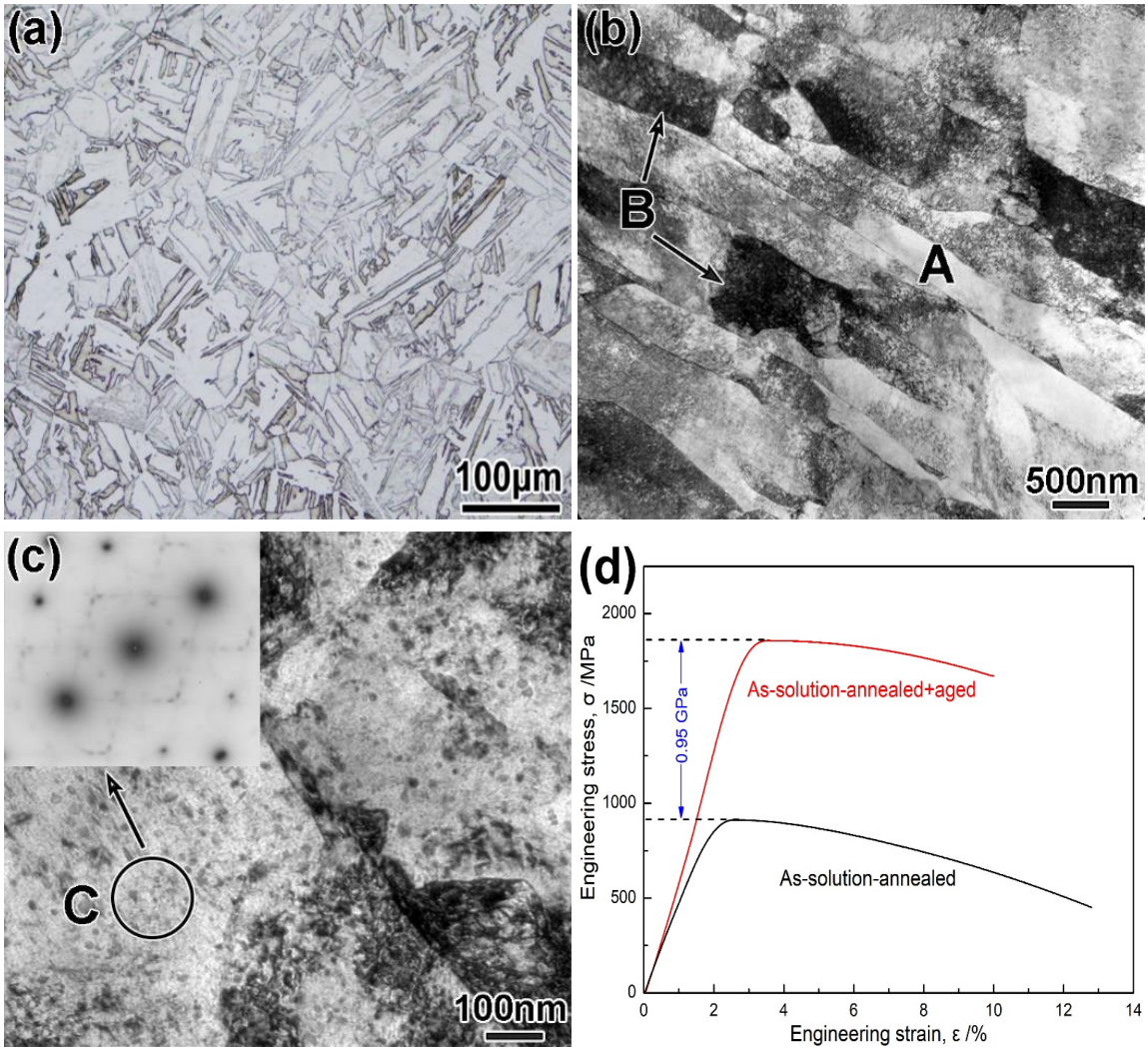

Figure 5. 2 (a) Light micrograph of solution annealed parent metal, (b) low magnification TEM micrograph of maraging steel aged at 480 ºC, (c) high magnification TEM micrograph of aged maraging steel and inset is selected area electron diffraction pattern and (d) engineering stress-engineering strain plot. (A-lath martensite, B-dislocation, C-precipitates)

Considering nanoscale precipitates to be spherical, the total volume fraction of nanoscale precipitates (f_v) is given by [140]:

$$f_v = \sum \frac{V_i}{V_{total}} \tag{5.1}$$

and the average nanoscale precipitate size ($\overline{d}_{ppt}$), nanoscale precipitate spacing (λ_{ppt}) and nanoscale precipitate density (ρ_{ppt}, unit: m^{-3}) were determined by equations (2)-(4), respectively [140,141]:

$$\overline{d}_{ppt} = 2R = \sum \left(\frac{V_i}{V_{total}} \cdot d_i\right) \tag{5.2}$$

$$\lambda_{ppt} = \sqrt{\frac{2\pi}{3 f_v}} \frac{\overline{d}_{ppt}}{2} \tag{5.3}$$

$$\rho_{ppt} = \frac{6 f_v}{\pi \overline{d}^3_{ppt}} \tag{5.4}$$

where $\frac{V_i}{V_{total}}$ is the volume fraction of nanoscale precipitates having diameter, d_i (unit: nm). Furthermore, the average width of martensite lath (W_m) was also measured by MATLAB software from more than 20 TEM micrographs. Based on equations (5.2)-(5.4), the characteristic evolution of nanoscale precipitate (size, volume fraction, density and spacing between nanoscale precipitates) and the width of martensite lath are listed in Table 5.2. The density of nanoscale precipitates was extremely high at 2.3×10^{24} m^{-3} and the average diameter of nanoscale precipitates was ~4.6 nm. Nanoscale precipitate spacing was ~11.2 nm, and the width of martensite lath was ~0.33 μm. Based on the well-known Orowan mechanism [142], the increase in yield strength due to precipitation strengthening is attributed to a decrease in the precipitate size and the spacing which can increase not only the force of dislocation movement, but also dislocation density. These parameters are of particular significance to ultrahigh strength of maraging steel.

Table 5. 2 Characteristics of nanoscale precipitates.

Sample	W_m (μm)	$\bar{d}_{ppt}$ (nm)	ρ_{ppt} (m^{-3})	λ_{ppt} (nm)
Aged maraging steel	0.33±0.04	4.6±0.5	2.3×10^{24}	11.2±0.8

Note: Wm-average width of martensite lath, -average nanoscale precipitate size, ρppt-nanoscale precipitate density, -nanoscale precipitate spacing.

Figs. 5.3 and 5.4 are high resolution TEM micrographs of nanoscale precipitates in aged steel. There were two types of nanoscale precipitates, and both of them were characterized by superlattice diffraction pattern. Fig 5. 3a shows that the points in the box with broken lines of 2D lattice image of nanoscale precipitate indicated an alternating bright and dark superlattice pattern. In contrast, the points in the box with solid lines of 2D lattice image of the matrix (Fig 5. 3a) had similar brightness, indicated by M. This is the difference in the real space between precipitates and the matrix, while the superlattice diffraction spots is the difference in the reciprocal space between the nanoscale precipitate and matrix. The differences in the high resolution image of nanoscale precipitates and matrix were clearly distinguished by the inverse fast Fourier transformation (IFFT) image (Fig 5. 3c). The IFFT micrograph (Fig 5. 3c) showed a distinct difference between the matrix and precipitates. Combining the fast Fourier transformation (FFT) image (Fig 5. 3b), selected area electron diffraction pattern (Fig 5. 3d) and indexed diffraction pattern (Fig 5. 3e), the nanoscale precipitate was identified to be η-Ni_3(Ti,Mo), which was further confirmed from the analysis of energy dispersive X-ray spectroscopy (atomic ratios of Ni, Ti and Mo in Fig 5. 3f). Based on the diffraction pattern, the η-Ni_3(Ti,Mo) had hcp structure [143,144]. The atomic arrangement of

$Ni_3(Ti,Mo)$ in Fig 5. 3a is identified by a box with broken lines. The crystal orientation relationship between $Ni_3(Ti,Mo)$ nanoscale precipitate and the matrix was $(01\bar{1}2)_\eta // (110)_\alpha$, $[\bar{2}110]_\eta // [001]_\alpha$.

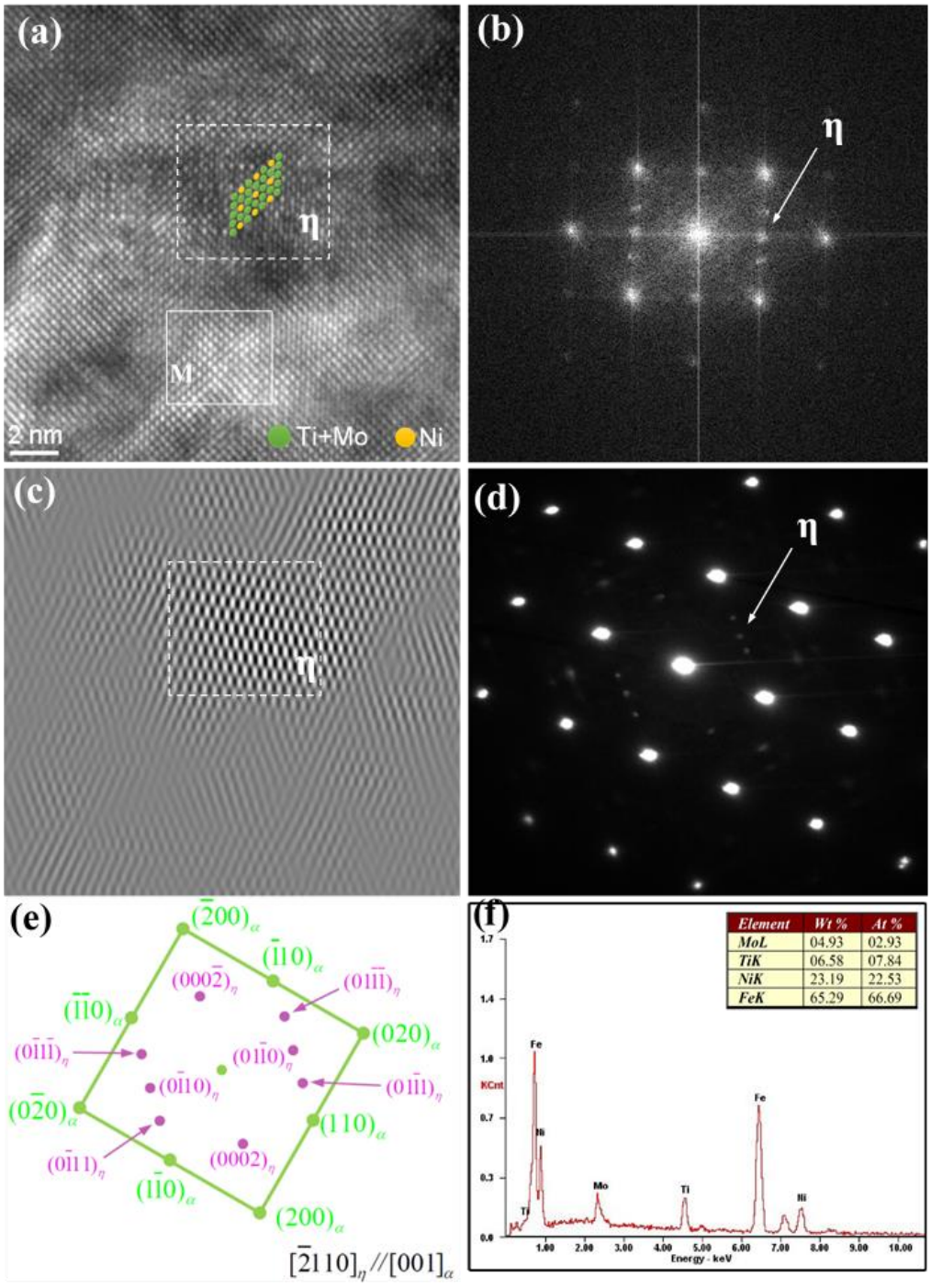

Figure 5. 3 (a) Representative high resolution image of η-Ni3(Ti,Mo) nanoprecipitate in maraging steel along [001]α direction, (b) FFT image of (a), (c) IFFT image of (a), (d) selected area electron diffraction pattern of (a), (e) indexed diffraction pattern of (b) and (d) and (f) EDS of η-Ni3(Ti,Mo) nanoprecipitate in (a).

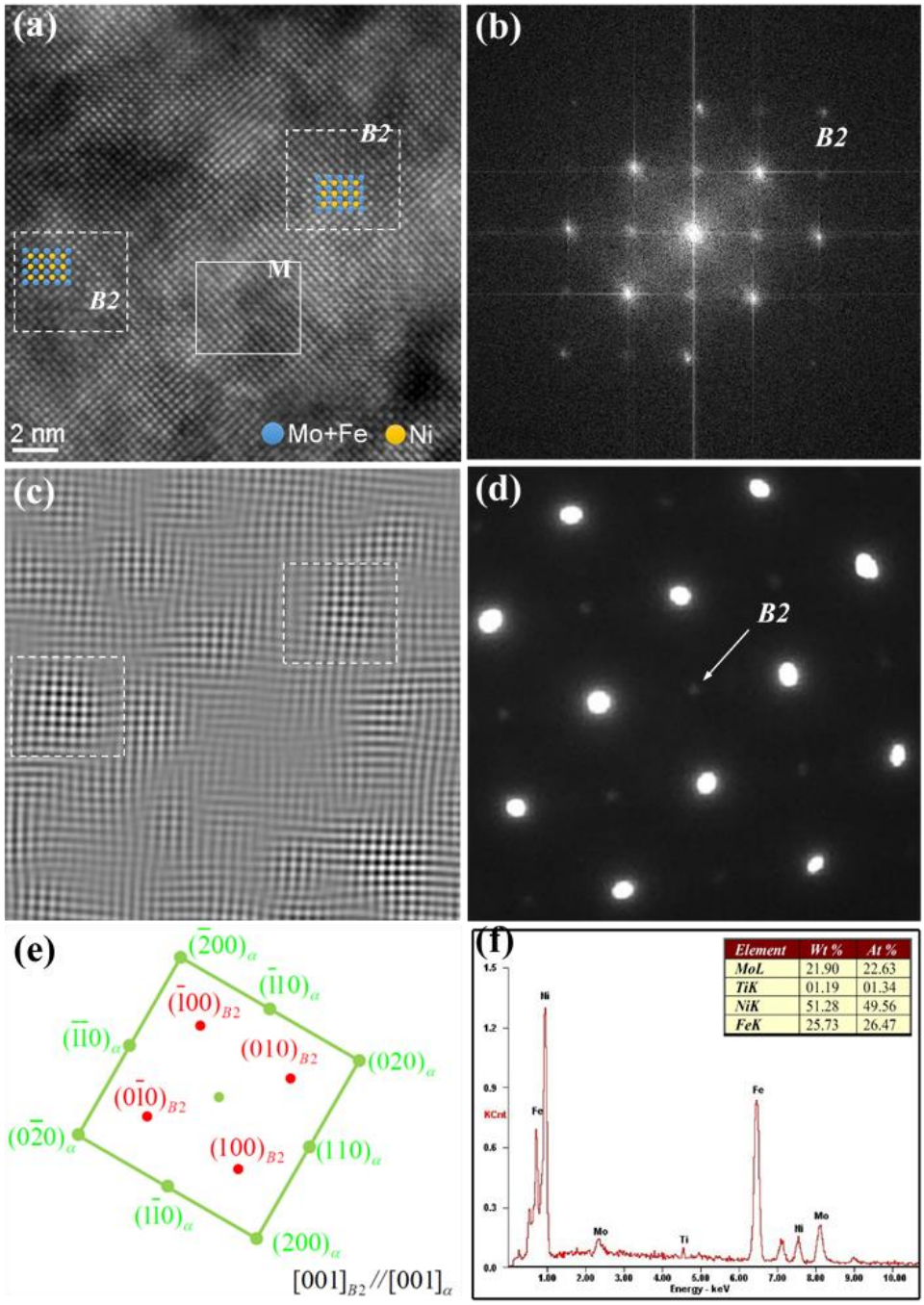

Figure 5. 4 (a) Representative high resolution image of B2-Ni(Mo,Fe) nanoprecipitate in maraging steel along [001]α direction, (b) FFT image of (a), (c) IFFT image of (a), (d) selected area electron diffraction pattern of (a), (e) indexed diffraction pattern of (b) and (d) and (f) EDS of B2-Ni(Mo,Fe) nanoprecipitate in (a).

Adopting an approach identical to that of characterizing the structure of $Ni_3(Ti,Mo)$, the second type of nanoscale precipitate was identified to be B2-Ni(Mo,Fe) (Fig 5. 4a-4f) with bcc structure, and the crystal orientation relationship between Ni(Mo,Fe) nanoscale precipitate and matrix was $(110)_{B2}//(110)_{\alpha}$, $[001]_{B2}//[001]_{\alpha}$. The a-axial lattice constants of η-$Ni_3(Ti,Mo)$, B2-Ni(Mo,Fe) and matrix were a_{η}=0.2847 nm, a_{B2}=0.2890 nm and a_m=0.2864 nm, respectively, which are similar to the lattice constant of α-Fe matrix in maraging steel, a_m=0.288 nm [145,146]. The lattice misfit (δ) between η-$Ni_3(Ti,Mo)$ and B2-Ni(Mo,Fe) with the matrix was only 0.6% and 0.9%, respectively, implying that both types of two nanoscale precipitates were coherent with the matrix. In comparison to Co-containing maraging steel, the presence of Co can decrease the solubility of Mo in the martensite matrix and suppresses the nucleation of dislocations in the matrix, which leads to more Mo-containing precipitates in Co-containing maraging steel, such as Fe_2Mo, Fe_7Mo_6. These precipitates coarsen easily and are semi-coherent or incoherent with the martensite matrix (δ＞5%). The dislocations cut and/or bypass the precipitates [147]. In contrast, in Co-free maraging steel, the high coherency of η-$Ni_3(Ti,Mo)$ and B2-Ni(Mo,Fe) precipitates with the matrix (δ＜1%) and nanoscale size with very low elastic strain are envisaged to contribute relatively less to dislocation interactions. The strengthening here is primarily associated with chemical ordering that produces back stresses that restrict elastic deformation when precipitates cut dislocations [148].

In summary, highly dislocated lath martensite and high density of low lattice misfit nanoscale precipitates contributed to ultrahigh strength in cobalt-free maraging steel. In contrast to the Ni_3Ti and Ni_3Mo strengthening precipitates in traditional 18Ni maraging steel, the strengthening in the experimental steel studied here is achieved through very high density (2.3×10^{24} m^{-3}) of low lattice misfit (~0.6%) precipitates (η-$Ni_3(Ti,Mo)$ and B2-Ni(Mo,Fe)) with the matrix and high antiphase boundary energy, without loss of ductility. The low lattice misfit

precipitate is envisaged to reduce the nucleation barrier for precipitation. Moreover, the low lattice misfit is expected to lower the elastic misfit energy between the precipitate nuclei and the matrix [148]. Lastly, the low interfacial energy of the precipitates in the martensite matrix reduces the energy barrier required for homogeneous precipitation of η-Ni_3(Ti,Mo) and B2-Ni(Mo,Fe). The number density of nanoscale precipitates is significantly greater than traditional cobalt-containing 250 maraging steels. This observation leads us to suggest that low lattice misfit approach is responsible for the very high density of precipitates. The aforementioned characteristics led to a remarkable combination of ultrahigh strength (UTS of 1860 MPa) and good ductility (10.2%) in our 19Ni3Mo1.5Ti experimental maraging steel. This combination of ultrahigh strength and good ductility is attributed to the following: First, the homogenous distribution of high density of low lattice misfit nanoscale precipitates (~5 nm) effectively reduce stress concentration at the precipitate/matrix interface, which is the primary challenge in traditional maraging steels. Second, the associated elastic interaction between precipitates and cutting dislocations is less because of low lattice misfit (~0.6%), preventing crack initiation at the precipitate/matrix interface because of negligible strain accumulation. Third, the high content of solute Ni (19 wt% in our case) in the matrix has an important role in reducing the tendency for cleavage, lowering the ductile–brittle transition temperature of steels [148,149]. In summary, the strengthening is obtained via high density of low lattice misfit coherent precipitates that require high cutting stress to enable dislocations to cut through the precipitates.

5.3.2 Deformation mechanisms in tensile strained maraging steel

Fig 5. 5 shows that there was a dramatic change in the morphology of lath martensite during tensile deformation from lath-type to wavy-type morphology. Some laths were broken and transformed into smaller laths. In comparison to the near straight lath-type morphology of undeformed maraging steel, the lath boundaries were wavy and discontinuous (marked by yellow broken lines). Furthermore, there was significant localization or enrichment of dislocations at the wavy boundaries. Two types of martensite matrix can be defined, referred as M1 and M2. The bright and large lath martensite (M1) contained less number of dislocations. The dark lath martensite (M2) was characterized by high density of dislocations (Fig 5. 5a-5c). The dislocation groups are most likely to be a consequence of high mobility and pile-up of different dislocations on different slip planes (Fig 5. 5d). In martensitic steels, there are four $\{111\}_\gamma$ habit planes involved in martensite/austenite transformation, which obey $\{110\}_\alpha$ // $\{111\}_\gamma$ irrespective of the orientation relationship between martensite and austenite, i.e., K-S, N-W or G-T. Given that the dislocations can easily slip on habit planes, the martensite lath is deformed to wavy shapes and several polygonal parts with angles of 30°, 60° or 120° (Fig 5. 5a-5c). The main slip planes that were identified include $(110)_\alpha$, $(101)_\alpha$, $(01\bar{1})_\alpha$, $(12\bar{1})_\alpha$ and $(211)_\alpha$, as indexed along the wavy lines in Fig 5. 5, consistent with the fact that $\{110\}$ and $\{112\}$ are common glide planes in body-centered cubic structure (bcc).

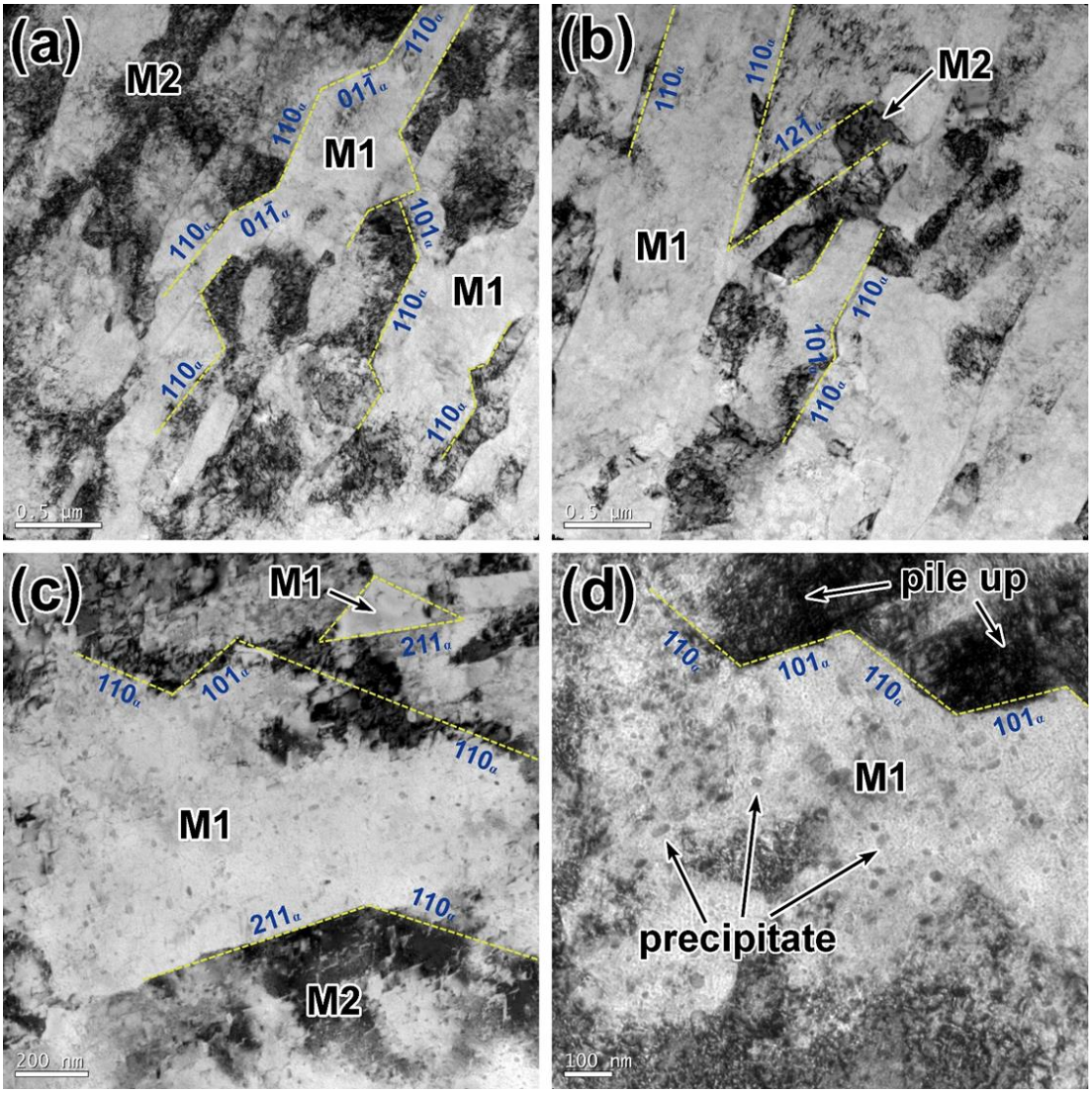

Figure 5. 5 TEM micrographs illustrating the morphology of tensile strained maraging steel in different areas (M1-bright lath martensite, M2-dark lath martensite with high density of dislocations).

It is envisaged that during deformation, a number of edge and screw dislocations are gradually generated. The interaction of edge and screw dislocations occurs when the deformation stress (σ_d) exceeds the critical resolved shear stress (CRSS) of dislocations, i.e., $\sigma_d \geq CRSS_{dislocation}$. This leads to two types of dislocation mobility in the martensite matrix, as schematically illustrated in Fig 5. 6. The intersection and movement of edge and screw dislocations enable slip and climb

to occur on another gliding plane (Fig 5. 6b). Jog is formed from edge dislocation, and kink is formed from screw dislocation (Fig 5. 6c and 6d). Hence, dislocations in the martensite matrix contained substantial number of kinks and jogs as compared to a straight line. These defects within a defect significantly influence the mobility of dislocations and are of relevance in the observed deformation.

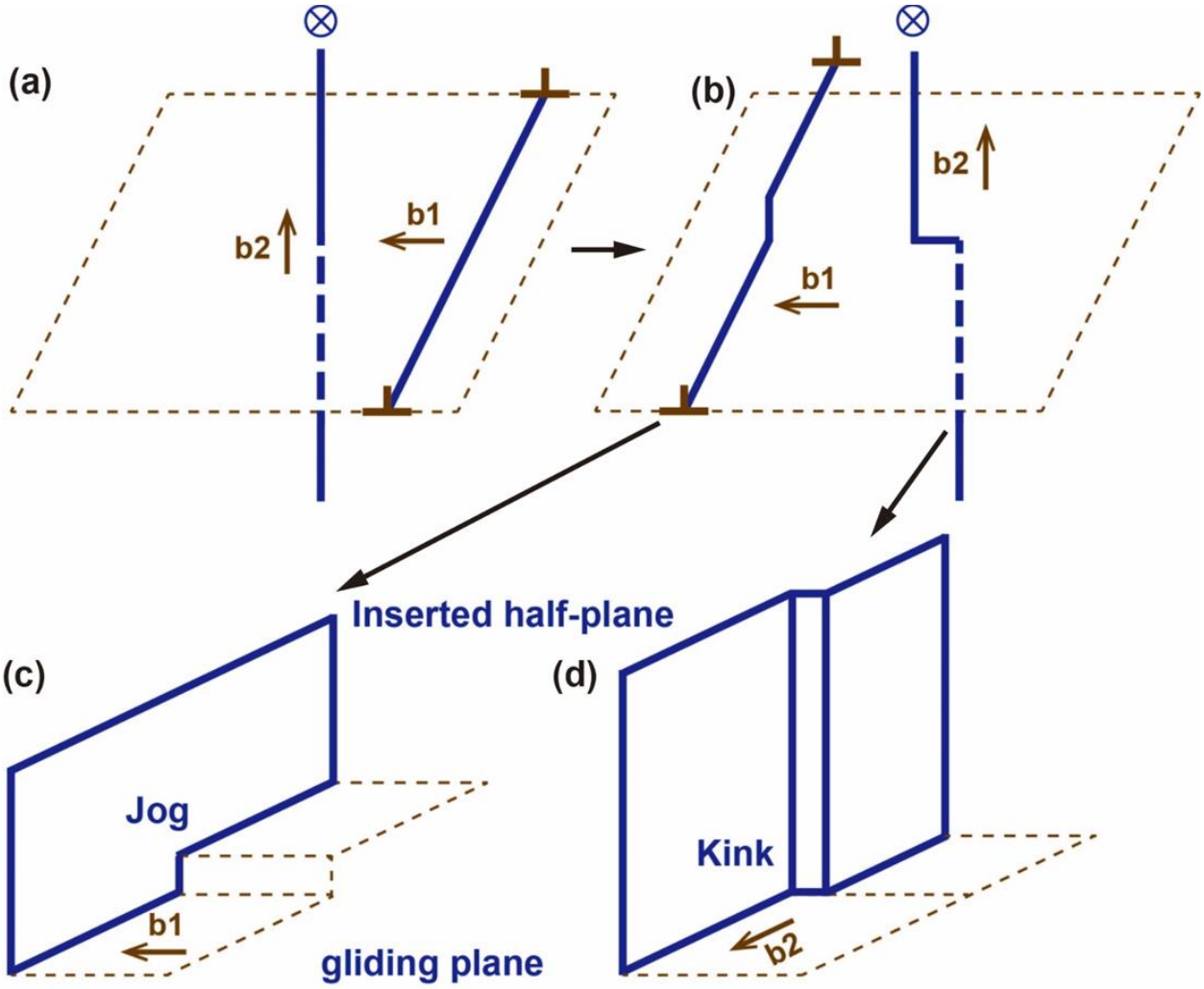

Figure 5. 6 Interactive mobility of dislocations and consequent defects (b1-edge dislocation and b2-screw dislocation).

The transformation of kinks and jogs is schematically illustrated in Fig 5. 7. The kinks and jogs are formed on the slip planes and at the intersectional regions, respectively. With increased

tensile deformation, the progressive formation of jogs and kinks occurs across the entire martensite lath and consequently separated the martensite lath via easy gliding planes to form the wavy martensite lath and small martensite lath with preferred orientation of lath boundaries, as shown in Figs. 5b and 5c. In addition, a part of jogs remained in the martensite lath (M2 in Fig 5. 5c) because of insufficient internal driving force for mobility. A TEM micrograph illustrating such a region is presented in Fig 5. 8a and a magnified view of the corresponding area is shown in Fig 5. 8b. The jogs were comprised of two short dislocations with different orientation, indicated by the small broken lines in the rectangular boxes in Fig 5. 8b. They are designated as stair-rod dislocations, which are partial dislocations that are formed when a dissociated dislocation bends over from one glide plane to another or interacts with a dislocation on another glide plane. Among them, the best known is the formation of Lomer-Cottrell locks [150]. These locks are formed by two stacking faults (a pair of extended dislocations) meeting at the intersection of two slip planes and connected by a stair-rod dislocation. Considering that this kind of lock is practically immobile, it is recognized as one of the most difficult obstacles for dislocations to surpass because of the resistance to glide and climb of dislocations even under an inverse stress. As a consequence, jogs in the local severely strained region were formed because of the pile-up of dislocations and stress concentration (Fig 5. 5d).

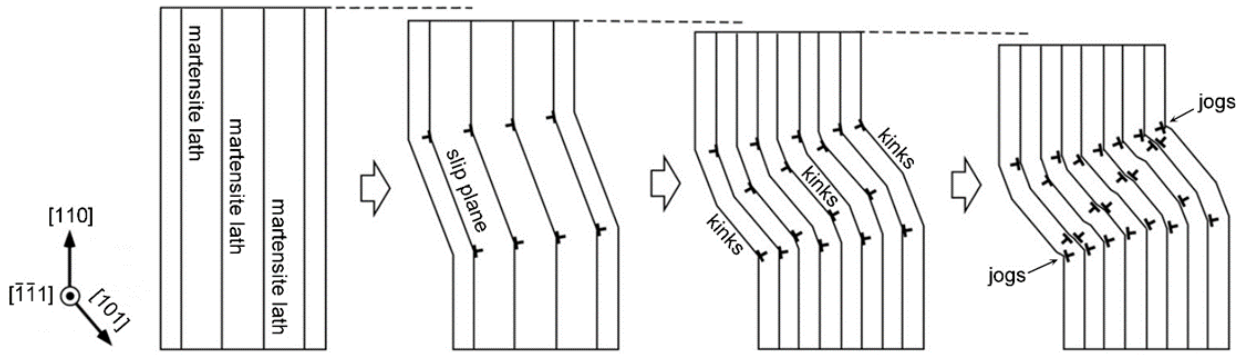

Figure 5. 7 Transformation from straight to wavy martensite lath induced by kinks and jogs via mobility of dislocations on easy slip planes.

Some precipitates observed in the martensite lath (Fig 5. 5c and Fig 5. 5d) were observed to interact with dislocations. This interaction between dislocations and precipitates observed in tensile strained steel must contribute to strengthening of maraging steel. As shown in Fig 5. 8b, a number of ribbons were formed in precipitates, marked by circles. In the high resolution TEM micrographs of precipitates 1, 2 and 3 (Figs. 5.8c-8e), it can be seen that some ribbons in the precipitates were straight and parallel (Fig 5. 8c), and others consisted of combined lines (Fig 5. 8d and 8e). In metals and alloys with low stacking fault energy, cross slip usually occurs when the dislocations pile-up at obstacles such that the internal stress increases to a level that dislocations escape from their locked positions at obstacles to change glide planes. Consequently, a full dislocation is dissociated into several partials (mostly Shockley partials) and continues to move until it is stopped by obstacles such as nanoprecipitates [151]. This means that an interaction between a full dislocation and the nanoprecipitate leaves a stacking fault in the interior of the precipitate. Thus, the stacking fault ribbon was formed, which impeded the mobility of the dislocations once the dynamic stress vanished. In Fig 5. 8c-8e, one ribbon marked by red arrow means a Shockley partial or a stacking fault derived from the dissociation of a full dislocation

stopped by the precipitate. In bcc structure, a full dislocation dissociates according to the following equation [150,151]:

$$\frac{a}{2}[110] \rightarrow \frac{a}{8}[110] + \frac{a}{4}[112] + \frac{a}{8}[110] \qquad (5.4)$$

These three partials are partially or completely retained in the particle when the dislocation cuts across or by-passes the precipitate. The straight ribbon means that only one partial possibly remained (Fig 5. 8c), and the ribbon in Fig 5. 8d indicated two partials such as $\frac{a}{8}[110]$, $\frac{a}{4}[112]$ that were retained in the precipitate. When three partials remained, the ribbon retained the full dissociation, as shown schematically in the inset in Fig 5. 8e. Generally, the stacking fault ribbon forms between the partials and makes cross-slip difficult because the stacking fault must be eliminated for dislocation slip to occur [152,153]. Thus, gliding dislocations were confined to a thin slip band forming a large pile-up against an obstacle, i.e., at a martensite lath boundary, as observed in Fig 5. 5. Progressive formation of stacking fault ribbons during deformation leads to a large pile-up of dislocations that builds a large long range of back stress and consequently produces a high strain-hardening rate for maraging steel.

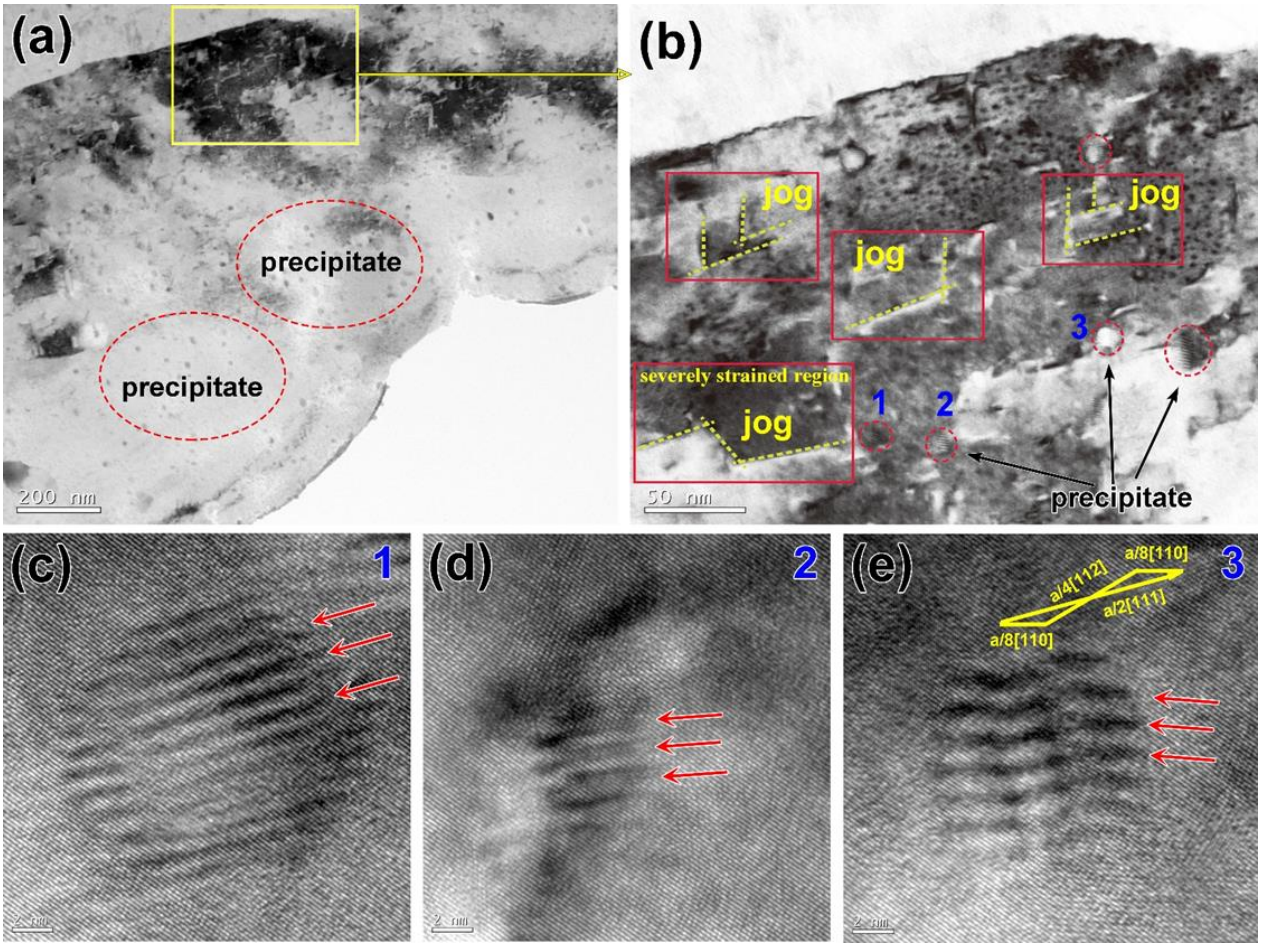

Figure 5. 8(a) TEM morphology of lath martensite and precipitates, (b) high magnification of rectangular box area in (a) and (c-e) high resolution TEM micrographs of precipitates 1, 2 and 3 in (b).

The plastic deformation of cobalt-free ultrahigh strength maraging steel must involve more number of slip systems considering the high elongation. Thus, besides the above deformation mechanism nanoscale twins were observed (Fig 5. 9). Twins were present individually or as clusters at the martensite lath boundaries or near the high density of pile-up of dislocations. They had an obvious preferred orientation (Fig 5. 9a-9c). Fig 5. 9d is a high resolution TEM micrographs of twins. Nanoscale twin had a thickness of a few nanometers (~3-4 nm). The twin plane was {112}, as indexed by the selected area electron diffraction pattern in the inset of Fig 5. 9d. Another

important aspect was that twins in the martensite lath were generally parallel (Fig 5. 9a-9c), and the closely spaced parallel twins can act as barriers to inclined twins or source for further twinning. Given that the propensity of twinning transformation has a positive correlation with strain energy [154,155], thus, on continued tensile deformation, the increase of strain energy increases the propensity to twinning. Thus, twinning also contributed to the ductility and toughness of maraging steel.

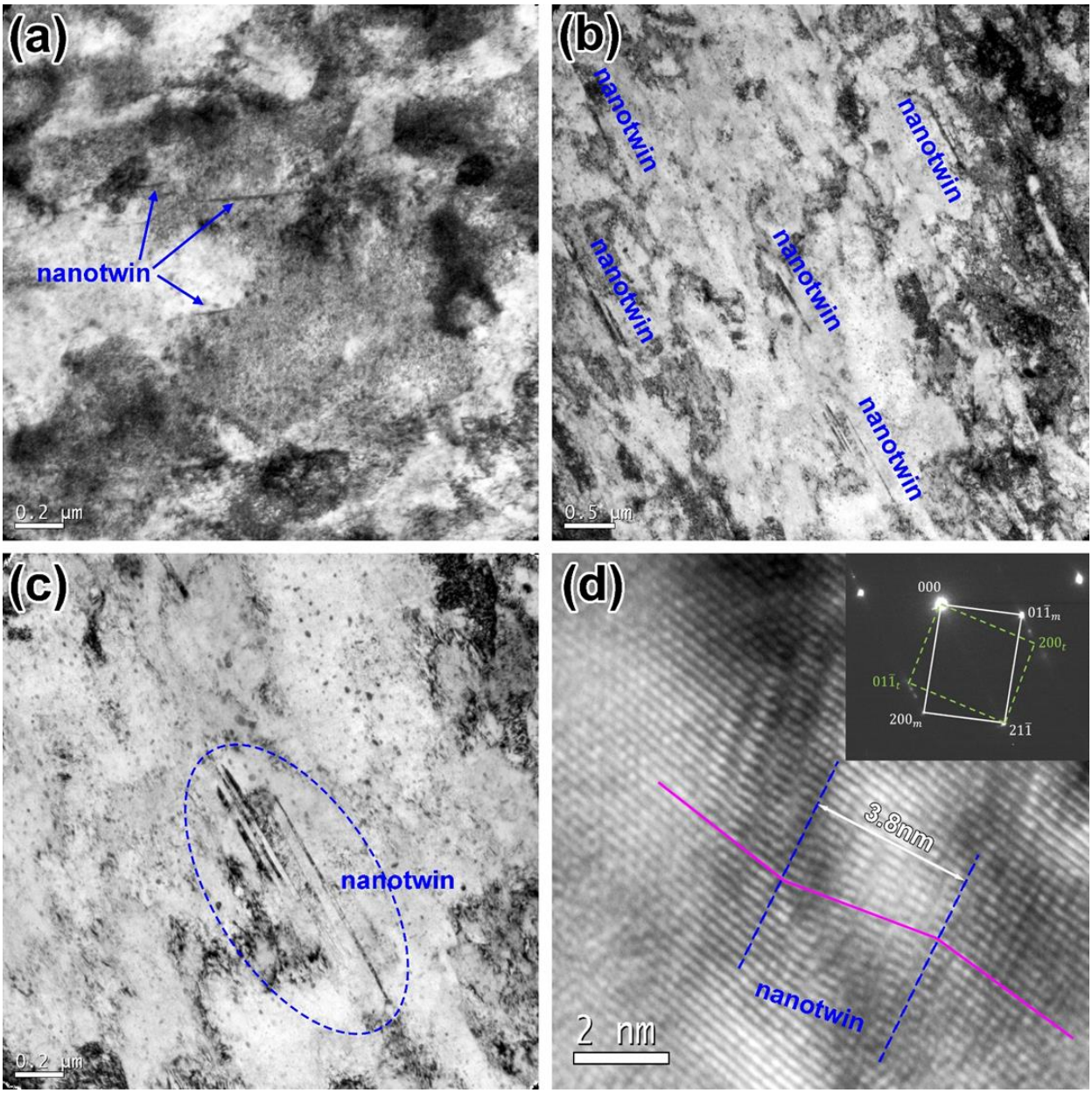

Figure 5. 9 (a-c) Micrographs of nanoscale twins in different areas near the fracture tip and (d) high resolution TEM micrograph of nanotwin and the corresponding selected area electron diffraction pattern.

5.4 CONCLUSIONS

We elucidate here the deformation mechanisms that contributed to high ductility in solution annealed and aged cobalt-free maraging steel with ultimate tensile strength of 1860 MPa, elongation of 10% and static toughness of 112.5 $MJ \cdot m^{-3}$ and comprised of high density (2.3×10^{24} m^{-3}) of η-Ni_3(Ti,Mo) and B2-Ni(Mo,Fe) nanoscale precipitates with lattice misfit of less than 1% with the martensite matrix.

Multiple deformation processes occurred during tensile deformation. There was a dramatic change in the morphology of lath martensite from straight lath-type to segmented and wavy-type morphology with angles of 30°, 60° or 120°, involving pile-up of dislocations at wavy-lath boundaries because of easy slip on habit planes $(110)_\alpha$, $(101)_\alpha$, $(01\overline{1})_\alpha$, $(12\overline{1})_\alpha$ and $(211)_\alpha$. The wavy morphology of martensite is attributed to progressive formation of jogs and kinks across the martensite lath via easy glide planes to form wavy morphology. The interactive mobility of edge and screw dislocations along the martensite habit planes was the intrinsic reason for the deformation of martensite lath.

Some low lattice misfit precipitates interacted with dislocations left a stacking fault within the precipitate such that stacking fault ribbons were formed, with retention of either one, two or three partials. The progressive formation of stacking fault ribbons during deformation led to pile-up of dislocations.

Nanoscale twinning also contributed to the deformation of maraging steel. Twins were present individually or as clusters at the martensite lath boundaries or in the vicinity of pile-up of dislocations. Twinning delayed the fracture of maraging steel.

The high ductility of ultrahigh strength cobalt-free maraging steel is attributed to cumulative contribution of glide of dislocations on habit planes that transformed the morphology

of lath-type martensite, progressive formation of jogs and kinks across the martensite lath, stacking fault and twinning. The above contributions to ductility are in addition to the significantly reduced elastic interaction between the low lattice misfit nanoscale precipitates and dislocations that reduces the ability for crack initiation at the particle-matrix interface.

5.5 SUMMARY

In this chapter we elucidate here the deformation mechanism of cobalt free maraging steel is involved multiple deformation processes such as precipitates-dislocation interaction, dislocation- martensite lath interaction. The high ductility of ultrahigh strength cobalt-free maraging steel is attributed to cumulative contribution of glide of dislocations on habit planes that transformed the morphology of lath-type martensite, progressive formation of jogs and kinks across the martensite lath, stacking fault and twinning.

Chapter 6 Study on the morphology of reverted austenite

6.1 INTRODUCTION

In previous chapter when we investigate aging parameters, reverted austenite was observed in the martensitic matrix on aging at high temperature. The reversion of martensite (α') to austenite (γ) is an important constituent that is believed to control the final structure and influence the mechanical properties. The effect of reverted austenite on mechanical properties continues to be unclear [9-11]. A few studies proposed that the reverted austenite is supposed to be harmful to toughness because of its inconsistent deformation with the matrix [9,10,12]. While others suggested that the reverted austenite is beneficial to fracture, fatigue resistance and stress corrosion cracking resistance, resulting from significantly reduced diffusion of hydrogen and crack blunting effect [11,13,14]. However, the content and morphology of reverted austenite is expected to govern the ultimate mechanical properties of maraging steel [15-22].

It is envisaged that the formation of reverted austenite strongly depends on the initial microstructure and heat-treatment temperature that determine the dynamics of transformation from martensite to austenite. In the study described here, we have used a combination of electron back-scattered diffraction (EBSD) and scanning electron microscopy (SEM), to explore the microstructural evolution of reverted austenite in cobalt-free maraging steel and elucidate the formation behavior of different morphologies at different heat-treatment temperature and time, to understand the formation mechanism of reverted austenite and its effect on mechanical properties.

6.2 EXPERIMENTAL DETAIL

Samples for microstructural analysis were cut from the aged plates and metallographically polished. They were etched with 3% nital regent (3 ml HNO3 + 97 ml C2H5OH) to observe morphology by SEM (Hitachi S-4800 field emission scanning electron microscope) operated at 15 kV. EBSD observations were carried out (TSL OIM Analysis 7) at an acceleration voltage and step size of 20 kV and 100 nm, respectively, after electro-polishing in a solution of 10% perchloric acid and 90% ethanol at a voltage of 25 V.

6.3 RESULTS AND DISCUSSION

Fig. 6.1 and Fig. 6.2 are the initial microstructure and martensite orientation map, respectively, of solution annealed (820 °C) parent maraging steel as imaged by optical microscopy and EBSD analysis. Lath martensite was observed within prior austenite grains of average size ~70 μm (Fig. 6.1). The prior austenite grain was separated by several martensite packets and each packet was further divided by elongated blocks that consisted of several martensite laths, as shown in Fig. 6.2.

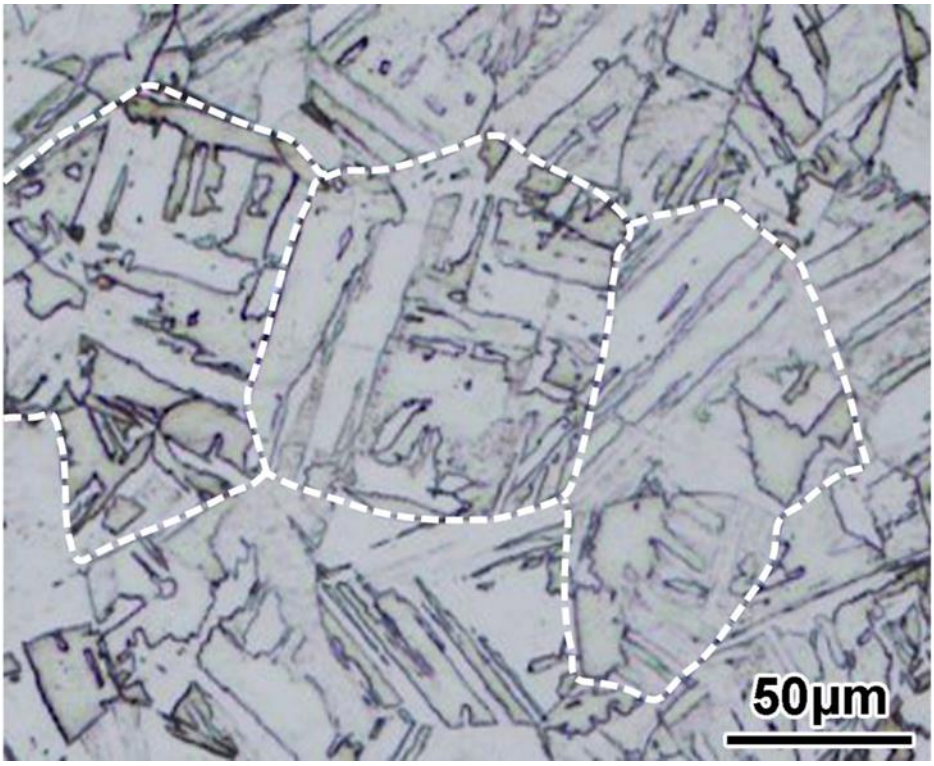

Figure 6. 1 Light micrograph of solution annealed parent steel.

Figure 6. 2 Martensite orientation map of solution annealed parent steel.

The representative microstructural evolution in maraging steel after different heat treatments is shown in Fig. 6.3. With the increase of aging temperature and holding time, three types of reverted austenite were observed. At low aging temperature (560 °C) and short holding time (60 s), granular reverted austenite (referred as γG1) was nucleated at grain/sub-grain boundaries and grew as rod-like along the prior austenite grain boundaries and block boundaries of martensite, as shown in Fig. 6.3a. When the aging time was prolonged to 1 h, besides γG1, a second type of lamellar reverted austenite (referred as γL) was present in the martensite matrix. γL was initially nucleated at lath boundaries as fine particles in the martensite matrix (Fig. 6.3a), then grew as parallel lamellar austenite (Fig. 6.3b). When the aging temperature was increased (640 °C), γG1 grew rapidly at short holding time (Fig. 6.3c) and extended along prior grain boundaries (Fig. 6.3d). Meanwhile, the content of γL increased rapidly and grew through the entire block martensite grain (Fig. 3d). At high temperature of 700 °C, both γG1 and γL were formed even at short holding time of 600 s (Fig. 6.3e). Their content increased with the increase of holding time. Next, they extended and merged to form globular reverted austenite (referred as γG2) inside original martensite grains (Fig. 6.3f). The content of γG2 increased with holding time until it reached equilibrium.

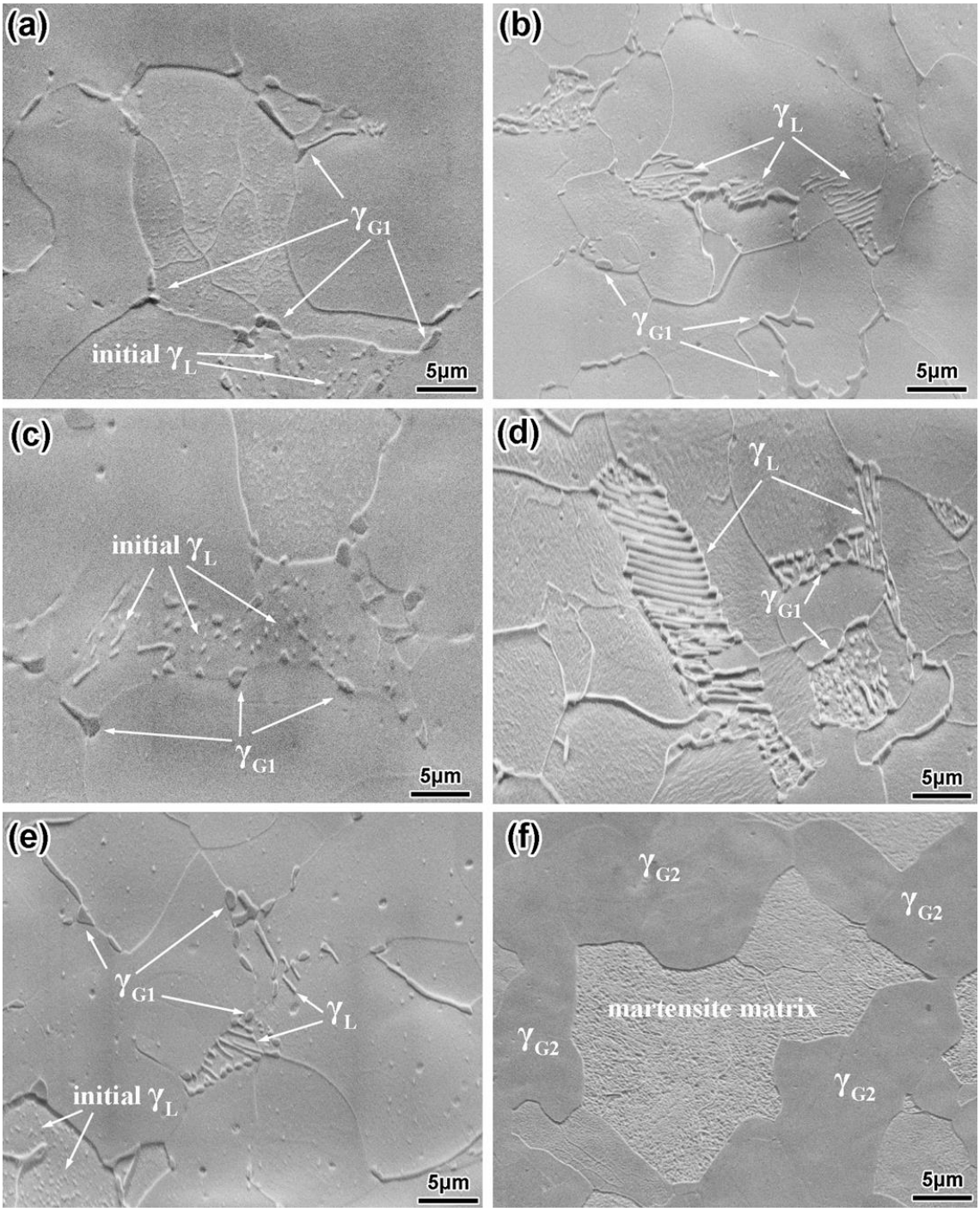

Figure 6. 3 SEM images of samples aged at different temperatures and holding times (a) 560 °C, 60 s, (b) 560 °C, 1h, (c) 640 °C, 60 s, (d) 640 °C, 1h, (e) 700 °C, 60 s and (f) 700 °C, 1 h. (γG1-granular γ, γL-lamellar γ, γG2-globular γ)

The volume fraction of the three types of reverted austenite for different aging temperatures and holding times is listed in Table 6.1, which was statistically measured by Digital Micrograph software using more than 20 SEM micrographs for each aging condition. The corresponding plot is shown in Fig. 6.4. It shows that the volume fraction of reverted austenite increased with the increase in holding time and eventually reached an equilibrium condition. At low temperature (such as 560 °C and 640 °C), there was no γG2 present in maraging steel in spite of long holding time. The volume fraction of γG1 and γL increased gradually with increased holding time at aging temperature of 560 °C and attained equilibrium volume fraction of 8.6% and 3.8% at 3 h, respectively. At higher aging temperature of 640 °C, the growth of γG1 and γL was higher when the holding time was increased, and the equilibrium volume fraction for 3 h was different. The equilibrium volume fraction of γG1 decreased from 8.6% to 6.7%, while the equilibrium volume fraction of γL increased significantly from 3.8% to 9.4% (Table 6.1). When the aging temperature was 700 °C, the initial volume fraction of γG1 and γL was higher, with presumably high growth rate. The γG2 was absent at low holding time of 6 s and 60 s. However, γG1 and γL decreased and converted to γG2 with the holding time of 600 s (Table 6.1). At equilibrium condition, γG1 and γL totally disappeared, while the volume fraction of γG2 was increased to 39.6%.

Table 6. 1 The volume fraction of reverted austenite at different aging conditions

Time	Temperature /γ fraction (%)								
	560 °C			640 °C			700 °C		
	$f_{\gamma G1}$	$f_{\gamma L}$	$f_{\gamma G2}$	$f_{\gamma G1}$	$f_{\gamma L}$	$f_{\gamma G2}$	$f_{\gamma G1}$	$f_{\gamma L}$	$f_{\gamma G2}$
6 s	0.2	0	--	0.8	0.2	--	1.6	1.4	--
60 s	1.8	0.6	--	2.5	1.3	--	3.8	2.6	--
600 s	2.7	1.2	--	3.4	3.3	--	2.7	2.4	15.5
1 h	4.6	2.4	--	4.8	5.8	--	0.9	1.3	33.8
3 h	8.6	3.8	--	6.7	9.4	--	--	--	39.6

Note: $f_{\gamma G1}$ – volume fraction of granular reverted austenite, $f_{\gamma L}$ - volume fraction of lamellar reverted austenite, $f_{\gamma G2}$ - volume fraction of globular reverted austenite.

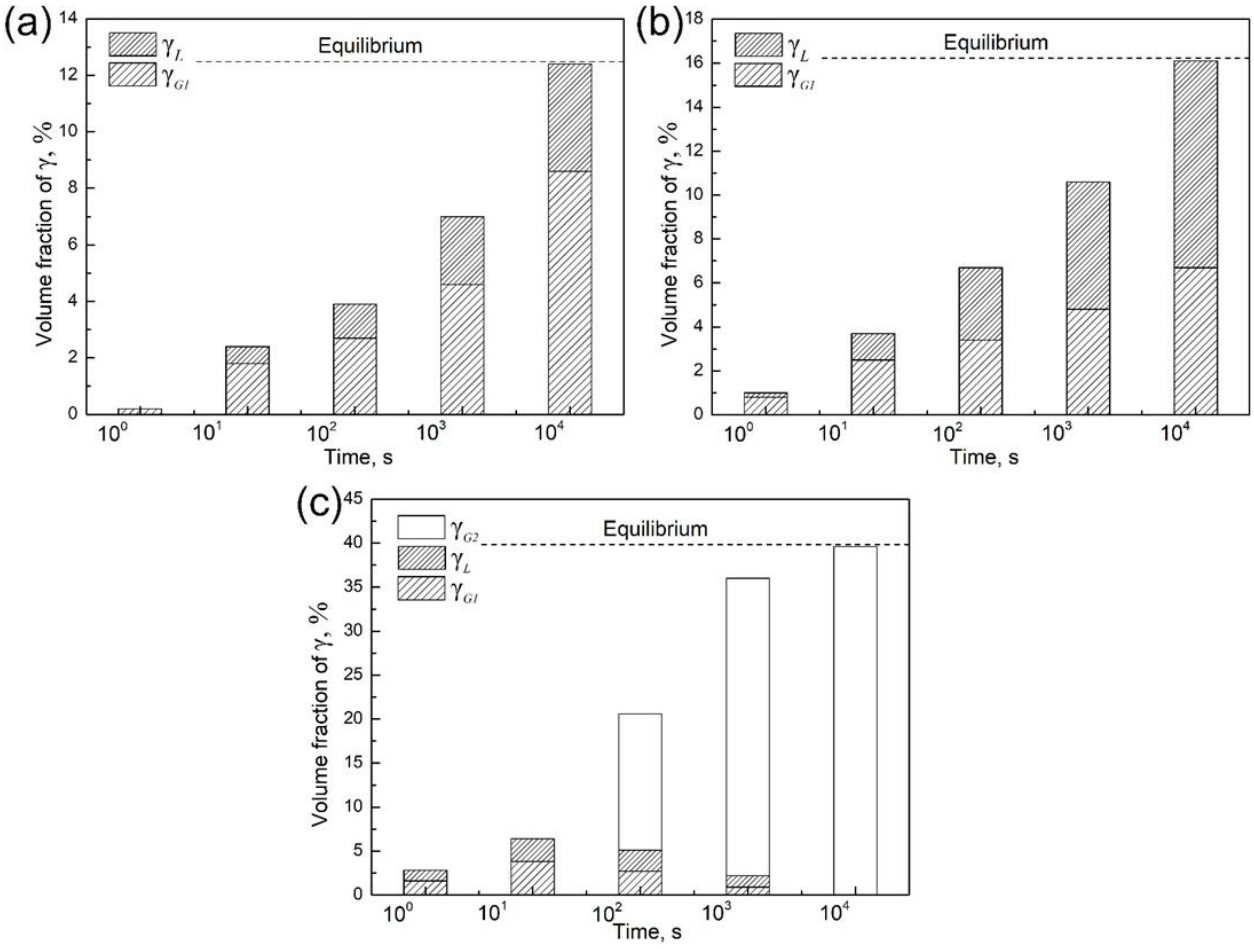

Figure 6. 4 Volume fraction of reverted austenite at different aging conditions (a) 560 °C, (b) 640 °C and (c) 700 °C

In summary, there was a significant difference in the morphology of reverted austenite at different aging temperatures and holding time. This is a result of competition between the nucleation rate of reverted austenite and its growth rate. Fig. 6.5 shows a schematic diagram of reverted austenite evolution as a function of aging temperature and time. It can be seen that at low aging temperature (560 °C) and short holding time (60 s), only γG1 occurs along the prior-austenite grain boundaries. With the increase of aging temperature (600 °C) and holding time (600 s), γG1 also begins to form along martensite packet/sub-grain boundaries. Then the initial γL forms in the martensite block and grows with the increase of holding time. At these stages, the nucleation rate of reverted austenite is lower than the growth rate. Hence it forms different morphologies, namely, γG1 and γL, and grows rapidly with different orientations. While at the high temperature (700 °C) and long holding time (3 h), the nucleation rate of reverted austenite is significantly higher than the growth rate at high temperature, such that γG1 and γL convert together to γG2 before they grow with different morphologies, as shown in the last stage of Fig. 6.5.

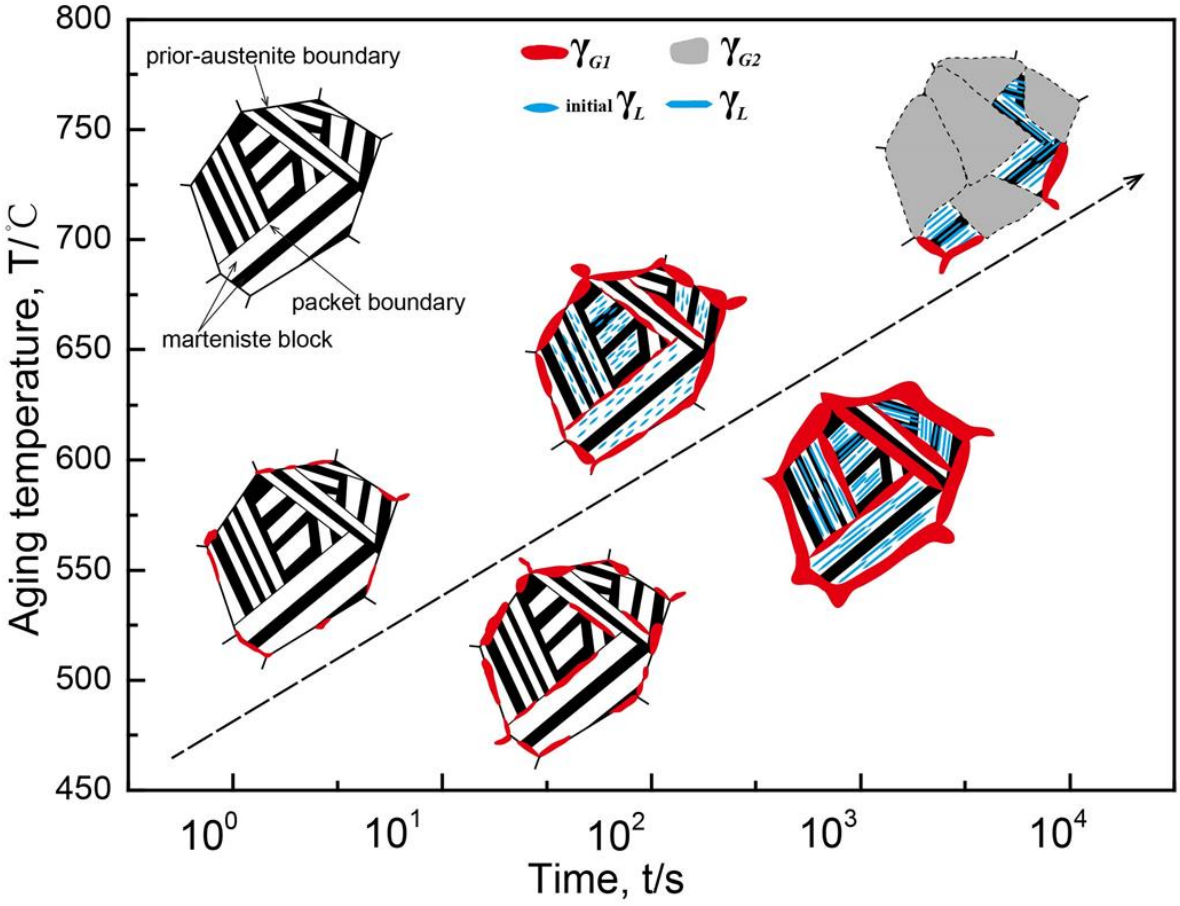

Figure 6. 5 Schematic diagram of reverted austenite evolution with the increase of aging temperature and holding time.

In order to further elucidate the impact of formation behavior of different morphology of reverted austenite at different aging conditions, texture and Schmid factor were analyzed, as shown in Fig. 6.6. It can be seen that at low aging temperature, the matrix had a strong texture (Fig. 6.6a1). With the increase of aging temperature, the texture of matrix became weak (Fig. 6.6a1-6c1), because of increased transformation from martensite to reverted austenite. The Schmid factor images show that more and more grains tend to have a Schmid factor value of 0.5 with the increase of aging temperature (Fig. 6.6a2-6c2). This implies that the material can be easily deformed, which

is beneficial to ductility and toughness. It is known that reverted austenite decreases strength and increases toughness because of its intrinsic soft phase compared with martensite. However, γG1 at grain boundaries corresponds to diffusional transformation and has low density of dislocations. While γL in the matrix corresponds to shear diffusionless transformation and inherits high density of dislocations and K-S orientation relationship with the matrix [23]. The presence of γG1 at grain boundaries is harmful to toughness and γL in the matrix is beneficial to toughness in maraging steel and was discussed by us in our recent studies [8,18,23]. As regards γG2, it was converted from γG1 and γL as a large grain size, which exhibited soft feature of austenite. Thus, we underscore that it is important to consider the different morphology of reverted austenite when discussing the mechanical behavior.

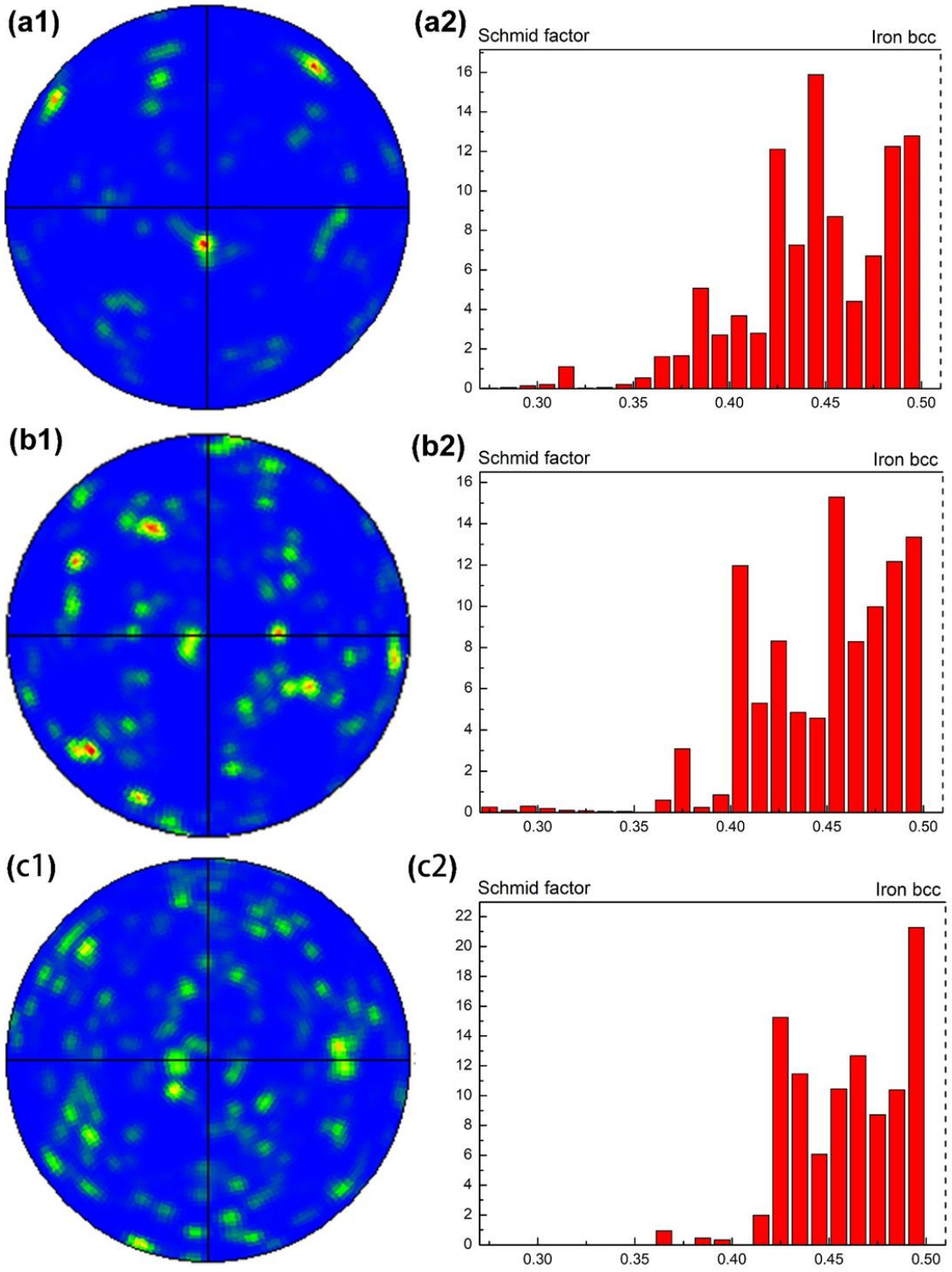

Figure 6. 6. 001α pole figures and Schmid factors of matrix with (a) 560 °C, 1 h, (b) 640 °C, 1 h and (c) 700 °C, 1 h.

6.4 CONCLUSIONS

Three types of reverted austenite were obtained in maraging steel depending on aging temperature and holding time: granular reverted austenite at grain boundaries (γ_{G1}), lamellar reverted austenite in the Fe-Ni matrix (γ_L) and globular reverted austenite (γ_{G2}) inside the entire martensite grain.

At low temperatures (560 °C and 640 °C), only γ_{G1} and γ_L were observed in maraging steel, irrespective of the holding time. The volume fraction of γ_{G1} and γ_L increased with the increase of aging temperature and holding time. While at high temperature (700 °C), γ_{G2} was absent at short holding time, and γ_{G1} and γ_L decreased with the increase of holding time such that they were converted to γ_{G2} at 3 h to equilibrium condition.

The nucleation rate of reverted austenite was envisaged to be lower than the growth rate at low temperature. The reverted austenite formed into different morphologies as γ_{G1} and γ_L, and grew rapidly with different orientations. While based on the morphological observation, the nucleation rate of reverted austenite was significantly higher than the growth rate at high temperature, such that γ_{G1} and γ_L converted to γ_{G2}.

The weak texture of maraging steel with high Schmid factor at high aging temperature implied that γ_L and γ_{G2} are the likely reasons for the previously observed superior toughness and ductility.

We underscore that it is important to consider and control the morphology and content of reverted austenite, besides other microstructural features to optimize the mechanical behavior.

6.5 SUMMARY

We elucidate here the microstructural evolution and formation of reverted austenite in cobalt-free maraging steel. Three types of reverted austenite, granular reverted austenite at grain

boundaries (γ_{G1}), lamellar reverted austenite in the matrix (γ_L) and globular reverted austenite (γ_{G2}) were observed in maraging steel, depending on the aging temperature and time. At low temperatures (560 °C and 640 °C), only γ_{G1} and γ_L were observed. While at high temperature (700 °C), γ_{G1} and γ_L decreased with holding time increased and were completely transformed to γ_{G2} at equilibrium condition. The observation of three different morphologies of reverted austenite were a consequence of competition between the nucleation rate and growth rate of reverted austenite at different aging temperatures. The weak texture of maraging steel with high Schmid factor at high aging temperature implied that γ_L and γ_{G2} are the likely reasons for superior toughness and ductility. We underscored that it is important to consider and control the morphology and content of reverted austenite, besides other microstructural features when interpreting the mechanical behavior.

Chapter 7 Research of periodic distribution of alloying elements during tempering in a multistep partitioned manganese steels

7.1 INTRODUCTION

Retained austenite (RA) governs strength-ductility combination in the third generation advanced high strength steels (AHSS) [40,172-175]. The stability and volume fraction are both important for uniform elongation and tensile strength [176], while high stability is critical for high fracture toughness [177]. Optimizing the presence of alloying elements in steel is important to control the volume fraction and the stability of RA [176, 178]. It is, however, important to consider the cost and any difficulty that may be experienced during processing, while tuning the volume fraction and stability.

Medium-Mn steels adopt intercritical annealing to stabilize retained austenite via diffusion of C and Mn into austenite [176]. But longer annealing time leads to a significant loss in strength because of low alloying content and recovery of dislocation. Quenching & partitioning (Q&P) heat treatment provides high strength martensite matrix and RA enriched with carbon [179]. However, there is a competitive relationship between diffusion of carbon to RA and nucleation of carbides during the partitioning process [180, 181]. High Si (~1.8 wt.%) content is important for Q&P steels, which is effective in preventing the formation of carbides and ensures stabilization of RA by carbon [182]. Al has as effect as similar to Si in retarding the precipitation of carbides [183, 184]. But high content of Al and Si pose a problem. For example, Al added to molten iron increases the risk of ladle nozzle blockage [185], while Si influences temper brittleness of medium-carbon steel [186]. Thus, there are restrictions on the addition of Si and Al in minimizing the formation of carbides or decomposition of RA [187].

7.2 EXPERIMENTAL DETAIL

The nominal chemical composition of experimental steel was Fe-0.22C-4.88Mn-1.59Al. Mn is the primary alloying element in the experimental steel. The reason for higher carbon content as compared to our recent study on MSP [188] is to study the effect of carbon on tempering in MSP steel. Al was added to inhibit the formation of cementite. Steel was melted in vacuum and cast into ingots of ~80 mm thickness. The ingots were homogenized at 1200ºC for 2 h, and hot rolled to 12 mm thick strip using several passes with minimum reduction of 20% per pass.

The Ac_1 and Ac_3 temperature for the experimental steel were determined by Thermol-Calc, Ac_3=860 ºC Ac_1= 575 ºC. Higher austenization temperature was used to obtain large martensite lath. Heat treatment details are listed in Table 1. Lower flash temperature was used to control austenization and partitioning of alloying elements. The experimental samples are referred based on tempering time (15 min, 30 min, 1 h and 2 h) at 300ºC, which was used to study the microstructural evolution of general quenched (Q) and multi-step partitioning (MSP) quenched steels.

The general quenching tempering (QT) process consisted of austenization at 960ºC for 30 min and water quenched, followed by tempering at 300ºC for 30 min. The multistep partitioning process (MSP) involved austenization at 960 ºC for 30 min and water-quenched (Q), intercritical annealing at 650 ºC for 6 h and quenching in water (L), reheating to 900ºC (at heating rate of 10ºC/s) and then water-quenched (Q) (referred as flashing process-F), and last step of tempering at 300ºC for 30 min, followed by cooling in air (T). The reasoning for these steps in the MSP process are the following: Austenization and quenching provides a predominately martensite lath matrix, intercritical annealing enriches retained austenite with C and Mn, while annealed martensite or ferrite is depleted in C and Mn. The aim of flashing process is to obtain martensite

and retained austenite during austenitization, and on flash cooling martensite transformation occurs. It may be noted that during the small duration of the flash process, Mn is enriched in retained austenite and bestows stability to austenite, while C diffuses from austenite to the depleted martensite region, increasing strength [188].

The primary objective of tempering is to enrich retained austenite once again with C and relax the internal stress in the matrix. In summary, the MSP process involved the following characteristics: (a) enrichment of retained austenite with C and Mn, (b) diffusion of C to the depleted annealed martensite, (c) second time enrichment of retained austenite with C. Considering the higher solubility of Al in BCC-Fe in relation to FCC-Fe, the diffusion of Al is opposite to that of Mn and C.

Table 7. 1 Heat treatment of samples conventional quenching and tempering (QT) and multistep partitioning-quenching and tempering (MSP-QT)

Samples	Heat treatment
Q	960^{o}C/30 min quenched in water (Q)
QT	Q + 300^{o}C/30 min cooling in air (T)
MSP-Q	Q + 650^{o}C/6 h cooling in air (intercritical annealing: L) + 1900^{o}C/6s cooling in water (flashing: F)
MSP-QT	QLF + 300^{o}C/30 min cooling in air (T)

Q: quenching; T: tempering; L: intercritical annealing step in multi-step partitioning (MSP) process; F: flashing in MSP process.

Tensile samples were machined parallel to the rolling direction according to the ASTM standard, and tested at room temperature using WE-300 uniaxial tensile test machine. Volume

fraction of austenite was determined by X-ray diffractometer (XRD) using Cu-Kα radiation. The volume fraction of austenite (VA) was calculated using equation [183]:

$$VA = 1.4I\gamma \; / \; \left(I\alpha + 1.4I\gamma\right) \tag{7.1}$$

where Iγ is the integrated intensity of austenite (200)γ, (220)γ and (311)γ peaks and Iα is the integrated intensity of (200)α and (211)α peaks.

Scanning electron microscopy (SEM) was carried out after mechanical polishing and etching with 3% nital to observe the microstructure. Transmission electron microscopy (TEM) was carried out using thin foils that were prepared by cutting thin slices from the steel samples and grinding to ~50 μm in thickness. 3 mm in diameter foils were punched and electropolished using 10% perchloric acid in ethanol.

7.3 RESULTS AND DISCUSSION

7.3.1 Mechanical properties

Mechanical properties and engineering stress-strain plots are presented in Fig. 7.1. High strength and low elongation were obtained after quenching (ultimate tensile strength (UTS) 1564 MPa, yield strength (YS) 1070 MPa, uniform elongation (Eu) 5.0% and total elongation (Et) 10.5%). After tempering at 300 ºC for 30 min, the UTS decreased to 1381 MPa and Et slightly decreased to 9.5%, while, YS and Eu were similar to the quenched steel.

Steel MSP-Q had relatively lower strength than steel Q, (YS 493 MPa, TS 1125 MPa), but the elongation was significantly greater than steel Q (Eu 17.4% and Et 20.9%). The YS of steel MSP-QT increased to 694 MPa and UTS decreased to 1018 MPa, while Eu and Et of steel MSP-QT decreased to a small extent on tempering.

As presented in Fig. 7.1, high strength and low elongation were obtained after conventional quenching and tempering. But high strength and excellent elongation were obtained in the MSP-

QT process. The uniform elongation of MSP steel was ~2.5 times greater than the general quenched and tempered (QT) steels.

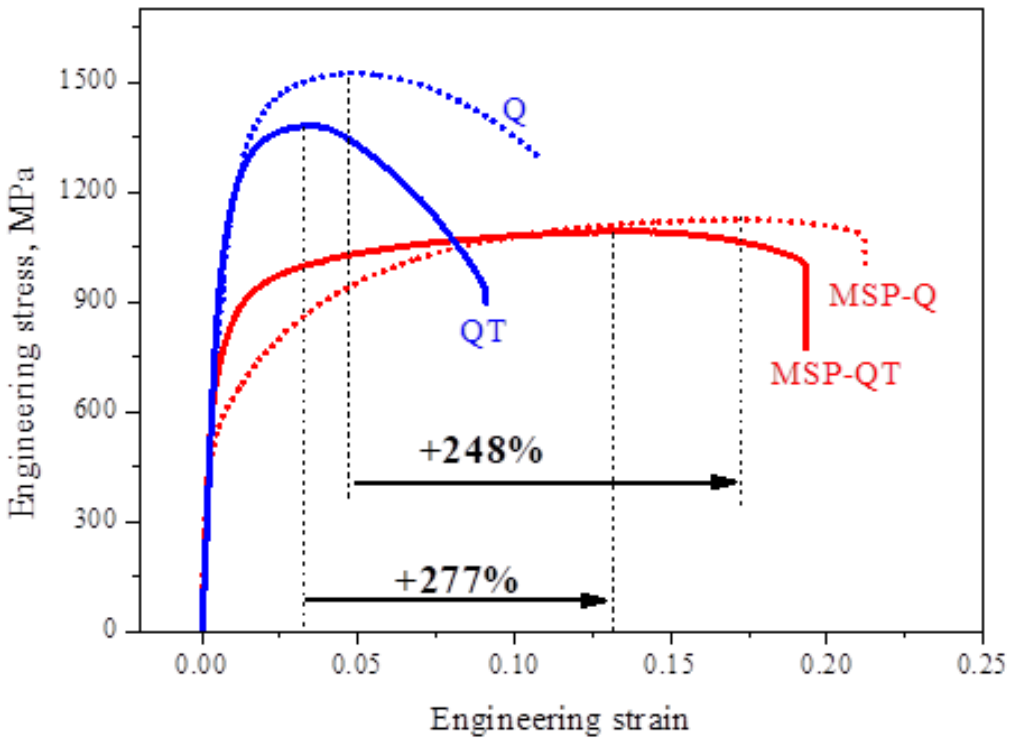

Figure 7. 1 Engineering stress-strain curves of experimental steels.

7.3.2 Microstructure

The microstructure, as imaged by SEM, is presented in Fig. 7.2. Lath-like martensite with high density of dislocations was obtained after quenching (Fig. 7.2a and 7.3a) and 3.9% retained austenite was measured by XRD (Fig. 7.4a). Carbides were noted at the lath boundary (indicated by arrow in Fig. 7.2b) and insides of martensite lath (Fig. 7.3b) in steel QT after tempering at 300ºC for 30 min. Lath-like microstructure was also observed in steel MSP-Q (Fig. 7.2c, 7.3c), together with some ferrite (white region with dislocations in Fig. 7.3c). Lath martensite (with high

density of dislocations appeared gray in Fig. 7.3c), twin martensite, ε martensite and retained austenite were present in MSP-Q. Twin martensite, ε martensite and retained austenite were present together (as dark regions in Fig. 7.3c) and was difficult to delineate in our TEM because of ultra-refine microstructure. However, they were identified by selective area diffraction of the circled region in Fig. 3c and is presented in Fig. 3e. 30.0% retained austenite was obtained in steel MSP-Q and decreased to 24.7% after tempering at 300^{o}C for 30 min. However, there were small differences in morphology between MSP-Q and MSP-QT (Fig. 7.3(c, d)). Carbides and recovery of dislocations were not observed in steel MSP-QT (Fig. 7.3d).

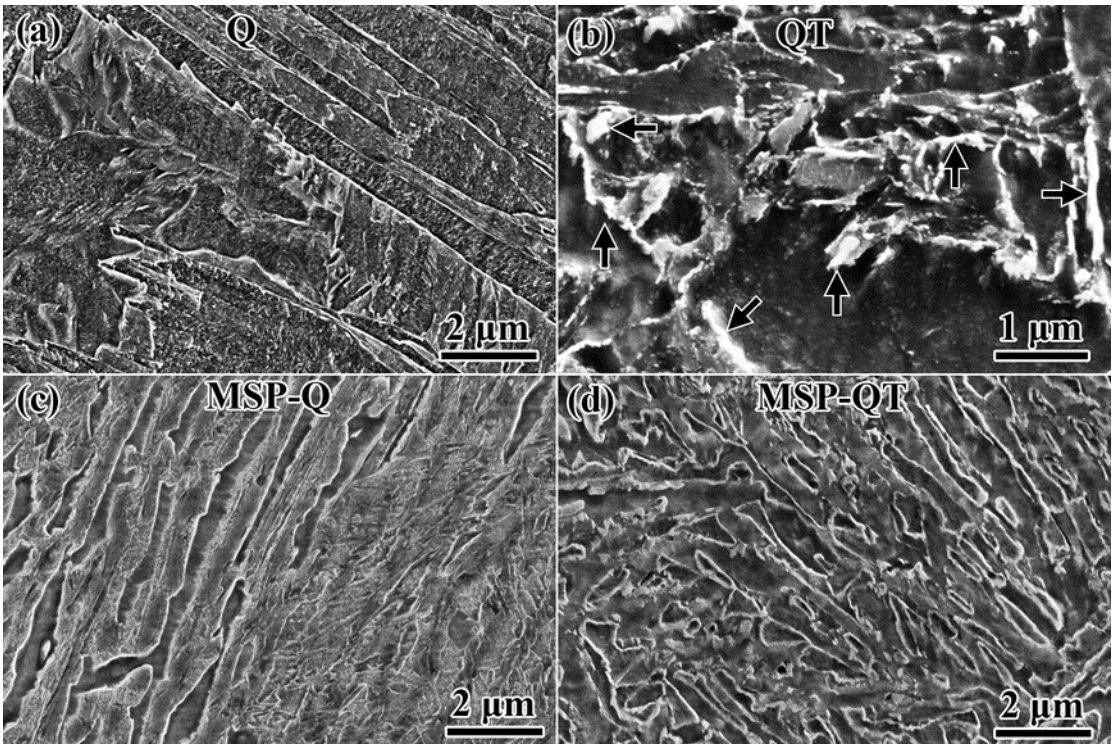

Figure 7. 2 SEM micrographs for different heat treatment conditions. (a) Q, (b) QT, (c) MSP-Q, (d) MSP-QT

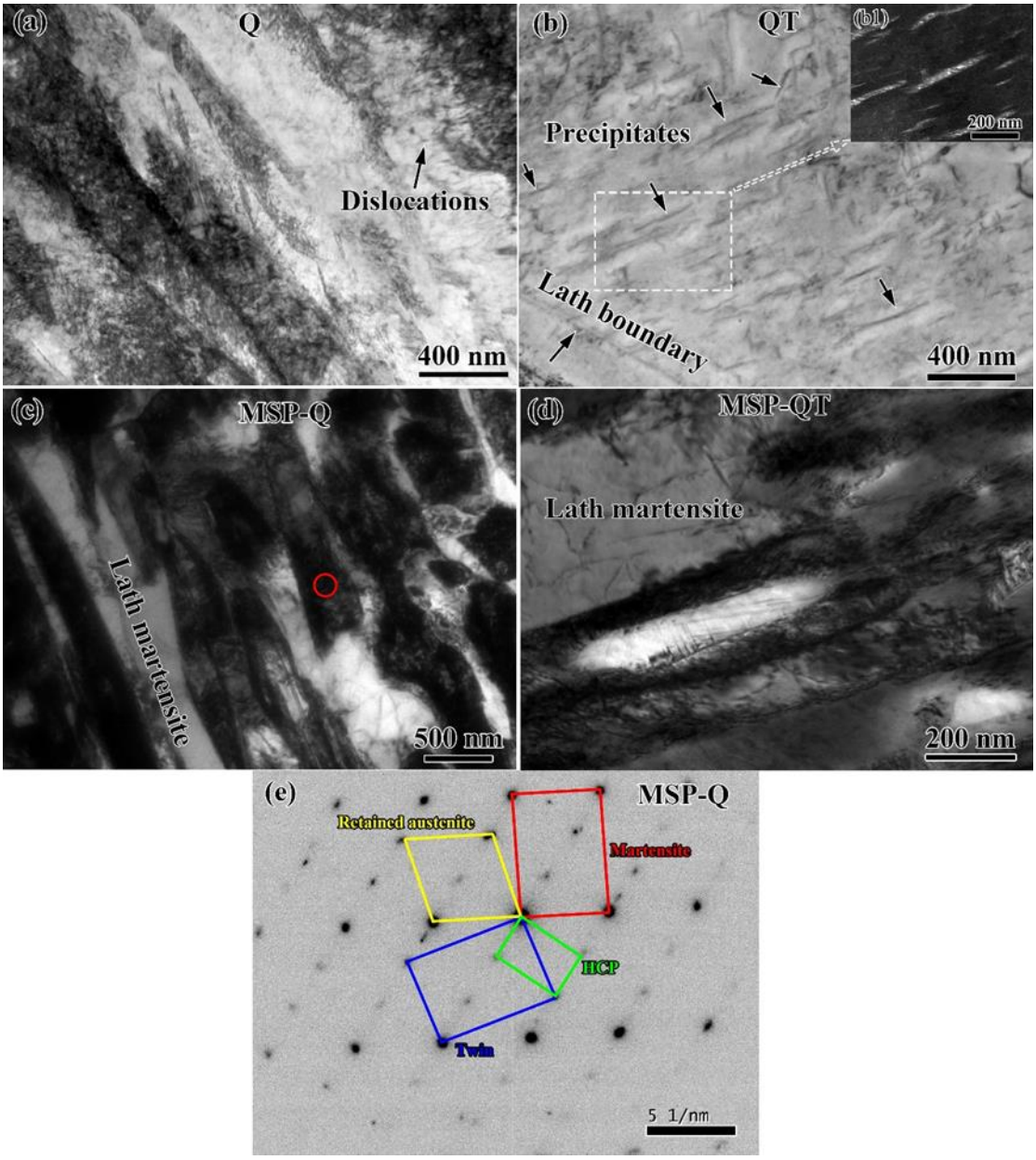

Figure 7. 3 TEM micrographs of experimental steel corresponding to different heat treatment conditions (a) steel Q, (b) steel QT, (c)steel MSP-Q, (d) steel MSP-QT and (e) select area diffraction of circle in (c), (b1) dark field images of precipitates in the marked region in (b).

7.3.3 Influence of tempering on microstructure

The remarkable difference between the two tempered steels (QT and MSP-QT) was the presence of carbides (Fig. 7.2b) in QT steel. However, insignificant change in the microstructure was observed in steel MSP-QT (Fig. 7.2(b, d)). To further study the influence of tempering on microstructural evolution, MSP-Q steel was tempered for 15 min/30 min, 1 h and 2 h and presented in Figs. 7.5 and 7.6.

Based on the XRD data (Figs. 7.4a), 3.9% retained austenite was obtained after quenching (steel Q), which decreased to near 0% after tempering at 300^{o}C for 15 min. While, ~30.0% retained austenite was obtained in steel MSP-Q, which increased to 34.8% after tempering at 300^{o}C for 15 min and decreased to 24.7%-27.0% on prolonged tempering for 30 min-2 h (Fig. 7.4b).

The microstructure of quenched and tempered steels is presented in Fig. 5. Carbides (white elongated particles in Fig. 7.5) were observed after tempering for 15 minutes at grain boundaries and inside martensite. The carbides coarsened with prolonged tempering time. In contrast, majority of retained austenite maintained lath-like morphology in MSP quenched and tempered steels after tempering at 300^{o}C for 2 h. No carbides were observed in SEM on tempering for 15 min in MSP-Q steel, and few carbides were noted in tempered martensite after tempering for 30 min. These carbides became coarse and more carbide precipitation occurred with the increase of tempering time.

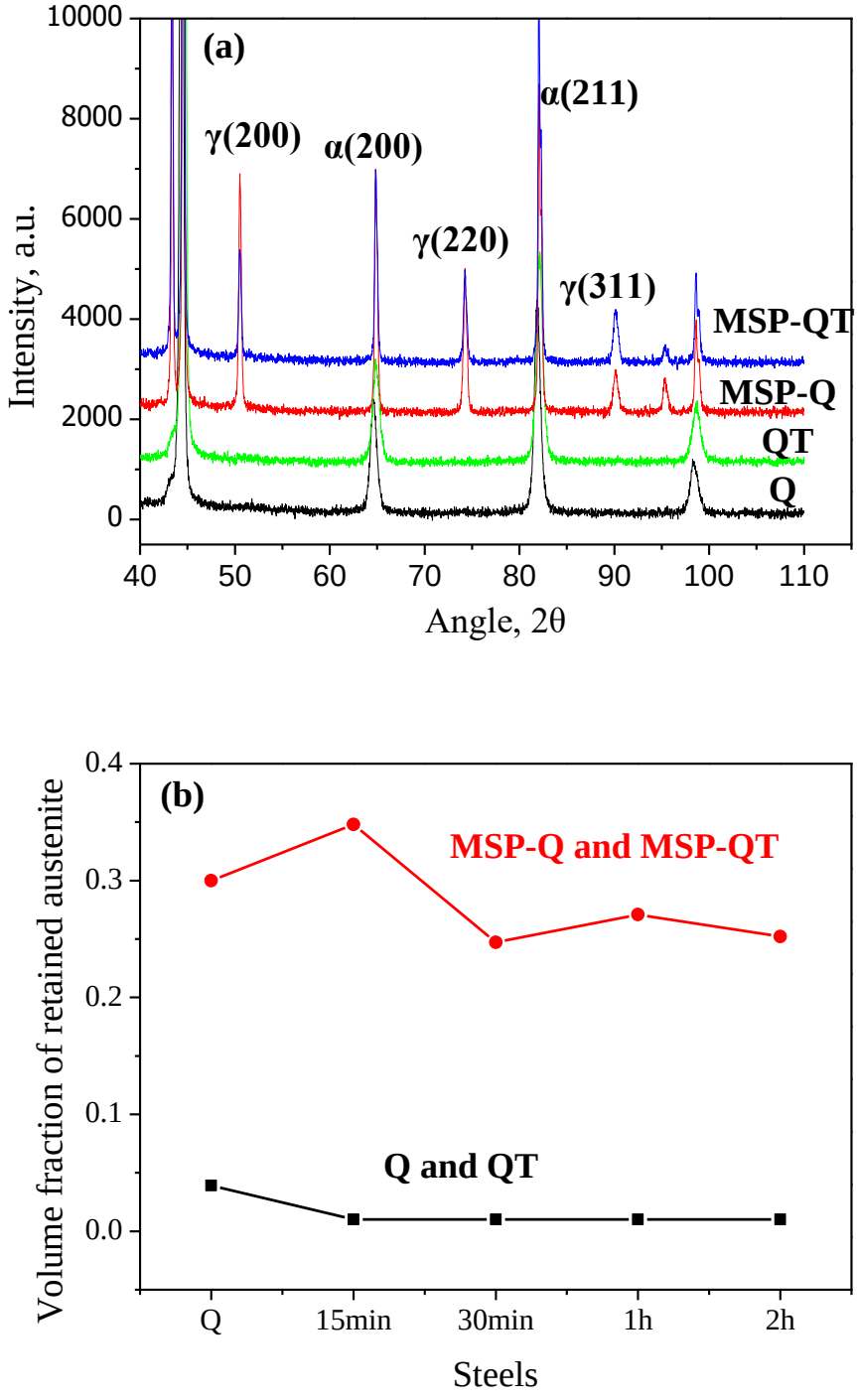

Figure 7. 4 (a) XRD curves of experimental steels and (b) volume fraction of retained austenite in experimental steels.

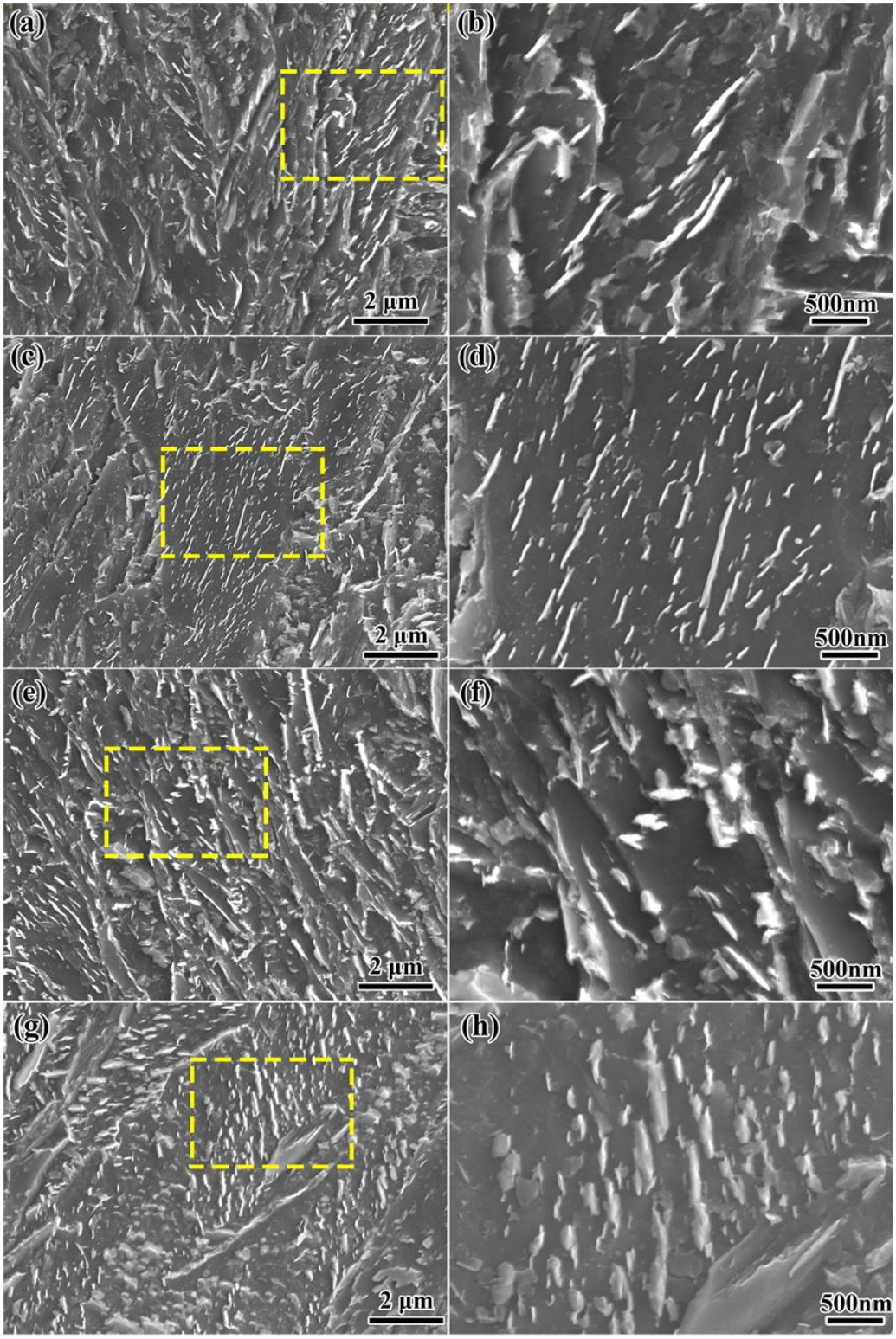

Figure 7. 5 Microstructure of conventional quenched and tempered steel with tempering time. (a, b) 15 min, (c, d) 30 min, (e, f) 1 h and (g, h) 2 h.

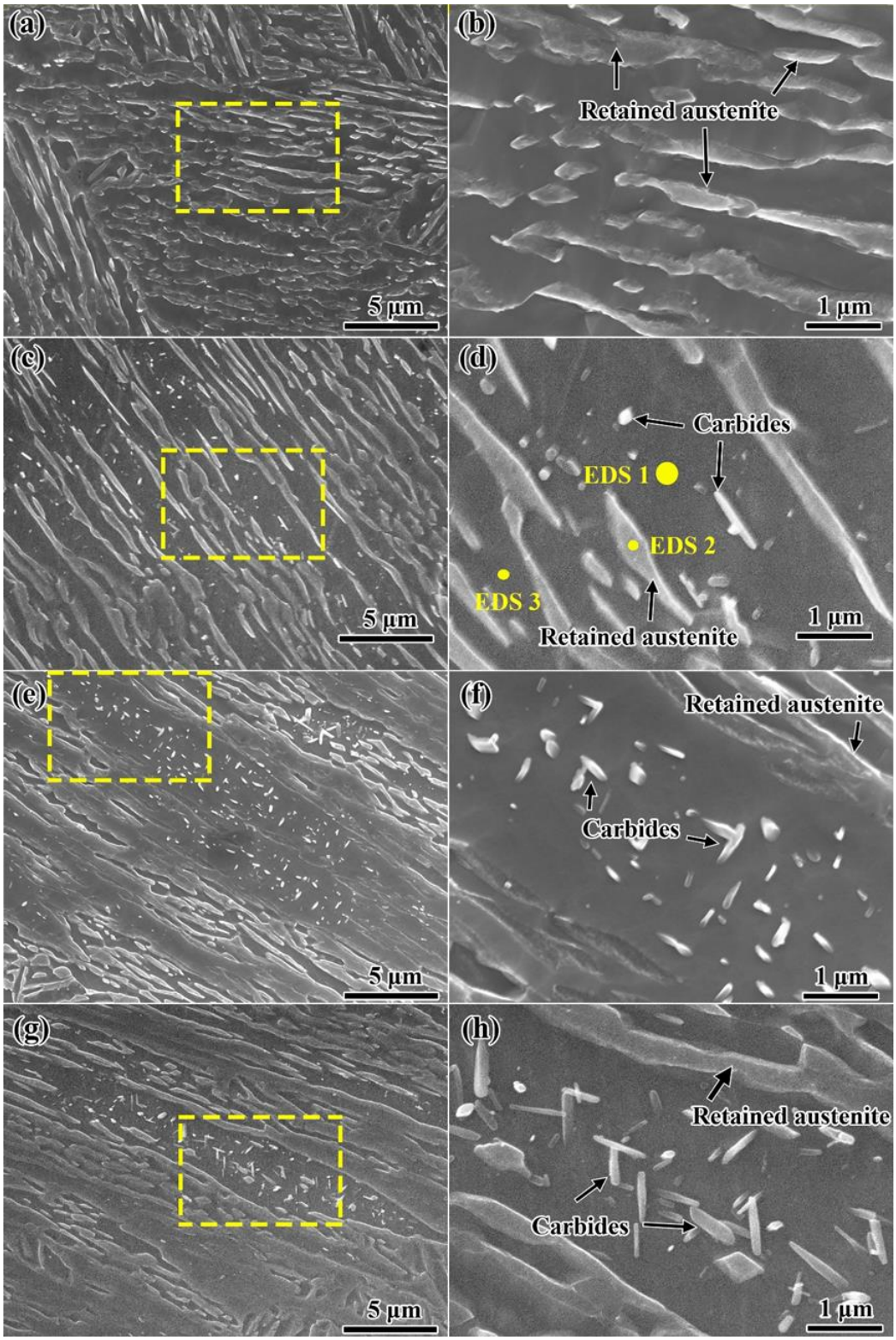

Figure 7. 6 Microstructure of MSP quenched and tempered steel with tempering time. (a, b) 15 min, (c, d) 30 min, (e, f) 1 h and (g, h) 2 h.

7.4 DISCUSSION

The major differences between QT and MSP-QT steels were carbides and retained austenite. The formation of retained austenite and retarding precipitation of carbides in MSP-Q steel is critical and is expected to have significant influence on mechanical properties, as discussed in the following paragraphs.

7.4.1 Distribution of alloying elements in the microstructure

The chemical composition of steel has a significant impact on the formation of carbides, especially when Al restricts the precipitation of carbides. A one-dimensional model (normal to the lath) of length 300 nm (from the center of austenite lath to the center of ferrite lath) was built and calculated by DICTRA to simulate the distribution of alloying elements, and the results are presented in Fig. 7.7. Austenization was not completed as predicted by DICTRA simulation, ferrite was left in the right side of model, which is consistent with the observation of ferrite (or annealed martensite) in the microstructure of steel MSP-Q in Fig. 7.3b. 2.25 wt.% Al was enriched in the ferrite region, and depleted in the center of austenite. In contrast, Mn and C were enriched in austenite but depleted in ferrite. The highest concentration of Mn in austenite was 8.06 wt.%. While Mn was periodically enriched and depleted in the microstructure of steel MSP-Q as studied by Auger electron spectroscopy (AES) (Fig. 7.7). Based on the above observations, it is believed that the distribution of alloying elements results in the formation of lath martensite and retained austenite, where the lath martensite is enriched in Al and depleted in Mn, and retained austenite is enriched in Mn and depleted in Al. The distribution of Mn and Al was maintained during tempering. The composition of local microstructure in Fig. 7.6d (EDS 1, 2 and 3) as determined by EDS, was 0.86Al-5.61Mn wt.% in retained austenite and 1.38Al-3.32Mn wt.% in the tempered martensite region.

While the local chemical composition in the precipitation region of carbides was 1.26Al-4.64Mn wt.%, which is close to the bulk composition. It is suggested that the thickness of lath varied with location, and the distribution of Mn and Al in small size lath was more uniform, because homogenization of Mn and Al can be accomplished when the diffusion distance is small. But the precipitation of carbides in these regions was similar to the conventional quenched microstructure. Carbides (Fig. 7.5) were well developed in conventional quenched steel (Fig. 7.6). Here, there was a competing affect, where small-size carbides in martensite dissolve and carbides at grain boundaries coarsen.

The competition of carbon in steel MSP-Q during tempering was between carbides and retained austenite. Considering the presence of retained austenite in steel MSP-Q, carbon was partitioned into retained austenite at the beginning of tempering and led to stabilization of retained austenite and possible growth of retained austenite, which explains the increase in the volume fraction after tempering for 15 min (Fig. 7.4). After the nucleation of carbides between retained austenite and martensite, coarsening of carbides occurred by diffusion of carbon from retained austenite to the precipitation region. It is clear that carbon diffusion is easier in retained austenite as compared to the dissolution of carbides, which can lead to coarsening of carbides.

The coarsening rate of carbides was faster in steel MSP-Q during tempering. However, ~25% retained austenite continued to be present in the matrix (Fig. 7.4). This is expected to inhibit nucleation of carbides between martensite and retained austenite. It is certain that carbides nucleated at martensite rather than at retained austenite. Al was enriched in the center of martensite and deceased at the phase boundary of martensite and retained austenite. Furthermore, minimum carbon in the martensite region after partitioning of carbon to retained austenite also restricted the nucleation of carbides. Therefore, enriched segregation of Al and depletion of carbon at the

nucleation site of carbides effectively inhibited the nucleation of carbides. Retained austenite restricted nucleation of carbides and resulted in high stability during tempering, which is beneficial in enlarging the tempering window from the perspective of application.

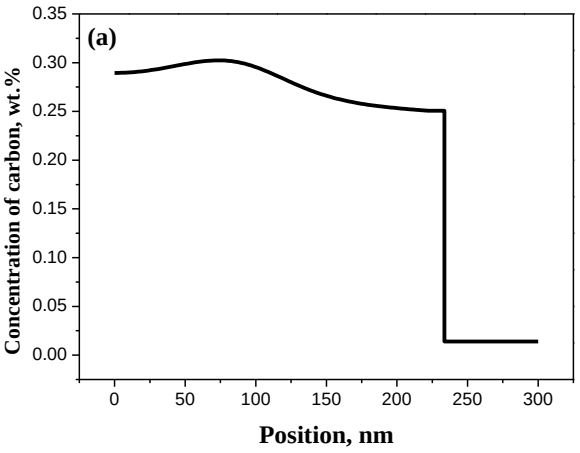

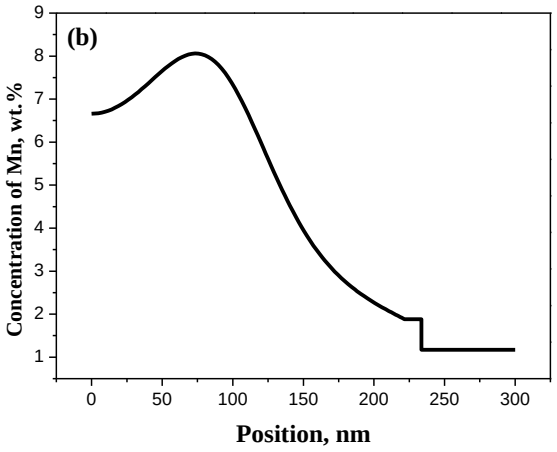

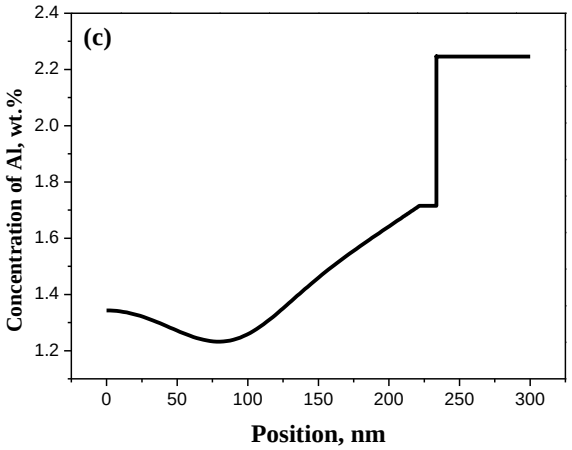

Figure 7. 7 Concentration of alloying elements as estimated from DICTRA (a) carbon, (b) Mn and (c) Al.

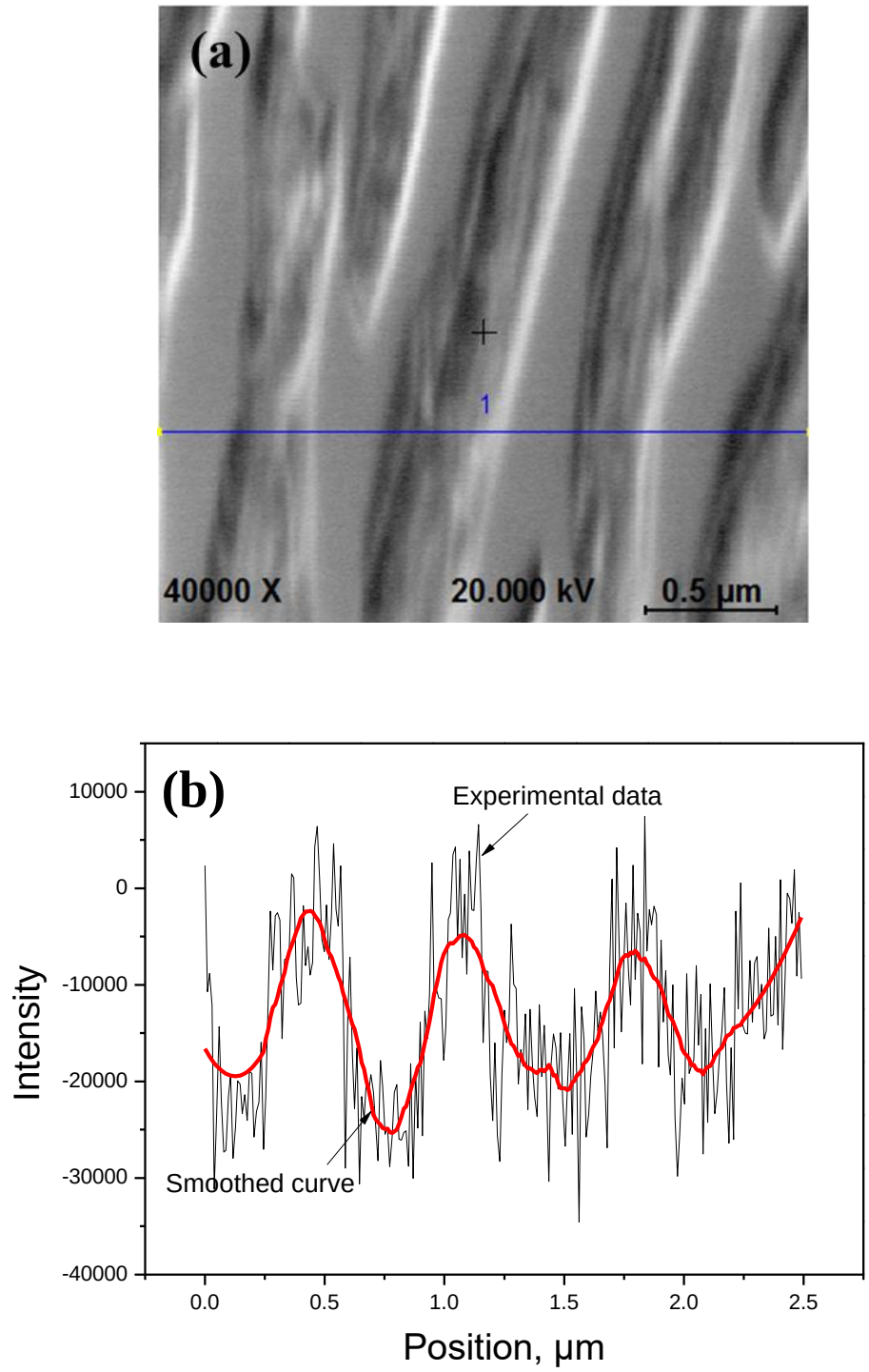

Figure 7. 8 (a) Surface morphology of electro-polished MSP-Q steel and (b) distribution of Mn along the lath structure as determined by AES.

7.4.2 TRIP effect of retained austenite

Retained austenite not only influences to the precipitation behavior of carbides, but also significantly impacts mechanical properties. In order to study the TRIP effect of retained austenite in steel MSP-QT, true strain-stress curves and work hardening index are plotted in Fig. 9. The stress–strain behavior was analyzed using Hollomon analysis and is given by Eq. (7.2) [189]:

$$\sigma = K\varepsilon^{n} \tag{7.2}$$

where σ is the true stress, ε is the true strain, K is constant, n is the work hardening index. Eq. (7.2) is represented in terms of instantaneous work hardening index (n*) by:

$$n^{*} = d\ln\sigma / d\ln\varepsilon \tag{7.3}$$

There is a significant difference between steel QT and steel MSP-QT as presented in Fig. 9. The instantaneous work hardening index of steel QT decreased rapidly with true strain to near 0, but the instantaneous work hardening index of steel MSP-QT maintained a relative lower decreasing rate to ~0.125 in stage I (Fig. 7.9) compared to steel QT and was nearly constant at ~0.125 in stage II. The high work hardening index in stage II greatly contributed to uniform elongation. However, the valley in the work hardening index [190], generally represents significant work hardening when retained austenite transforms to martensite. The low value of instantaneous work hardening index before martensite start transformation is because the stability of retained austenite is relatively high when alloying elements are enriched in austenite. While TRIP effect was present in stages I and II, but the TRIP behavior was quite different with the commonly observed effect in TRIP-aided steels, such as Q&P steel and intercritical annealed steels. The high rate of n^{*} before stage I is attributed to the initiation of dislocation movement after yielding. Subsequently, TRIP occurs in stage 2 and contributes to work hardening.

Considering the unique distribution of alloying elements in austenite of steel MSP-Q, the

martensitic transformation start temperature was calculated based on the following equation [191] and is presented in Fig. 7.10,

$$M_s = 539 - 423C - 30.4Mn - 7.5Si + 30Al \quad (7.4)$$

The Ms temperature was highest at the phase boundary, which is opposite to conventional Q&P steels and intercritical annealed steels, because the alloying elements are segregated at the phase boundary or distributed uniformly in austenite. We know that the phase boundary is a potential site for nucleation of martensite, because of high local free energy and low interfacial energy. The martensite transformation initiated at the phase boundary of ferrite and austenite progressed in the interior of austenite or parallel to the austenite lath. Thus, 30% retained austenite was left at room temperature because of chemical stability and mechanical stability induced by fresh martensite. The volume fraction of retained austenite was reduced to 24.7% after tempering at 300^{o}C for 30 min, while carbon was enriched in 24.7% retained austenite and enhanced its stability. The concentration of Mn and Al can be ignored because of low diffusion at 300^{o}C. Thus, the retained austenite inherited the distribution of Mn and Al in austenite, which dominated the heterogeneous distribution of stability of retained austenite. Heterogeneous stress concentration and heterogeneous stability of retained austenite led to martensitic transformation during the early stage of deformation, and greatly contributed to work hardening index in stage I.

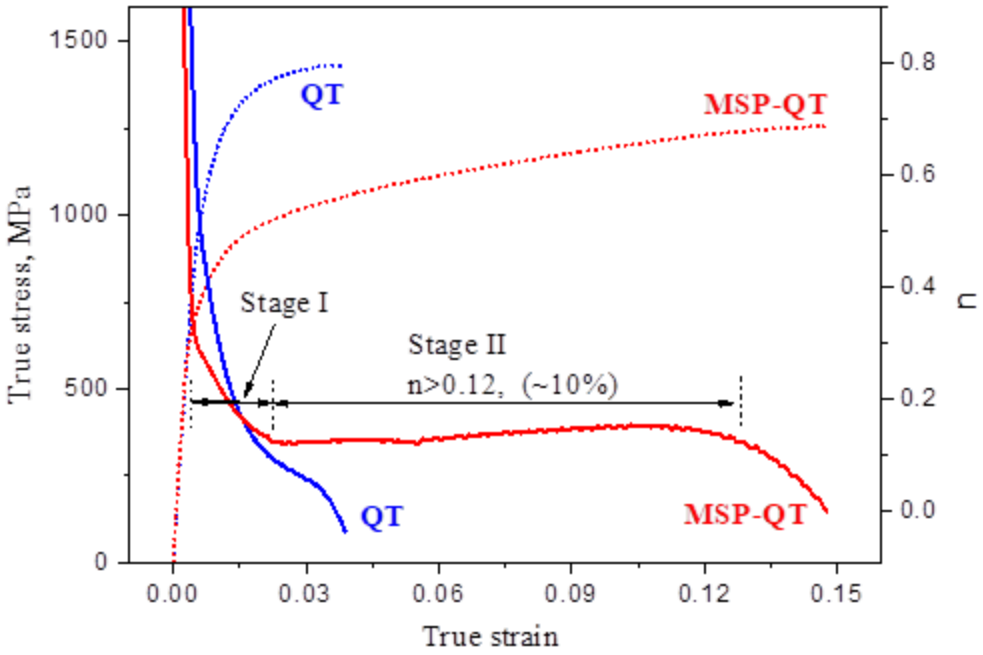

Figure 7. 9 True stress-strain curves and work hardening index of experimental steels.

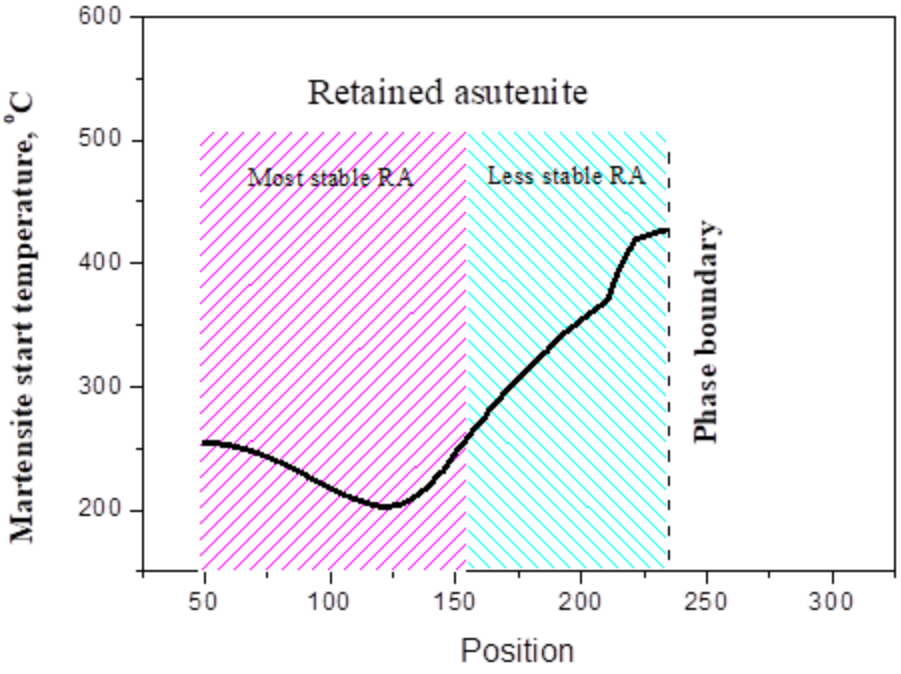

Figure 7. 10 Martensite start temperature in retained austenite.

7.5 CONCLUSIONS

Multi-step partitioning (MSP) process had unique effect in tuning the distribution of alloying elements such that there was periodic distribution of high Mn-low Al and low Mn-high Al region in MSP quenched steel (MSP-Q).

The high Mn and low Al in retained austenite of MSP quenched steel contributed to the stabilization of retained austenite by carbon enrichment during the early stage of tempering. The high concentration of Al in the martensite region restricted the nucleation of carbides and promoted carbon partitioning to retained austenite.

The growth of carbides in martensite during tempering, is governed by the competition of carbon between carbides and retained austenite, which led to faster coarsening rate of carbides compared to conventional quenched and tempered process.

The periodic distribution of Mn and Al, which led to low stability of retained austenite at the phase boundary resulted in a unique TRIP effect in MSP quenched and tempered steel with high work hardening rate during the early stage of deformation.

7.6 SUMMARY

In this chapter, we describe here the periodic distribution of alloying elements in MSP. To accomplish the objective, 0.2C-5Mn-1.6Al steel was subjected to two types of heat treatment, general quench-temper and MSP quench-temper heat treatment with the aim to delineate the influence of MSP quenching on the precipitation behavior of carbides during tempering.

Chapter 8 Conclusion and future work

8.1 CONCLUSIONS

An excellent combination of strength and toughness was obtained in the optimized 820 ºC solution heat treated steel. The ultimate strength and static toughness were 1858 MPa and ~110 $MJ \cdot m^{-3}$ at the temperature where the density of nanoscale precipitates (~2-3 nm) is highest($2.3 \times 1024\ m^{-3}$) with minimal lattice misfit of less than 1%.The precipitation strengthening was the dominant strengthening mechanism in T-250 maraging steels. the highest density of nanoscale precipitates and lowest lattice misfit led to work hardening at a later stage (high strain) and a longer work hardening period, which contributed to increase in the elastic deformation and uniform deformation regimes.

The best combination of high-strength and high-toughness was obtained at aging temperature of 520 ℃, without sacrificing ductility. The ultimate strength and static toughness at this peak aged condition were 1850 MPa and 125.4 $MJ \cdot m^{-3}$, respectively. The microstructural constituents in maraging steels were strongly influenced by the aging temperature.

With increase of aging temperature, the preferred orientation of matrix was weakened. the size of nanoscale precipitates was increased from ~3 nm to ~10 nm. The characteristics of precipitation (size, density and interparticle spacing) at different aging temperatures governed the strengthening contribution and mechanism.

Multiple deformation processes occurred during tensile deformation. The high ductility of ultrahigh strength cobalt-free maraging steel is attributed to cumulative contribution of glide of dislocations on habit planes that transformed the morphology of lath-type martensite, progressive formation of jogs and kinks across the martensite lath, stacking fault and twinning. The above contributions to ductility are in addition to the significantly reduced elastic interaction between the

low lattice misfit nanoscale precipitates and dislocations that reduces the ability for crack initiation at the particle-matrix interface.

Three types of reverted austenite were obtained in maraging steel depending on aging temperature and holding time: granular reverted austenite at grain boundaries (γ_{G1}), lamellar reverted austenite in the Fe-Ni matrix (γ_L) and globular reverted austenite (γ_{G2}) inside the entire martensite grain. The nucleation rate of reverted austenite was envisaged to be lower than the growth rate at low temperature. The reverted austenite formed into different morphologies as γ_{G1} and γ_L and grew rapidly with different orientations. While based on the morphological observation, the nucleation rate of reverted austenite was significantly higher than the growth rate at high temperature, such that γ_{G1} and γ_L converted to γ_{G2}.

Multi-step partitioning (MSP) process had unique effect in tuning the distribution of alloying elements such that there was periodic distribution of high Mn-low Al and low Mn-high Al region in MSP quenched steel (MSP-Q). The periodic distribution of Mn and Al, which led to low stability of retained austenite at the phase boundary resulted in a unique TRIP effect in MSP quenched and tempered steel with high work hardening rate during the early stage of deformation.

8.2 FUTURE WORK

In maraging steel research, the kinetic origin of nanoscale twins was observed, and hypothesis was proposed meanwhile due to lack of direct evidence we cannot solidified it. In-situ TEM or other technique which can provide direct evidence is required for further research. Since experimental data has been sufficiently acquired, we will continue in thermodynamic simulation of deformation behavior and interaction between precipitates and dislocation to further facilitate

the understanding in strengthening mechanism. Reverted austenite in high aging temperature is observed and its essential for further improvement of ductility of maraging steel.

In medium manganese steel research, MSP method is well developed, and we have gained in depth understanding in partition of alloy elements. Future research will focus on more complex alloy design and higher carbon content to achieve better mechanical properties.

References

[1] Ramana, P. Venkata, et al. Materials & Design 31.2 (2010): 749-760.

[2] Garrison Jr, W. M., and M. K. Banerjee. "Martensitic non-stainless steels: high strength and high alloy." (2016).

[3] Mihalisin, J. R., and C. G. Bieber. JOM 18.9 (1966): 1033-1036.

[4] Decker, R. F., and S. Floreen. "Maraging steels--the first 30 years." Maraging steels: recent developments and applications (1988): 1-38.

[5] Floreen, Ss. Metallurgical Reviews 13.1 (1968): 115-128.

[6] Adrian P. Mouritz S Strengthening of metal alloys, ,2012, Pages 57-90

[7] Military specification: Steel: 18 percent nickel alloy maraging

[8] Michlinmetal, Maraging steel 200 specification

[9] Sadowski, E. P., Metals Eng. Quart, 5,56-64(1965).

[10] Decker, R. F., S. Floreen, and R. K. Wilson. "Maraging steels: recent developments and applications." RK Wilson, Warrendale, PA (1988).

[11] Asayama, Y. "Maraging Steels: Recent Developments and Applications." TMS/AIME, Warrendale, PA (1988): 295.

[12] Tariq, Fawad, et al. Journal of Materials Engineering and Performance 19.2 (2010): 264-273.

[13] Marcisz, Jaroslaw, et al. "New generation maraging steel and high-carbon bainitic steel for armours." Proceedings of 26th International Symposium on Ballistics, Miami, USA. Vol. 12. No. 16.09. 2011.

[14] Cajner, Franjo, and Dragomir Krumes. "Maraging steels-New tools material." BIAM. 1998.

[15] Ute, Jufr. "ARMED SERVICES TECHNICAL INFORMATION AGENCY ARLINGTON

HALL STATION ARLINGTON 12, VIRGINIA."

[16] Mouritz, Adrian P. Introduction to aerospace materials. Elsevier, 2012.

[17] R. F. Decker, J. E. T. Wash, and A. J. Goldman, Trans. Quart. ASM, 1962 55-58

[18] B. G. Reisdorf and A. J. Baker, Wright Patterson AFB, Ohio, Tech. Rep. (AFML-TR-64-390), 1965

[19] D. T. Peters and C. R. Cupp, Trans. Met. Soc. A.I. M. E., 1966, 236, 1420.

[20] Ahmed, M., I. Nasim, and S. W. Husain. Journal of materials engineering and performance 3.2 (1994): 248-254.

[21] V. M. Kardonskii and M. D. Perkas, Fiz. Metall. i Metalloved., 1_99, No. 2 (1965).

[22] G. Miller and W. Mitchell, J. Iron Steel Inst., 203 (1965).

[23] R. Decker, J. Eash, and A. Goldman, Trans. Am. Soe. Met., 55, No. 1 (1962).

[24] 5. Floreen and G. Speich, Trans. Am. Soe. Met., 5_77 (1964).

[25] He, Yi, et al Materials letters 56.5 (2002): 763-769.

[26] Men'shikova, G. V., I. L. Shimelevich, and G. D. Getmanskaya. Metal Science and Heat Treatment 11.4 (1969): 251-253.

[27] J.-B. Seol, D. Raabe, P.-P. Choi, Y.-R. Im, and C.-G. Park, Acta Mater., vol. 60, no. 17, pp. 6183–6199, Oct. 2012.

[28] S. Zhang and K. O. Findley, “Acta Mater., vol. 61, no. 6, pp. 1895–1903, Apr. 2013.

[29] S. Zaefferer, J. Ohlert, and W. Bleck, Acta Mater., vol. 52, no. 9, pp. 2765–2778, May 2004.

[30] W. Bleck, “Proceedings of the International Conference on TRIP-Aided High Strength Ferrous Alloys,” 2002, p. 13.

[31] A. Markfeld and A. Rosen, Mater. Sci. Eng., vol. 46, no. 2, pp. 151–157, Dec. 1980.

[32] L. T. Shiang and C. M. Wayman, Metallography, vol. 21, no. 4, pp. 425–451, 1988.

[33] R. Schnitzer, R. Radis, M. Nöhrer, M. Schober, R. Hochfellner, S. Zinner, E. Povoden-Karadeniz, E. Kozeschnik, and H. Leitner, Mater. Chem. Phys., vol. 122, no. 1, pp. 138–145, 2010.

[34] W. Sha, A. Cerezo, and G. Smith, Metall. Mater. Trans. A, vol. 24, no. 6, pp. 1221–1232, 1993

[35] Y. He, K. Yang, and W. Sha, Metall. Mater. Trans. A, vol. 36, no. 9, pp. 2273–2287, 2005.

[36] S.-J. Kim and C. M. Wayman, Mater. Sci. Eng. A, vol. 128, no. 2, pp. 217–230, 1990.

[37] A. Shekhter, H. Aaronson, M. Miller, S. Ringer, and E. Pereloma, Metall. Mater. Trans. A, vol. 35, no. 3, pp. 973–983, 2004

[38] H. Leitner, R. Schnitzer, M. Schober, and S. Zinner, Acta Mater., vol. 59, no. 12, pp. 5012–5022, 2011

[39] V. K. Vasudevan, S. J. Kim, and C. M. Wayman, Metall. Trans. A,vol. 21, no. 10, pp. 2655–2668, Oct. 1990.

[40] E. V Pereloma, A. Shekhter, M. K. Miller, and S. P. Ringer, Acta Mater., vol. 52, no. 19, pp. 5589–5602, 2004.

[41] W. Sha, A. Cerezo, and G. D. W. Smith, Metall. Trans. A, vol. 24, no. 6, pp. 1251–1256, 1993.

[42] C. Servant, G. Maeder, and G. Cizeron, Metall. Trans. A, vol. 6, no. 5, pp. 981–990, May 1975. References 186

[43] C. Servant, N. Bouzid, and O. Lyon, Philos. Mag. A, vol. 56, no. 5, pp. 565–582, Nov. 1987.

[44] A. Gemperle, J. Gemperlova, W. Sha, and G. D. W. Smith, vol. 8, no. 6, pp. 546–554, 1992.

[45] X. Li and Z. Yin, Mater. Lett., vol. 24, no. 4, pp. 239–242, 1995.

[46] H. Luo, J. Shi, C. Wang, W. Cao, X. Sun, and H. Dong, Acta Mater., vol. 59, no. 10, pp.

4002–4014, Jun. 2011.

[47] Jiang, Suihe, et al. Nature 544.7651 (2017): 460.

[48] Han, G., et al. Materials Science and Engineering: A 730 (2018): 119-136.

[49] W. Sha and Z. Guo, Maraging Steels: Modelling of Microstructure, Properties, and Applications. Woodhead, Oxford, 2009.

[50] J. K. Tien, P. G. Shewmon, and J. S. Foster, Scr. Metall., vol. 7, no. 11, pp. 1171–1174, Nov. 1973.

[51] R. Wagner, R. Kampmann, and P. W. Voorhees, "Homogeneous Second-Phase Precipitation, in Phase Transformations in Materials," G. Kostorz, Ed. Weinheim, FRG: Wiley-VCH Verlag GmbH & Co. KGaA, 2001.

[52] R. Kampmann and R. Wagner, Decomposition of Alloys: The Early Stages. Elsevier, 1984.

[53] I. M. Lifshitz and V. V. Slyozov J. Phys. Chem. Solids, vol. 19, no. 1–2, pp. 35–50, Apr. 1961.

[54] C. Wagner, Zeitschrift für Elektrochemie, Berichte der Bunsengesellschaft für Phys. Chemie, vol. 65, no. 7-8, pp. 581–591, Sep. 1961.

[55] L. Ratke and P. W. Voorhees, Growth and Coarsening: Ripening in Materials Processing, Springer V. Berlin, 2002.

[56] A. Brailsford and P. Wynblatt, Acta Metall., vol. 27, no. 3, pp. 489–497, Mar. 1979.

[57] J. A. Marqusee and J. Ross, J. Chem. Phys., vol. 80, no. 1, p. 536, Jan. 1984.

[58] K. Tsumuraya and Y. Miyata, Acta Metall., vol. 31, no. 3, pp. 437–452, Mar. 1983.

[59] S. P. Marsh and M. E. Glicksman, Acta Mater., vol. 44, no. 9, pp. 3761–3771, Sep. 1996.

[60] Z. K. Teng, C. T. Liu, G. Ghosh, P. K. Liaw, and M. E. Fine, Intermetallics, vol. 18, no. 8, pp. 1437–1443, Aug. 2010

[61] Ohkita, Shigeru, and Yukihiko Horii ISIJ international 35.10 (1995): 1170-1182.

[62] ZACKAY V F, PARKER E R, FAHR D, et al. The enhancement of ductility in high-strength steels[J]. ASM Trans Quart, 1967, 60(2): 252-259.

[63] MATSUMURA O, SAKUMA Y, TAKECHI H. Transactions of the Iron and Steel Institute of Japan, 1987, 27(7): 570-579.

[64] SUGIMOTO K-I, KOBAYASHI M, HASHIMOTO S-I. Metallurgical Transactions A, 1992, 23(11): 3085-3091.

[65] ZAEFFERER S, OHLERT J, BLECK W. Acta Materialia, 2004,52(9): 2765-2778.

[66] MAHIEU J, DE COOMAN B, CLAESSENS S. metallurgical and materials transactions A, 2001, 32(11): 2905-2908.

[67] MINTZ B. The influence of aluminium on the strength and impact properties of steel.Ghent: International Conference on TRIP-Aided High Strength Ferrous Alloys, 2002.

[68] ILANA B, TIMOKHINA P D. Effect of alloying elements on the microstructure-property relationship in thermos mechanically processed CMn-Si TRIP steels. De Cooman B C. Int. Conf. on TRIP-Aided High Strength Ferrous Alloys, 2001.

[69] BLECK W. TRIP aided high strength ferrous alloys, 2002: 13-22.

[70] LI Z, WU D, HU R. Journal of Iron and Steel Research, International, 2006, 13(5): 41-46.

[71] CABALLERO F, BHADESHIA H. Current Opinion in Solid State and Materials Science, 2004, 8(3): 251-257.

[72] CABALLERO F, BHADESHIA H, MAWELLA K, et al. Materials science and technology, 2002, 18(3): 279-284.

[73] CABALLERO F, SANTOFIMIA M, GARCíA-MATEO C, et al. Materials & Design, 2009, 30(6): 2077-2083.

[74] SPEER J, MATLOCK D, DE COOMAN B, et al. Acta Materialia, 2003, 51(9): 2611-2622.

[75] MATLOCK D K, BRäUTIGAM V E, SPEER J G. Application of the quenching and partitioning (Q&P) process to a medium-carbon, high-Si microalloyed bar steel[C]. Materials Science Forum, 2003.

[76] EDMONDS D, HE K, RIZZO F, et al. Materials Science and Engineering: A, 2006, 438: 25-34.

[77] GALI A, GEORGE E P. Intermetallic, 2013, 39: 74-78.

[78] GIRAULT E, JACQUES P, HARLET P, et al. Materials Characterization, 1998, 40(2): 111-118.

[79] RAY A, DHUA S K. Materials Characterization, 1996, 37(1): 1-8.

[80] Hsu, T. Y., and Zu Yao Xu. Materials Science Forum. Vol. 561. Trans Tech Publications, 2007.

[81] HSU T, JIN X, RONG Y. Journal of Alloys and Compounds, 2013, 577: S568-S571.

[82] Ohtsuka, S., et al. Journal of nuclear materials 367 (2007): 160-165.

[83] QIN S, LIU Y, HAO Q, et al. Metallurgical and Materials Transactions A, 2015, 46(9): 4047-4055.

[84] MILLER R. Metallurgical Transactions, 1972, 3(4): 905-912.

[85] NIIKURA M, MORRIS J. Metallurgical Transactions A, 1980,11(9): 1531-1540.

[86] D. Raabe, D. Ponge, O. Dmitrieva, B. Sander, Nanoprecipitate-hardened 1.5 GPa steels with unexpected high ductility. Scr. Mater 60 (2009) 1141-1144.

[87] R.F. Decker, S. Floreen, Maraging Steels: Recent Developments and Applications (ed. R. K. Wilson), TMS-AIME (1988) 1-38.

[88] Z.M. Li, K.G. Pradeep, Y. Deng, D. Raabe, C.C. Tasan, Metastable high-entropy dual-phase

alloys overcome the strength–ductility trade-off, Nature 534 (2016) 227-230.

[89] R.D.K. Misra, V.S.A. Challa, P.K.C. Venkatsurya, Acta Mater 84 (2015) 339-348.

[90] J. Han, S.J. Lee, J.G. Jung, Y.K. Lee, Acta Mater 78 (2014) 369-377.

[91] S. Curtze, V.T. Kuokkala, Acta Mater 58 (2010) 5129-5141.

[92] D. Ye, Li J, Q.L. Yong, Mater. Technol. 27 (2012) 88-91.

[93] S. Liu, Z. Xiong, H. Guo, C. Shang, R.D.K. Misra, Acta Materialia 124 (2017) 159-172.

[94] ASTM E-8M. Standard Test Methods for Tension Testing of Metallic Materials. Annual book of ASTM standards, ASTM International, 2003.

[95] C. Yang, S. Luo, and W. Yu, GB: Retained austenite in steel-Quantitative determination method of X-ray diffractometer. Standardization Administration of the People's Republic of China, 2006.

[96] W. Conshohocken, ASTM Standard, Standard Practice for X-Ray Determination of Retained Austenite in Steel with Near Random Crystallographic Orientation'' Standard E975-03, vol. 03, no. Reapproved 2008. American Society for Testing and Materials, 2003.

[97] D. B. Williams and C. B. Carter, Transmission Electron Microscopy. New York: Springer Science, 2009.

[98] J.H. Kim, D.H. Kim, S.I. Moon, Mater. Sci. Eng. A 387-389 (2004) 381-384.

[99] L.Y. Zhang, G. Yang, C.X. Huang, Acta Metall. Sin. 44 (2008) 409.

[100] L. Lu, Z.B. Li, Z.Y. Bi, J. Iron Steel Res. 26 (2014) 67-70.

[101] L.W. Tsay, H.L. Lu, C. Chen, Corros. Sci. 50 (2008) 2506-2511.

[102] K. Li, J. Shan, C. Wang, Z. Tian, Mater. Sci. Eng. A 663 (2016) 157-165.

[103] P.P. Sinha, K.T. Tharian, D. Sreekumar, Mater. Sci. Technol. 14 (1998) 1-9.

[104] K. Li, J. Shan, C. Wang, Z, Sci. Eng. A 669 (2016) 58-65.

[105] V.K. Vasudevan, S.J. Kim, C.M. Wayman, Metall. Trans. 21A (1990) 2655-2668.

[106] W. Sha, Iron & Steel, 29 (1994) 47-51.

[107] K. Stiller, F. Danoix, A. Bostel, Appl. Surf. Sci. 94-95 (1996) 326-333.

[108] W. Sha, A. Cerezo, G.D.W. Smith, Metall. Trans. A 24A (1993) 1221-1232.

[109] F. Habiby, T.N. Siddiqui, H. Hussain, J. Mater. Sci. 31 (1996) 305-309.

[110] R. Schnitzer, M. Schober, S. Zinner, H. Leitner, Acta Mater 58 (2010) 3733-3741.

[111] T. Gladman, Mater. Sci. Technol. 15 (1999) 30-36.

[112] R.M. Brito, H.J. Kestenbach, J. Mater. Sci. 16 (1981) 1257-1263.

[113] M.F. Ashby, Acta Metall. 14 (1966) 679-683.

[114] P. Kelly, Int. Metall. Rev. 18 (1973) 31-36.

[115] I. Baker, Mater. Sci. Eng. A 192-193, (1995) 1-13.

[116] H.Q. Ye, B.S. Zou, Acta Metall. Sin. 15 (1979) 69-76.

[117] H.M. Tawancy, J. Mater. Sci. 15 (1980) 2597-2604.

[118] R.D. Noebe, R.R. Bowman, M.V. Nathal, Int. Mater. Rev. 38 (1993) 193-232.

[119] Z.B. Jiao, J.H. Luana, M.K. Millerb, Acta Mater 84 (2015) 283-291.

[120] K. Li, J. Shan, C. Wang, Z. Tian, Mater. Sci. Eng. A 669 (2016) 58–65.

[121] K. Li, J. Shan, C. Wang, et al. Mater. Sci. Eng. A 681 (2017) 41-49.

[122] K. Li, B. Yu, R.D.K. Misra, et al, Mater. Sci. Eng. A 715 (2018) 174-185.

[123] L. Lu, Z.B. Li, Z.Y. Bi, J. Iron Steel Res. 26 (2014) 67–70.

[124] L.W. Tsay, H.L. Lu, C. Chen, Corros. Sci. 50 (2008) 2506–2511.

[125] P.R. Narayanan, K. Sreekumar, A. Natarajan, P.P. Sinha, J. Mater. Sci. 25 (1990) 4587-4591.

[126] J. Hu, L.X. Du, J.J. Wang, C.R. Gao, Mater. Sci. Eng. A 577 (2013) 161-168.

[127] X.L. Wan, K.M. Wu, G. Huang, K.C. Nune, Y. Li, L. Cheng, Sci. Technol. Weld. Join. 21

(2016) 295-302.

[128] K. Luecke, Proceedings of the ICOTOM7: Proceedings Texture of Materials; C.M. Brakman, P. Jongenburger, E.J. Mittemiejer, Eds.; Netherlands Society of Materials Science: Noordwijkerhout, The Netherlands, 1984.

[129] A.N. Kolmogorov, Izv. Akad. Nauk SSSR Ser. Matem. 1 (1937) 355-359.

[130] S.G. Chowdhury, S. Datta, B.R. Kumara, et al. Mater. Sci. Eng. A 443 (2007) 114-119.

[131] D. Raabe, Acta Mater. 45 (1997) 1137-1151.

[132] H.P. Lin, T.S. Ng, J.C. Kuo, et al. Mater. Charact. 93 (2014) 167-172.

[133] T. Gladman, Mater. Sci. Technol. 15 (1999) 30-36.

[134] R. Tewari, S. Mazumder, I. S. Batra, Acta Mater. 48 (2000) 1187-1200.

[135] R.M. Brito, H.J. Kestenbach, J. Mater. Sci. 16 (1981) 1257–1263.

[136] M.F. Ashby, Acta Metall. 14 (1966) 679–683.

[137] T. Gressmann, M. Wohlschlögel, S. Shang, Acta Mater. 55 (2007) 5833–5843.

[138] S. Braccini, C. Casciano, F. Cordero, Meas. Sci. Technol. 11 (2000) 467–476.

[139] P.P. Sinha, K.T. Tharian, D. Sreekumar, Steel Res. 65 (1994) 494-499.

[140] T. Gladman, Mater. Sci. Technol. 15 (1999) 30-36.

[141] R. Tewari, S. Mazumder, I. S. Batra, Acta Mater. 48 (2000) 1187-1200.

[142] J.S. Koehler, F. Seitz, E. Orowan, et al. Dislocations in metals, AIME, New York, (1954) 31-32.

[143] V.K. Vasudevan, S.J. Kim, C.M. Wayman, Metall. Trans. 21A (1990) 2655-2668.

[144] P.P. Sinha, K.T. Tharian, D. Sreekumar, Mater. Sci. Technol. 14 (1998) 1-9.

[145] F. Habiby, T.N. Siddiqui, H. Hussain, J. Mater. Sci. 31 (1996) 305-309.

[146] R. Schnitzer, M. Schober, S. Zinner, H. Leitner, Acta Mater. 58 (2010) 3733-3741.

[147] U.K. Viswanathan, G.K. Dey, M.K. AsundiTrans. A 24 (1993) 2429-2442.

[148] S. Jiang, H. Wang, Y. Wu, et alNature 544 (2017) 460-464.

[149] P. Rama Rao, Private Communication, 2018.

[150] J.P. Hirth, Theory of dislocations, John wiley & sons Inc., New York, 1982.

[151] W. Puschl, Prog. Mater. Sci. 47 (2002) 415-461.

[152] S. Mahajan, C.S. Pande, M.A. Imam, et al. Acta Mater. 45 (1997) 2633-2638.

[153] T.S. Byun N. Hashimoto, K. Farrell, Acta Mater. 52 (2004) 3889-3899.

[154] K. Li, V.S.Y. Injeti, R.D.K. Misra, Z.H. Cai, H. Ding, Mater. Sci. Eng. A 711 (2018) 515-523.

[155] S. Takaki, K. Fukunaga, J. Syarif, T. Tsuchiyama, Mater. Trans. 45 (2004) 2245-2251.

[156] N. Kenyon, Weld. J. 47 (1968) 193S.

[157] K. Li, J.G. Shan, C.X. Wang, Z.L. Tian, Acta Metall. Sin. 51 (2015) 904–912.

[158] H.J. Rack, R.D. Kalish, Metall. Mater. Trans. B 2 (1971) 3011-3020.

[159] Y.J. Lee, I.K. Lee, S.C. Wu, Sci. Technol. Weld. Join. 12 (2007) 266–273.

[160] D.T. Peters, ASM Trans. Q. 61 (1968) 62.

[161] C.P. Wu, L.W. Tsay, C. Chen, Mater. Sci. Eng.: A 346 (2003) 302–309.

[162] K. Tomimura, S. Takaki, Y. Tokuna, J. Iron Steel Inst. Jpn. 31 (1991) 1431–1437.

[163] K. Li, B. Yu, R.D.K. Misra, C.X. Wang, Z.L. Tian, J.G. Shan, Mater. Sci. Eng.: A 718 (2018) 173–181.

[164] S. Lee, Y. Park, Y. Lee, Mater. Sci. Eng.: A 515 (2009) 42–37.

[165] K. Li, J.G. Shan, C.X. Wang, Z.L. Tian, Mater. Sci. Eng.: A 681 (2017) 41–49.

[166] S. Matsuda, Y. Okamura, Tetsu-to-Hagane 60 (1974) 226–238.

[167] H. Luo, J. Shi, C. Wang, W. Cao, X. Sun, H. Dong, Acta Mater 59 (2011) 4002–4014.

[168] M.R. Plichata, H.I. Aaronson, Metall. Trans. 5 (1974) 2611–2613.

[169] N. Nakada, T. Tsuchiyama, S. Takaki, S. Hashizume, ISIJ Int. 47 (2007) 1527–1532.

[170] K. Li, J.G. Shan, C.X. Wang, Z.L. Tian, Mater. Sci. Eng.: A 669 (2016) 58–65.

[171] K. Li, L. Wei, B. An, B. Yu, R.D.K. Misra, Mater. Sci. Eng.: A 739 (2019) 445–454.

[172] H. Luo, J. Shi, C. Wang, W. Cao, X. Sun, H. Dong, Acta Materialia 59(10) (2011) 4002-4014.

[173] W. Zhou, H. Guo, Z. Xie, X. Wang, C. Shang, Materials Science and Engineering: A 587 (2013) 365-371.

[174] B. He, B. Hu, H. Yen, G. Cheng, Z. Wang, H. Luo, M. Huang, Science 357(6355) (2017) 1029-1032.

[175] D. Edmonds, K. He, F. Rizzo, B. De Cooman, D. Matlock, J. Speer, Materials Science and Engineering: A 438 (2006) 25-34.

[176] Y. Sakuma, O. Matsumura, H. Takechi, Metallurgical Transactions A 22(2) (1991) 489-498.

[177] C. Sun, S.L. Liu, R.D.K. Misra, Q. Li, D.H. Li, Materials Science and Engineering: A 711 (2018) 484-491.

[178] E. De Moor, D.K. Matlock, J.G. Speer, M.J. Merwin, Scripta Materialia 64(2) (2011) 185-188.

[179] D. De Knijf, R. Petrov, C. Föjer, L.A. Kestens Materials Science and Engineering: A 615 (2014) 107-115.

[180] Y. Toji, G. Miyamoto, D. Raabe, Acta Materialia 86(0) (2015) 137-147.

[181] T. Hsu, X. Jin, Y. Rong, Journal of Alloys and Compounds 577 (2013) S568-S571.

[182] D.K. Matlock, V.E. Bräutigam, J.G. Speer, Trans Tech Publ, 2003, pp. 1089-1094.

[183] W. Leslie, G. Rauch, Metallurgical Transactions A 9(3) (1978) 343-349.

[184] G.M. Michal, J.A. Slane, Metallurgical Transactions A 17(8) (1986) 1287-1294.

[185] S. Basu, S.K. Choudhary, N.U. Girase, ISIJ international 44(10) (2004) 1653-1660.

[186] V. Miihkinen, D. Edmonds, Materials Science and Technology 3(6) (1987) 441-449.

[187] A. Clarke, J. Speer, M. Miller, R. Hackenberg, D. Edmonds, D. Matlock, F. Rizzo, K. Clarke, E. De Moor, Acta materialia 56(1) (2008) 16-22.

[188] S. Liu, Z. Xiong, H. Guo, C. Shang, R.D.K. Misra, Acta Materialia 124 (2017) 159-172.

[189] V. Colla, M. De Sanctis, A. Dimatteo, G. Lovicu, A. Solina, R. Valentini, Metallurgical and Materials Transactions A 40(11) (2009) 2557-2567.

[190] L. Luo, W. Li, L. Wang, S. Zhou, X. Jin, Materials Science and Engineering: A 682 (2017) 698-703.

[191] J. Mahieu, B. De Cooman, J. Maki, Metallurgical and Materials Transactions A 33(8) (2002) 2573-2580.

Vita

Bing Yu earned his bachelor's degree in Material Physics from University of Science and Technology Beijing (USTB), China in 2015. In 2016 he earned his master's degree in Material Science and Engineering from University of Florida. Later he joined the University of El Paso to pursue his doctoral degree in Materials Engineering.

Dr. Yu was the recipient of the Graduate Research Award presented by the Department of MMBME Department, The University of Texas at El Paso and Anita Mochen Loya Fellowship for outstanding research student award in 2017 and 2018.

Dr. Yu has authored as main author 6 publications in international journals and presented them in several international conferences including TMS, MS&T during 2017 to 2019. The publications related to his dissertation topic are as follows:

1. **B. Yu**, et al. Materials Science and Engineering: A 766 (2019): 138357.
2. Li, K., **B. Yu**, R. D. K. Misra, G. Han, S. Liu, and C. J. Shang. Materials Science and Engineering: A 715 (2018): 174-185.
3. Li, K., **B. Yu**, R. D. K. Misra, G. Han, S. Liu, and C. J. Shang. Materials Science and Engineering: A 715 (2018): 174-185.
4. Li, K., Wei, L., An, B. **B. Yu,** and Misra, R.D.K., 2019. Materials Science and Engineering: A, 739, pp.445-454.
5. Li, K., Wei, L., **B. Yu,** and Misra, R.D.K., 2019. Materials Letters, p.126692

Contact Information: bryan.yu.bing@gmail.com